Characterization of HgCdTe and Related Materials

For Third Generation Infrared Detectors

by

Majid Vaghayenegar

A Dissertation Presented in Partial Fulfillment
of the Requirements for the Degree
Doctor of Philosophy

Approved November 2017 by
Graduate Supervisory Committee:

David J. Smith, Chair
Martha R. McCartney
Peter A. Crozier
Mariana I. Bertoni

ARIZONA STATE UNIVERSITY

December 2017

ABSTRACT

$Hg_{1-x}Cd_xTe$ (MCT) has historically been the primary material used for infrared detectors. Recently, alternative substrates for MCT growth such as Si, as well as alternative infrared materials such as $Hg_{1-x}Cd_xSe$, have been explored. This dissertation involves characterization of Hg-based infrared materials for third generation infrared detectors using a wide range of transmission electron microscopy (TEM) techniques.

A microstructural study on HgCdTe/CdTe heterostructures grown by MBE on Si (211) substrates showed a thin ZnTe layer grown between CdTe and Si to mediate the large lattice mismatch of 19.5%. Observations showed large dislocation densities at the CdTe/ZnTe/Si (211) interfaces, which dropped off rapidly away from the interface. Growth of a thin HgTe buffer layer between HgCdTe and CdTe layers seemed to improve the HgCdTe layer quality by blocking some defects.

A second study investigated the correlation of etch pits and dislocations in as-grown and thermal-cycle-annealed (TCA) HgCdTe (211) films. For as-grown samples, pits with triangular and fish-eye shapes were associated with Frank partial and perfect dislocations, respectively. Skew pits were determined to have a more complex nature. TCA reduced the etch-pit density by 72%. Although TCA processing eliminated the fish-eye pits, $\frac{1}{2}[0\bar{1}1]$ dislocations reappeared in shorter segments in the TCA samples. Large pits were observed in both as-grown and TCA samples, but the nature of any defects associated with these pits in the as-grown samples is unclear.

Microstructural studies of HgCdSe revealed large dislocation density at ZnTe/Si(211) interfaces, which dropped off markedly with ZnTe thickness. Atomic-resolution STEM images showed that the large lattice mismatch at the ZnTe/Si interface was accommodated through {111}-type stacking faults. A detailed analysis showed that the stacking faults were inclined at angles of 19.5 and 90 degrees at both ZnTe/Si and HgCdSe/ZnTe interfaces. These stacking faults were associated with Shockley and Frank partial dislocations, respectively. Initial attempts to delineate individual dislocations by chemical etching revealed that while the etchants successfully attacked defective areas, many defects in close proximity to the pits were unaffected.

This dissertation is dedicated to my parents, Zohreh and Mojtaba and my sister Faranak.

ACKNOWLEDGMENTS

I would like to express my deepest appreciation to my mentor Regents' Professor David J. Smith for his tireless guidance, support and encouragement since the start of my training and course work in developing my research and personal skills and eventually accomplishing this dissertation. I would also like to thank my supervisory committee members, Professors Martha R. McCartney, Peter A. Crozier, and Mariana I. Bertoni, for their valuable time and suggestions.

I would like to acknowledge the staff members as well as the use of facilities in John M. Cowley Center for High Resolution Electron Microscopy at Arizona State University. Special thanks to Mr. Karl Weiss, Dr. Toshihiro Aoki, Dr. Katia March, and Mr. Kenneth Mossman for their technical assistance.

I would like to express my sincere appreciation to all my collaborators: Dr. R. N. Jacobs (CERDEC Night Vision and Electronic Sensors Directorate), Dr. Y. P. Chen (Army Research Lab), Dr. S. Simingalam (Army Research Lab), Dr. B. Vanmil (Army Research Lab), Dr. K. Doyle (Army Research Lab) and Dr. P. Wijewarnasuriya (Army Research Lab).

Sincere thanks to my past and present friends and colleagues in 'MDG': Dr. Jaejin Kim, Dr. Jing Lu, Dr. Zhaofeng Gan, Dr. Desai Zhang, Dr. Xiao-Meng Shen, Thomas McConkie, Allison Boley, Sirong Lu, Abhinandan Gangopadhyay, Brian Tracy, Scott Sherman, HsinWei Wu, and Brandon McKeon who generously shared their knowledge and expertise with me and made my studies memorable.

Finally, I owe special thanks to my family away from home in Iran: my parents Mojtaba and Zohreh and my one and only dear sister Faranak who always encouraged and supported me to pursue my dream.

TABLE OF CONTENTS

Page

CHAPTER Page

CHAPTER Page

LIST OF FIGURES

Figure Page

Figure Page

Figure Page

Figure Page

Figure Page

Figure Page

Figure Page

Figure Page

Figure Page

LIST OF TABLES

Table Page

CHAPTER 1

INTRODUCTION

1.1. Infrared Radiation and Detection

Infrared (IR) radiation was first discovered in 1800 by Frederick Herschel.[1] By measuring the temperature of each color in sunlight using a prism and a simple thermometer, he found that the greatest intensity level was beyond the red, which is now called IR.[1] In 1864, Maxwell's theory of electromagnetic radiation classified IR as electromagnetic radiation with wavelengths ranging from visible red light at 700nm all the way to 1mm.[1]

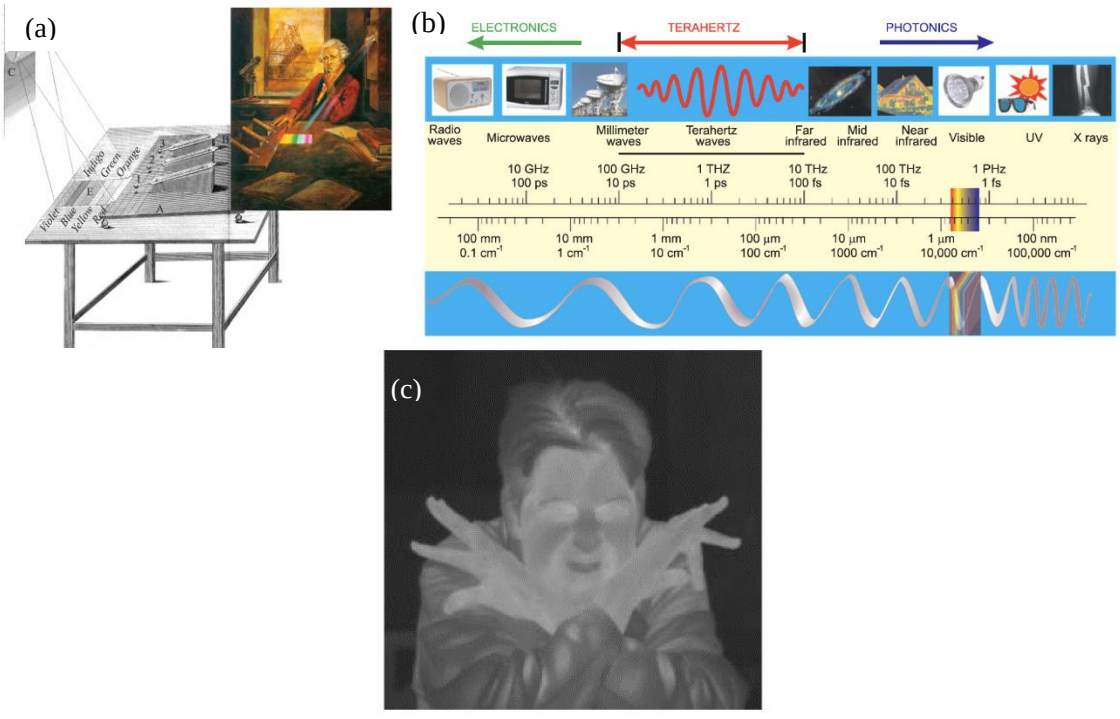

Figure 1. 1 (a) First experimental set-up of Herschel,[1] (b) The electromagnetic spectrum,[2] and (c) High quality infrared image taken with a 30µm unit-cell 256×256 LWIR HgCdTe/Si double-layer-heterojunction.[3]

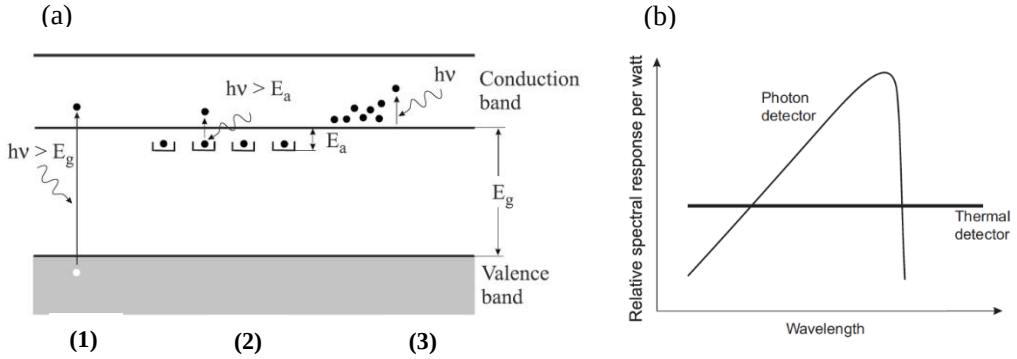

Figure 1. 2 (a) Interaction of radiation with (1) lattice sites, (2) impurity atoms, and (3) free electrons in a semiconductor, (b) Relative spectral response for a photon and thermal detector.[1]

The transformation of IR radiation to a measurable electronic signal is the function of IR detectors. IR detectors in general can be classified in two categories of photon detectors and thermal detectors. In photon detectors, the interaction of radiation with the crystal lattice, impurity atoms or free electrons changes the electronic configuration energy and subsequently produces an output signal. Therefore, photon detectors show a selective wavelength dependence of response for incident radiation. Absorption of radiation in thermal detectors changes the material temperature and subsequently alters physical properties, which can be measured to generate an electrical output. Thus, thermal effects in these detectors are generally wavelength-independent.[1-2] Defect analysis in the traditional constituent building block material of photon detectors, i.e. HgCdTe, is the major topic of this dissertation.

1.2. HgCdTe (MCT)

MCT alloys with variable band gaps were first studied in 1959.[4] Advances in focal-plane array (FPA) technology using MCT have since been made in three major steps or

"generations" which has kept this material as the predominant detector material in all IR spectral bands.[5] As this technology enables people to see in the dark, the military has shown tremendous interest in its development. As a result, most of the progress in the IR field was classified until the late 1960s, and only a few defense-financed companies were conducting research on MCT. This situation changed in 1980 when the Defense Advanced Projects Research Agency (DARPA) allowed US universities to collaborate in MCT research, and the first workshop was held on the physics and chemistry of HgCdTe, now known as the II-VI workshop.[6] Although alternative materials, such as Schottky barriers on Si, SiGe heterojunctions, AlGaAs multiple quantum wells, and GaInSb strained-layer superlattices, have been explored over the years, none of them can so far compete with MCT in terms of fundamental physical properties either for better performance or for operation at higher temperature.[1] However, type-II superlattices are an exception due to their attractive physical properties.[6-7]

1.3. Physical Properties of MCT

$Hg_xCd_{1-x}Te$ is a pseudo-binary alloy with the zincblende structure composed of the semimetal HgTe and the semiconductor CdTe[5]. The MCT properties that make it superior for IR detection are as follows.[5,7-8]

- Tunable cut-off wavelength from 1μm to 30μm;

- Direct band gap and high quantum efficiency due to large optical coefficient;

- Moderate thermal coefficient of expansion;

- Moderate dielectric constant;

- Favorable inherent recombination mechanism that leads to high operating temperature;

- Availability of lattice-matched substrates with wide band gap for epitaxial growth;

Some of these properties will be discussed briefly in the following sections.

1.3.1. Band gap

The band gap of MCT is a function of temperature and alloy composition *x* in $Hg_{1-x}Cd_xTe$. This allows IR coverage over a wide range from short-wavelength infrared (SWIR) 1-3 μm, mid-wave infrared (MWIR) 3-8 μm, long-wave infrared 8-12 μm (LWIR), up to wavelengths greater than 12 μm (VLWIR).[5,8] The band gap (in eV) of MCT as a function of composition *x* and temperature T in Kelvin is given by:[9]

$$E_g = -0.302+1.03x-0.81x^2+0.832x^3+5.35\times10^{-4}(1-2x)T \quad (1.1)$$

Figure. 1.3 shows the bandgap (left axis) and cut-off wavelength (right axis) as a function of composition *x* for MCT at 77K and 300K. The wavelength at which the response drops to its 50% peak value is termed the cut-off wavelength. The material is direct gap at k=0.[10] As can be seen, the band gap changes from -0.3eV for semimetal HgTe all the way to 1.6eV for CdTe. Table 1.1 shows the uncertainty in cut-off wavelength at 77K for *x* variations of 0.1%. Composition control and uniformity is stricter in the LWIR regime with higher uncertainty in the cut-off wavelength.[7]

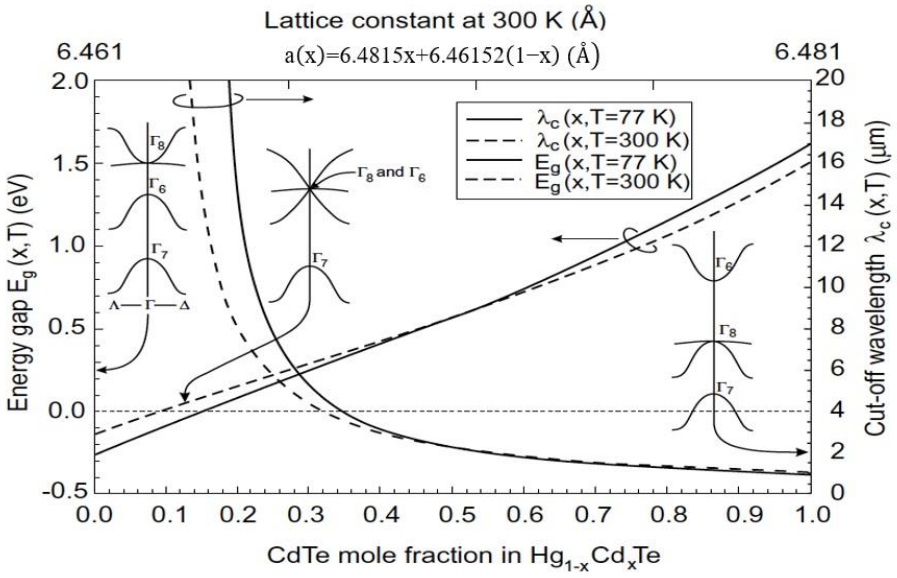

Figure 1. 3 $Hg_{1-x}Cd_xTe$ band gap and cut-off wavelength variation with Cd concentration x.[7]

Composition "x"	**Cut-off wavelength (μm)**	**Uncertainty (μm)**
0.395	3	0.012
0.295	5	0.032
0.210	10	0.131
0.196	14	0.257
0.187	20	0.527

Table 1. 1 Cut-off wavelength uncertainty for 0.1% change in composition at 77K.[7]

1.3.2. Lattice Constant

Schematic structure of an MCT unit cell is shown in Fig. 1.4. It is composed of two interpenetrating face-centered-cubic lattices offset by $(\frac{1}{4}\ \frac{1}{4}\ \frac{1}{4})a$ in the primitive cell. The Te anions are purple colored while cations (Hg or Cd) are yellow.[11] Table 1.2 shows possible *n*-type and *p*-type dopants for MCT. Although *n*-type doping over a wide range

of concentration (10^{14}-10^{19} cm^{-3}) with *in situ* incorporation of Indium or Iodine is possible, controlled *p*-type doping is still challenging to achieve.

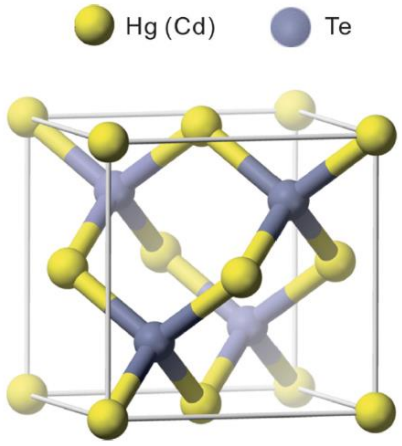

Figure 1. 4 Schematic unit cell of MCT.[11]

Dopant type	*n*-type (group-III on Hg/Cd sites)	*n*-type (group-VII on Te sites)	*p*-type (group-V on Te sites)	*p*-type (group-I on Hg/Cd sites)
Element	B, Al, Ga, In and Ti	F, Cl, Br, I and At	N, P, As, Sb and Bi	Li, Na, Cu, Ag and Au

Table 1. 2 Possible *n-type* and *p-type* dopants for MCT.[11]

The lattice constants of HgTe and CdTe are 6.46Å and 6.48Å, respectively. Lattice constants for compositions in between can be linearly interpolated and the change over the entire range is less than 0.3%. This extremely small value makes MCT attractive for growth of dislocation-free epitaxial films on CdZnTe substrates, and also for growth of complex heterostructures for next-generation IR detectors.[7] Using high-resolution XRD, it was shown that the unstrained lattice constant of $Hg_{1-x}Cd_xTe$ obeyed Vegard's law over the entire composition range:[12]

$$a(x) = 6.4815x+6.46152(1-x)\ (Å) \quad (1.1)$$

A similar relationship for temperature dependence of the lattice parameter has been developed, where a(300K) is the lattice constant at room temperature and B(T) values are given in Table 1.3.[12]

$$a(T) = a(300K)+B(T)\ (Å) \quad (1.2)$$

T (K)	100	200	300	400	500	600	700	800
B(T)	-0.007	-0.004	0.0	0.003	0.006	0.01	0.014	0.019

Table 1. 3 Lattice parameter correction factor B(T) for several temperatures.[12]

1.3.3. Coefficient of Thermal Expansion (CTE)

Since lattice-matching during growth will not be perfectly retained upon cooling, and more importantly during operation of the IR detector, CTE also plays an important role. CTE values for both MCT and CdTe are well documented.[10] Successful integration of MCT on Si read-out integrated-circuit (ROIC) also depends on the CTE differences, which has changed with the historic use of lattice-matched CdZnTe substrate compared with Si substrates which have 19% lattice mismatch.[7]

1.3.4. Minority Carrier Lifetime Properties

Auger and radiative minority lifetime modes are band-to-band recombination mechanisms and are largely unavoidable in MCT. However, the Shockley-Read mode is theoretically avoidable through the elimination of defects in the band gap.[10]

1.4. Evolution of MCT Growth

From early days (1960s to 1970s) until the current day, MCT growth techniques have changed drastically from bulk to epitaxial. Figure. 1.5 shows MCT growth time-line.

Molecular Beam Epitaxy (MBE) has many advantages over traditional growth methods, which make it the predominant method of choice for MCT growth for next-generation IR detectors.[13] These advantages are briefly listed as follows:[14]

- Growth temperature (~185ºC) is lower than MOCVD (300-400 ºC) or LPE (~500ºC), which allows for better control of impurity diffusion and the growth of sharp interfaces.

- Heterostructure growth is easily achieved even with multilayers, whereas LPE is limited to two or three layers.

- *In situ* characterization such as reflection-high-energy electron diffraction (RHEED) during MBE growth.

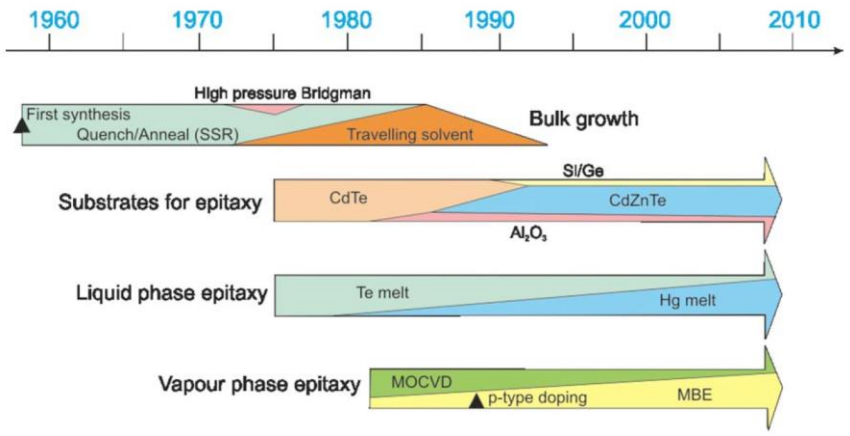

Figure 1. 5 Timeline for MCT growth techniques.[13]

1.4.1. MBE

A brief overview of MBE as an advanced technique for thin-film growth is provided here: a more comprehensive review can be found elsewhere.[15] The materials sources used in MBE are atoms or molecules held in effusion cells. Upon opening the

shutters, constituents in the form of localized beams travel in a nearly collision-free path under ultrahigh-vacuum conditions and reach the heated substrate. Thermal energy of the substrate provides the energy for atoms/molecules hitting the substrate to migrate on the surface before bonding and forming a crystalline film. The arrival rate of the constituents is set through the temperatures of the effusion cells. The composition and thicknesses of the films can be controlled by shutters that can be turned on and off almost simultaneously. Typical growth rates are about 1 monolayer per second. For MCT growth, the background pressure should be kept as low as possible, in the range of 10^{-7}-10^{-8} Torr, to avoid contamination and to preserve electrical properties.[14]

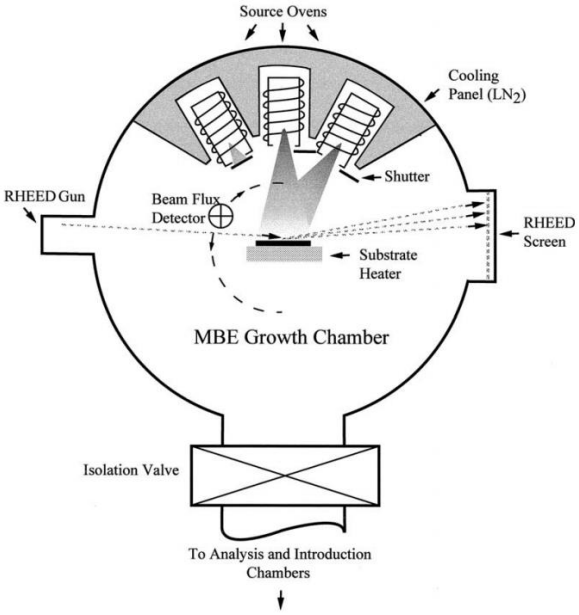

Figure 1. 6 Essential parts of an MBE system.[15]

1.5. Substrate for MCT Growth

$Cd_{0.96}Zn_{0.04}Te$ (CZT) has been the preferred substrate for MCT growth for many years due to its perfect lattice-matching with MCT, and it is still the substrate of choice for current state-of-the-art IR technologies.[11] However, various limitations such as: lack

of major US commercial supplier, larger initial defect density (of the order of 10^5 cm^{-2}) which may initiate defects in MCT during growth, the high price 300-400$/$cm^2$, and the currently smaller available wafer size ~ 36-49cm^2, has motivated researchers to explore the possibility of growth on alternative substrate (e.g. Si, Ge and GaAs).[11,14] These substrates have lower cost, larger available area, lower initial defect density, and are commercially more readily available. Table 1.4 compares the characteristics of CZT, GaAs and Si as possible substrates for MCT growth. Si is more attractive as it is compatible with Si read-out circuits in a flip-chip bonded configuration. However, almost all of these alternative substrates (except for GaSb) suffer from mismatches in lattice constants and coefficients of thermal expansion compared with MCT. This is clearly apparent in Fig 1.7.[11]

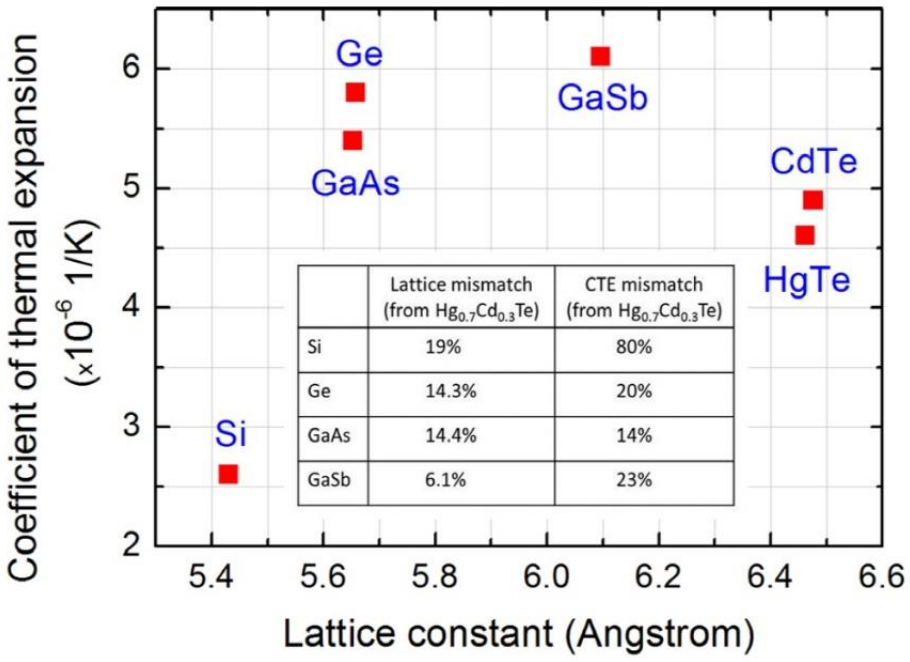

	Lattice mismatch (from $Hg_{0.7}Cd_{0.3}Te$)	CTE mismatch (from $Hg_{0.7}Cd_{0.3}Te$)
Si	19%	80%
Ge	14.3%	20%
GaAs	14.4%	14%
GaSb	6.1%	23%

Figure 1. 7 Lattice constants and coefficients of thermal expansion for alternative substrates at room temperature.[11]

Direct growth of MCT on different substrates will likely lead to the generation of highly defective films which will subsequently deteriorate IR detector performance. The effect of defects on IR detector performance parameters is illustrated in Fig. 1.8.[5] Growth of thick (>10μm) CdTe buffer layers on alternative substrates is a common approach used to entangle dislocations and effectively stop their propagation upwards to the MCT layer. In the case of alternative Si substrates, As passivation followed by growth of a thin ZnTe buffer layer is necessary to stop micro-twin formation and to improve the quality of the following CdTe buffer layer.[16] In addition to the closer lattice-matching to MCT, good IR transmission (47-52%) and narrow XRD FWHM (20-25 arc.sec) make GaSb an intriguing substrate for growth of high quality (less than 5×10^5 cm^{-2}) MCT for LWIR detectors. Thus, research is underway on the growth of MCT on GaSb substrates.[11]

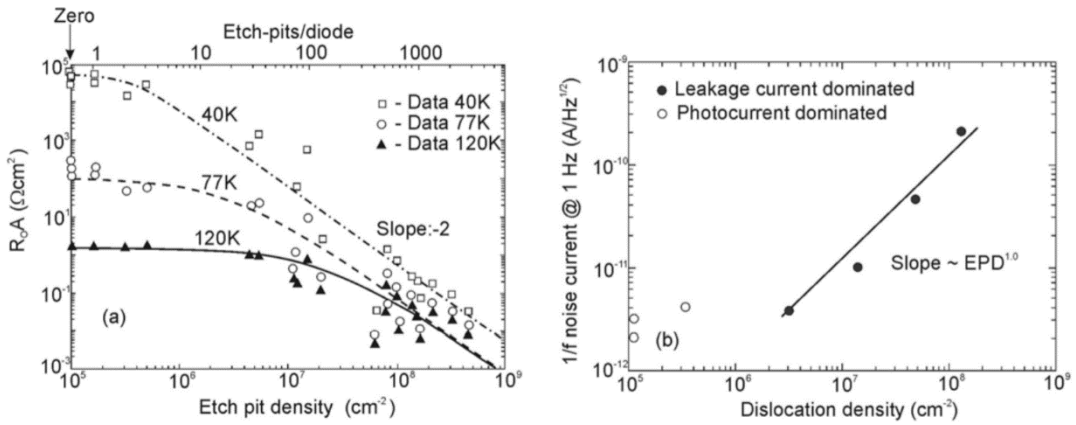

Figure 1. 8 Influence of dislocation density on R_0A and 1/f noise current at 1Hz vs dislocation density for 10.3μm HgCdTe photodiode array.[5]

Properties	CZT	GaAs	Si
Cost per cm^2	US$ 400	US$ 0.71	US$ 0.56
Largest commercial size	49	182.4	5228
Vickers hardness (kg/mm^2) at 300K	60 Brittle	360 Moderately Robust	1150-1330 Strong
Lattice mismatch with HgCdTe (x=0.2 at 300K)	<1%	13.6%	19.47%
Thermal mismatch with HgCdTe (x=0.2 at 300K)	3.53%	27.04%	51.85%
Substrate surface defect density (cm^{-2}) / growth mode	10^4 (high-pressure Bridgman)	5×10^3 (vertical gradient freeze)	10^2 (float-zone growth)
Surface preparation	Difficult, sometimes poor	Standardized	Standardized

Table 1. 4 Properties of CZT, GaAs and Si as substrates for MBE growth of MCT.[14]

1.6. Focal Plane Array (FPA)

An IR detector is basically a multilayer structure composed of contact metal, photon-absorbing material, and substrate. Photoconductors and diodes are the two principal detectors used.[14] Based on detector type and performance, most detectors work in the temperature range from 10-150K. This range is necessary to preserve fast response and good signal-to-noise performance to suppress generation of thermal charge carriers that compete with optical ones. This is merely to minimize noise and increase resolution in detectors by eliminating the near-field IR radiation.[2,14] The maximum operating

temperature of a detector is strongly dependent on cut-off wavelength:[2] $T_{Max} = \frac{300K}{\lambda[\mu m]}$. This imposes a limitation on the performance of the detector at the upper end of the IR spectrum.[14] Therefore, for applications such as space missions, detectors with very long cut-off wavelength require much lower operation temperature. The two current cooling technologies are closed-cycle refrigerators and thermoelectric coolers. The former is used for cooled sensors while the latter is used for uncooled ones.[2] A lattice-like arrangement of individual elements creates the FPA. Each pixel shares one contact with other pixels while having one independent contact.[2] This configuration leads to fundamental limitations of light coupling in neighboring pixels in an array which subsequently develop false counts, or cross-talk.[2] The positions of detector pixels in a sensor system is shown schematically in Fig. 1.9.

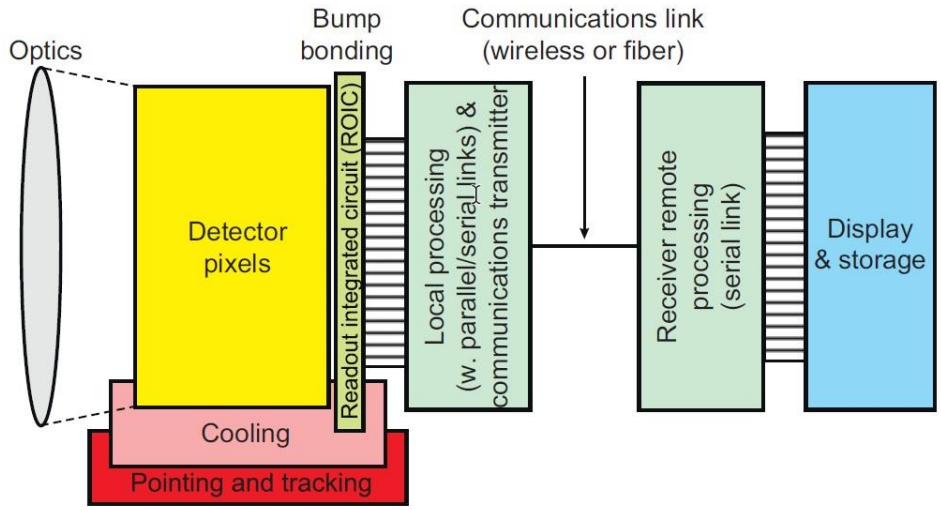

Figure 1. 9 Position of pixel detectors and the remaining components in an IR imaging system.[2]

Depending on the requirement and cost, FPA can be categorized as having hybrid or monolithic architectures. In the monolithic type, the external read-out circuit is not

responsible for multiplexing. Either a charge-coupled device (CCD) or a complementary metal-oxide semiconductor (CMOS) is the fundamental element of the monolithic array. More information and a schematic of this type of FPA are given elsewhere.[2] Although the CCD has the highest pixel counts of above 10^9, CMOS is rapidly approaching these high values. In hybrid FPAs, detectors are fabricated by flip-flop bonding or loophole interconnection on different substrates. Thus, optimization of the detector material and the multiplexer can be done independently.[2] FPA nominally have a Moore's law growth rate but with a 5-10 years lag.[2]

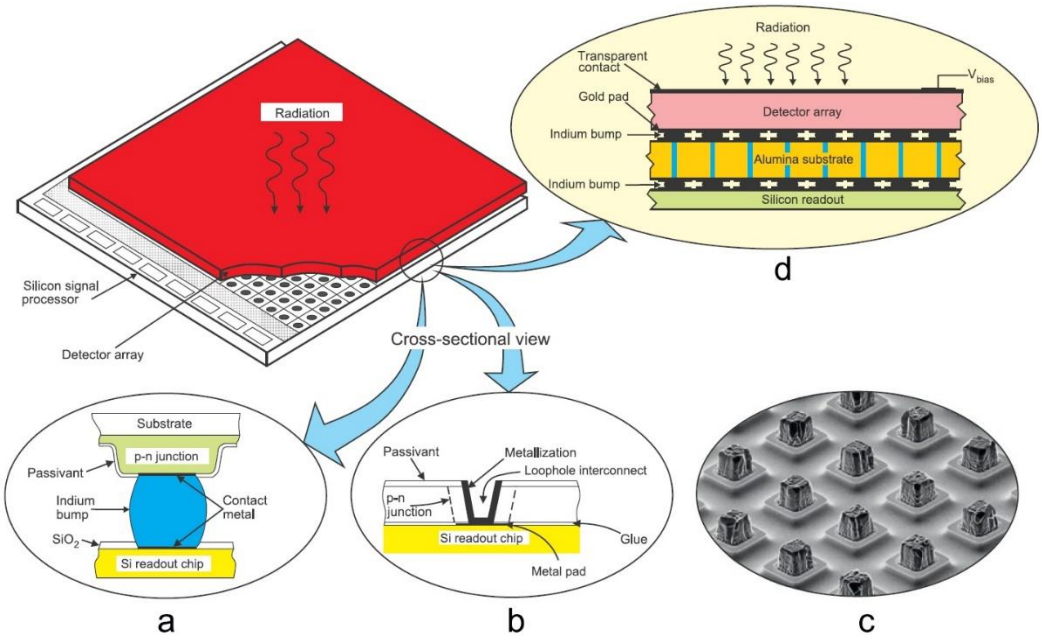

Figure 1. 10 Hybrid IR FPA: (a) Indium bump technique, (b) Loophole technique, (c) SEM image of indium bumps, and (d) Layer hybrid design for large format far-IR.[2]

Significant progress has been made over the years on FPA fabrication. First-generation linear FPAs involved scanning the scene across the linear array to generate an image with no multiplexing functions on the focal plane, as illustrated in Fig. 1.10. Second-generation detectors are based on 2D arrays[2]. In the 1990s, the challenges for

advanced IR imaging motivated the development of third-generation FPAs. The third-generation FPAs provide smaller pixel size, faster frame rates, better thermal resolution, and multicolor functionality, which make larger-scale hybrid integration with multiplexing electronics more difficult.[2,5] This detector generation includes both cooled and uncooled systems. Unfortunately, several major obstacles still hinder the development of the third generation of FPAs:[2,7,13]

- Difficulty in attaining relevant figure of merit in FPA: required temperature change of a scene; for production of signals equal to the root-mean-square of noise, i.e. noise-equivalent difference temperature (NEDT);
- Difficulty in deploying two/three-color detector structures in cheap small size pixels;
- Uniformity impacts accurate temperature measurement. Standard deviation over the mean for counted number of operable pixels in an array is used to quantify uniformity;
- Identification and detection ranges; third-generation IR detectors are necessary to provide technological advantage over enemy forces during night operations. This means further extension of the range of target detection and identification.

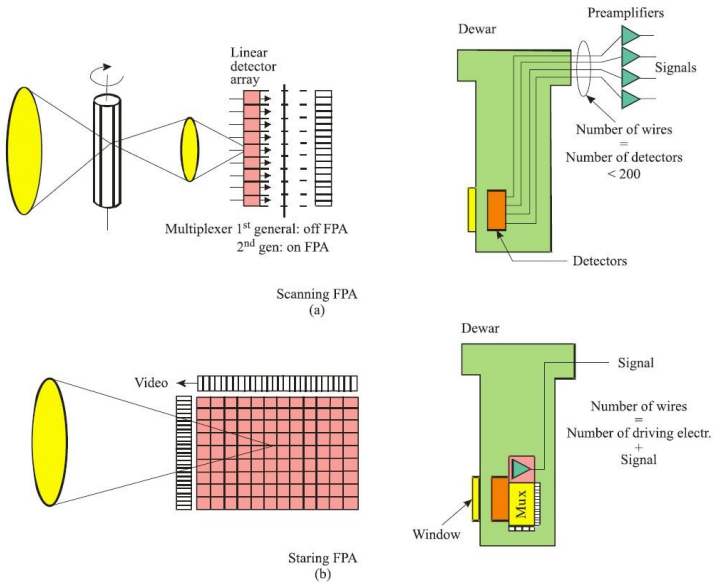

Figure 1. 11 FPA: (a) 1st generation, and (b) 2nd generation.[1,5,11]

The architecture of dual/multi-color third-generation FPA is based on a stacked arrangement of detectors where the shorter wavelength detector is located right after the substrate. Each detector is transparent to the upper wavelength and only collects signals to its cut-off wavelength. The signals can be collected sequentially or simultaneously. Figure. 1.12 schematically shows the simplest two-color IR detector architecture.[13]

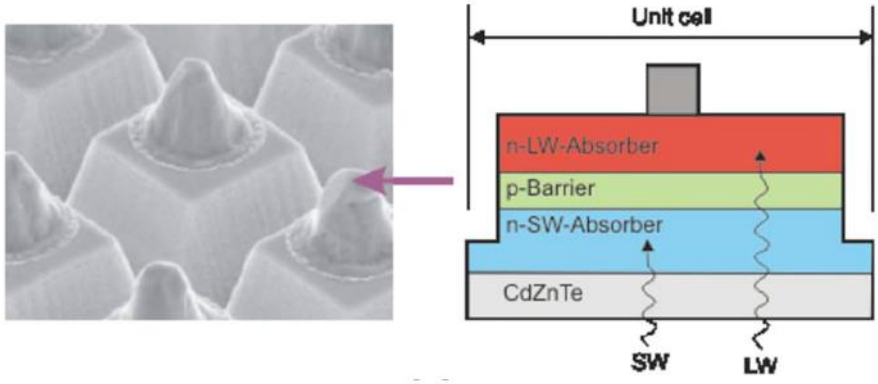

Figure 1. 12 Cross-section view of back-illuminated dual-band HgCdTe detector with bias-selectable *n-p-n* structure.[13]

1.7. Outline of dissertation

The research of this dissertation has concentrated on the characterization of defects in Hg-related IR materials (i.e. HgCdTe, HgCdSe) using advanced electron microscopy techniques, especially high-resolution transmission electron microscopy (HRTEM), two-beam bright-field imaging, and high-resolution scanning transmission electron microscopy (HRSTEM).

This dissertation research is separated into three major parts, according to the material of interest: i) characterization of HgCdTe heterostructures grown on Si (211); ii) correlation of etch pits and dislocations in HgCdTe (211) films; and iii) characterization of HgCdSe (211) heterostructures grown on Si and evaluation of etchants for development of etch-pit-density measurements.

Chapter 1 has provided the introduction and motivation for this research and introduced some basic concepts.

Chapter 2 summarizes important experimental aspects of this dissertation, including preparation of samples, and electron-microscopy-based characterization methods.

Chapter 3 investigates the effectiveness of HgTe buffer layers in blocking the threading dislocations in HgCdTe/CdTe/ZnTe/Si(211) heterostructures.

Chapter 4 describes an investigation of correlation of etch pits and dislocations in HgCdTe(211) for both as-grown material and after thermal-cycle-annealing as a post-processing technique for reduction of defects. The major results from this part of the research have been published elsewhere.[17]

Chapter 5 provides microstructural studies in HgCdSe/ZnTe/Si(211) heterostructures, which are being considered as an alternative material to HgCdTe. Early attempts to use etchants for delineation of dislocations in HgCdSe and etch pits was also investigated. The results of this research have been submitted for publication.

Chapter 6 summarizes microstructural characterization of other related samples including type-III HgTe/CdTe superlattices grown on Si (211) substrates and HgCdTe/CdZnTe (211) heterostructures.

References

[1]A. Rogalski, Opto-Electron. Rev. **20(3)**, 279-308 (2012).

[2]A. Rogalski, Prog. Quantum Electron. **36**, 342-473 (2012).

[3]E. P. G. Smith, R. E. Bornfreund, I. Kasai, L. T. Pham, E.A. Patten, J. M. Peterson, J. A. Rotha, B. Z. Noshoa, T. J. De Lyon, J. E. Jensena, J. W. Bangs, S. M. Johnson and W. A. Radford, Proc. of SPIE **Vol. 6127 61271F-1**, 8 (2006).

[4]W. D. Lawson, S. Neilson, E. H. Putely, and A. S. Young, J. Phys. Chem. Solids. **9**, 325 (1959).

[5]A. Rogalski, Rep. Prog. Phys. **68**, 2267-2336 (2005).

[6] M. A. Kinch, J. Electron. Matter. **39**, 1043 (2010).

[7]A. Rogalski, Infrared Phys. Technol. **50**, 240-252 (2007).

[8]P. Norton, Opto-Electron. Rev. **10(3)**, 159-174 (2009).

[9]G. L. Hansen, J. L. Schmit, and T. L. Casselman, J. Appl. Phys. **53**, 7099 (1989).

[10]M. A. Kinch, Fundamentals of Infrared Detector Materials. 67 (2007).

[11]W. Lei, J. Antoszewski, and L. Faraone, Appl. Phys. Rev. **2**, 041303 (2015).

[12]P. Capper, and J. Garland, Mercury Cadmium Telluride Growth, Properties and Application. 159-161 (2011).

[13]A. Rogalski, J. Antoszewski, and L. Faraone, J. Appl. Phys. **105**, 091101 (2009).

[14]J. W. Garland, S. Sivananthan, Springer Handbook of Crystal Growth. Chapter 32, 1070-1121 (2010).

[15]J.R. Arthur, Surf. Sci. **500**, 189-217 (2002).

[16]W. F. Zhao, R. N. Jacobs, M. Jaime-Vasques, L. O. Bubulac, and D. J. Smith, J. Electron. Mater. **40**. 1733 (2011).

[17]M. Vaghayenegar, R. N. Jacobs, J. D. Benson, A. J. Stoltz, L. A. Almeida, D. J. Smith, J. Electron. Mater. **46**. 5007 (2017).

CHAPTER 2

EXPERIMENTAL DETAILS AND METHODS

This chapter presents an overview of sample preparation methods suitable for electron microscopy examination of HgCdTe/CdTe/ZnTe/Si(211) and HgCdSe/ZnTe/Si(211) heterostructures. A brief overview is provided of transmission electron microscopy (TEM) techniques, including selected-area electron diffraction (SAED), conventional bright-field TEM, two-beam imaging, high-resolution transmission electron microscopy (HRTEM), scanning transmission electron microscopy (STEM), high-angle annular-dark-field (HAADF) imaging, and energy-dispersive X-ray spectroscopy (EDS), which are used frequently in the experimental studies described in later chapters.

2.1. Traditional TEM Specimen Preparation

The traditional method of cross-sectional TEM (XTEM) specimen preparation consists of mechanical polishing, dimpling and finally Ar-ion milling. The detailed steps involved are as follows. First, a piece of the specimen wafer is placed on a glass slide with melted liquid wax in an oven at a temperature of 90°C. A rotating diamond blade is then used to slice the wafer, usually along <011> direction. Two small pieces or one small piece and an Si-dummy are then glued face-to-face using Gatan M-bond adhesive. A specimen clamp is used to press the two pieces against each other to form a thin uniform glue line. A 30-min curing process in an <90°C oven is then implemented. Standard mechanical polishing is then applied. The first side is gently polished using with abrasive-diamond decreasing grain size lapping films of 6μm, 3μm, 1μm, 0.5μm, and

0.1μm, until a scratch-free mirror-like surface is achieved. The approximate thickness removals for each lapping film are as follows: 100μm for 6-μm film, 50 μm for 3-μm film, 15 μm for 1-μm film, 5-7 μm for 0.5-μm, and 1-2 μm for 0.1-μm. Platen speed during polishing should be maintained at or below 40 rpm for first-side polishing. Application of Green-lube as an effective lubricant during the last stage of polishing helps in obtaining a scratch-free surface. Since HgCdTe is a soft material, it is important to avoid using 9-μm film for the first-side polishing. The specimen is then washed several times with deionized water, dried with compressed air, and then flipped over for the second side to be polished. 9-μm lapping film is used to reduce the thickness to 300-250 μm, and 3-μm and 1-μm films eventually reduce the thickness to a range of 90-100 μm. A Cu-wheel and a cloth-wheel are then used for dimpling the specimen to thicknesses of 10-12 μm. Due to possible crack formation in thin composite films, pushing the dimpling further to reduce the thickness below 10 μm is not recommended. The center of dimpling should preferably lie on the center of the sample to avoid crack formation and damage in the thick film. Figure 2.1 illustrates the approximate region where the center of dimpling should be set, in this case for examination of a thick HgCdTe absorber layer. Finally, the specimen should be argon-ion-milled at an ion energy of 2.5 keV and a milling angle of 7° while held at liquid nitrogen temperature[1], to perforate a hole and make an electron-transparent region. A final low-kV (1.9-2 keV) milling for 5-10 min is always implemented to reduce surface amorphization and minimize ion-beam-induced damage in the specimen.[1]

Although this traditional method (i.e. mechanical polishing, dimpling and ion-milling) is usually successful, it still has some disadvantages for milling HgCdTe

composite films. The process is tedious, time-consuming, with low success rate because of sample fragility, and cannot be applied to a specific site (e.g. across a certain region of a device).[2] Moreover, the final region of interest will usually have a thickness gradient from very thin close to the perforated hole to thicker areas.[2] In situ lift-out using focused ion beam (FIB) is a technique that addresses these problems and is discussed in the next section.

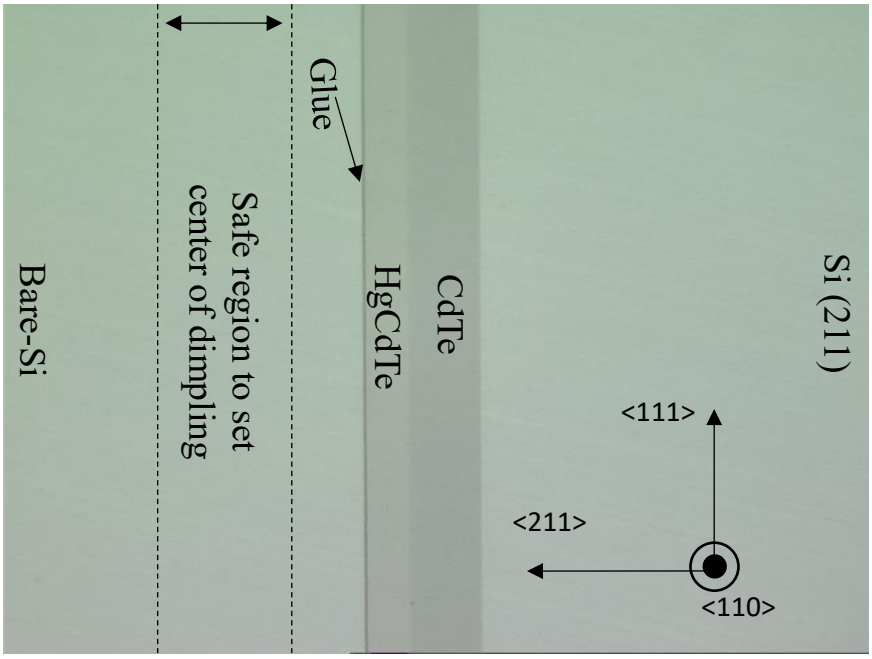

Figure 2. 1 Optical micrograph of polished sample with safe region marked for setting the dimpling center.

2.2. Dual-beam SEM and Focused Ion Beam (FIB)

The dual-beam FIB is a powerful tool that combines the imaging capabilities of SEM with the milling, deposition and imaging capabilities of the FIB. Figure 2.2 is a schematic showing the combination of SEM and FIB in a dual-beam system.[3] A liquid

metal ion source, usually gallium, at the top of the FIB column is used for production of ions, which are focused by an electric field and pass through different apertures and are then scanned over the sample surface for the purposes of etching, milling, deposition and imaging.[3]

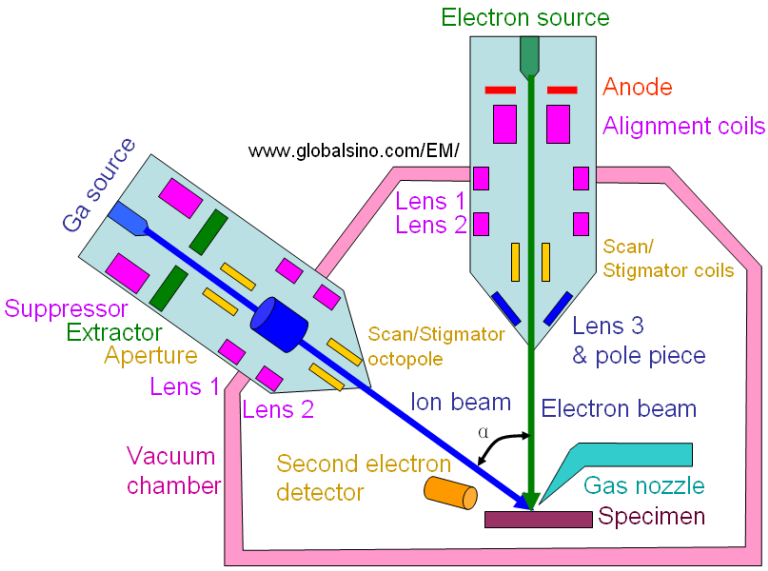

Figure 2. 2 Schematic of a dual-beam FIB-SEM system.[3]

Since these energetic ions are significantly heavier than electrons, see Table 2.1, their greater momentum can be implemented for precise and controlled removal of surface material, i.e. milling.[3] Moreover, when a vapor of organometallic compound is injected in a controlled manner close to the sample, the FIB can be used for precise and efficient materials deposition. Figure 2.3 schematically shows the deposition of Pt on a surface using ions. Depending on the penetration depth and work function of the sample, these high-energy ions can also transfer energy to electrons in the sample and cause them to escape. These secondary electrons provide surface imaging capabilities in the ion-

mode similar to the electron mode.[3] Table 2.1 provides a quantitative comparison between Ga^+ ions and electrons in the typical dual-beam FIB-STEM.[3]

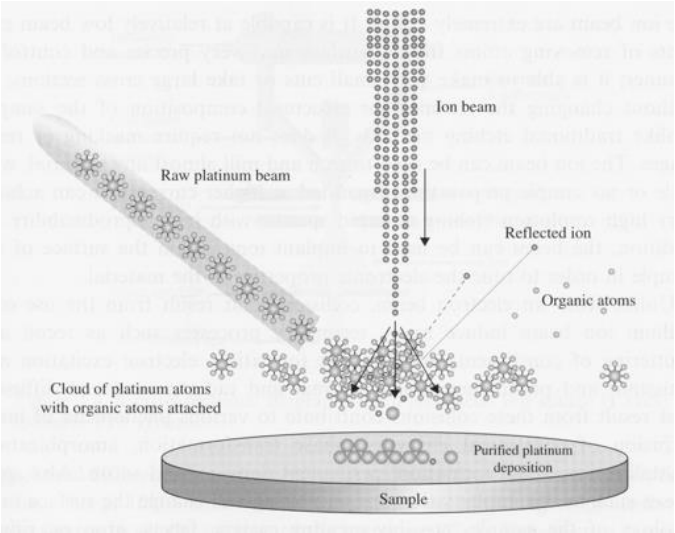

Figure 2. 3 Schematic of ion-beam-induced Pt deposition process inside an FIB.[3]

Particle	FIB	SEM	Ratio
Type	Ga^+ ion	Electron	
Elementary charge	+1	−1	
Particle size	0.2 nm	0.00001 nm	20 000
Mass	1.2×10^{-25} kg	9.1×10^{-31} kg	130 000
Velocity at 30 kV	2.8×10^{5} m/s	1.0×10^{8} m/s	0.0028
Velocity at 2 kV	7.3×10^{4} m/s	2.6×10^{7} m/s	0.0028
Velocity at 1 kV	5.2×10^{4} m/s	1.8×10^{7} m/s	0.0028
Momentum at 30 kV	3.4×10^{-20} kg m/s	9.1×10^{-23} kg m/s	370
Momentum at 2 kV	8.8×10^{-21} kg m/s	2.4×10^{-23} kg m/s	370
Momentum at 1 kV	6.2×10^{-21} kg m/s	1.6×10^{-23} kg m/s	370
Beam			
Size	nm range	nm range	
Energy	up to 30 kV	up to 30 kV	
Current	pA to nA range	pA to μA range	
Penetration depth			
In polymer at 30 kV	60 nm	12000 nm	0.005
In polymer at 2 kV	12 nm	100 nm	0.12
In iron at 30 kV	20 nm	1800 nm	0.11
In iron at 2 kV	4 nm	25 nm	0.16
Average signal per 100 particles at 20 kV			
Secondary electrons	100–200	50–75	1.33–4.0
Backscattered electron	0	30–50	0
Substrate atom	500	0	infinite
Secondary ion	30	0	infinite
X-ray	0	0.7	0

Table 2. 1 Quantitative comparison of Ga ions and electrons.[3]

For several practical reasons, gallium is favored over other ion sources for FIB milling.[2,3] These can be summarized as follows: Gallium requires limited heating due to its low melting temperature, its heavy mass makes it effective for milling, it provides a long source life of about 400 µA-hours/mg, and finally it can be used in its pure form rather than alloyed due to its low vapor pressure.[3] With pressure from the semiconductor industry for faster milling time for larger volumes, Plasma-FIB (PFIB) with other sources (e.g., Xenon) has recently been developed and commercialized.[4]

2.2.1. *In situ* Lift-Out FIB Specimen Preparation

When an *in situ* sample micromanipulator is installed on a dual-beam system, TEM lamellae can be prepared completely from beginning to the end within the dual-beam chamber. The full details and steps for FIB lamella preparation are briefly summarized as follows. First a thin layer of carbon is deposited on the sample. This will be followed by site-specific deposition of a thin layer of Pt (~300nm) in electron mode at 5kV with 1.6nA, and a thicker layer of Pt (2-3µm) using Ga ions at 30kV with 0.1nA beam current. The length and width of the Pt stripe can be varied but it is typically ~ 10 µm length and 1.2 µm width. Trench milling at 30kV is then done on both sides of the Pt-deposited area. To decrease side-wall damage, this milling is usually performed in a step-wise manner. Milling starts with 7nA at about 3µm away from the deposited area, then continues with 3nA at about 1µm away, and is finally completed at 1nA until the milling window reaches the sides of the Pt stripe. This process is illustrated in Fig 2.4. The depth of the trenches in all steps is usually the same and will be determined by the thickness of the film or the features that will be imaged in the final lamella. After the base and side walls are undercut through, the micromanipulator will then place a tungsten needle on the slice

and make a gentle touch down. When Pt-welding of the needle on top of the sample is completed, it will be cut free and lifted out. The lamella will eventually be mounted on a Cu-grid and thinned at 0.1nA at 30kV with Ga^+ ions. In order to reduce the effect of Ga^+ amorphization, a final milling with 5kV and 72pA is normally implemented.

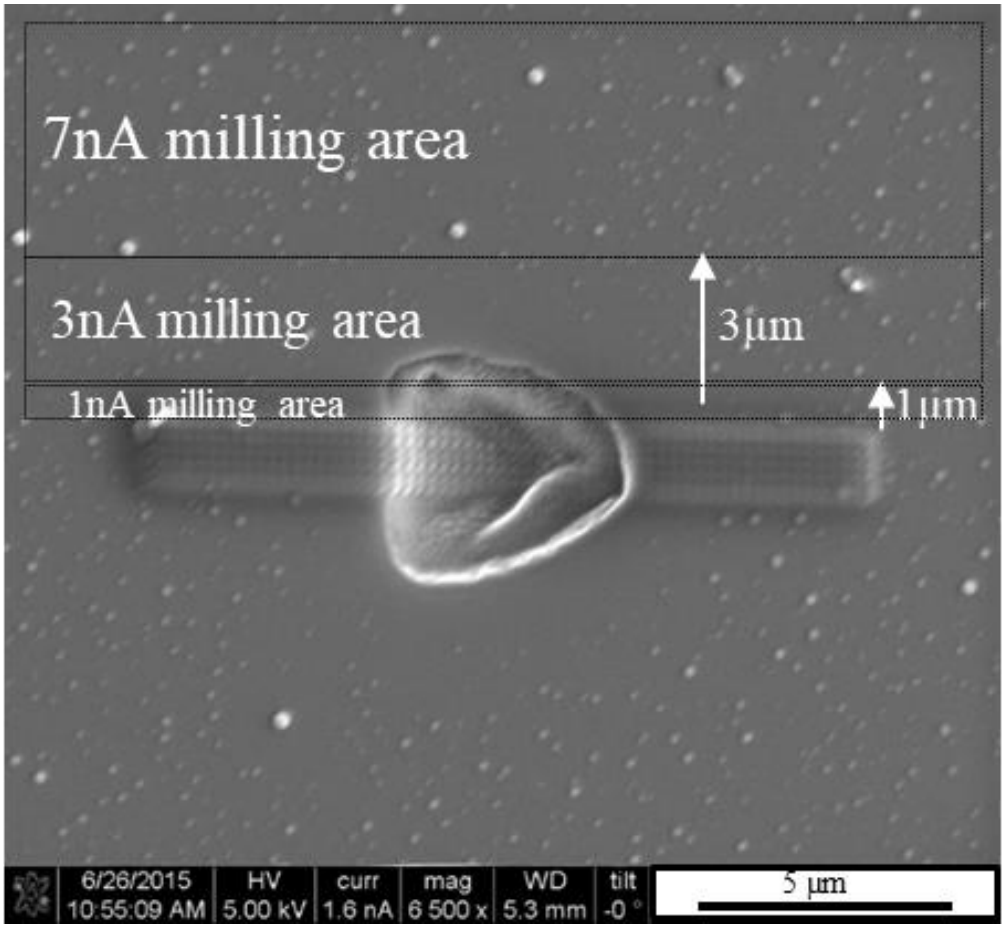

Figure 2. 4 SEM image showing dimensions of different regions adjacent to an etch pit in HgCdSe which is coated with e-beam-deposited Pt. Boundaries for each milling condition are indicated.

2.3. (Scanning) Transmission Electron Microscopy Techniques

The transmission electron microscope uses a wide range of signals originating from highly energetic electrons that interact with thin specimens, leading to images or spectra that contain structural, chemical and electronic information. Figure 2.5 summarizes these signals schematically.[5]

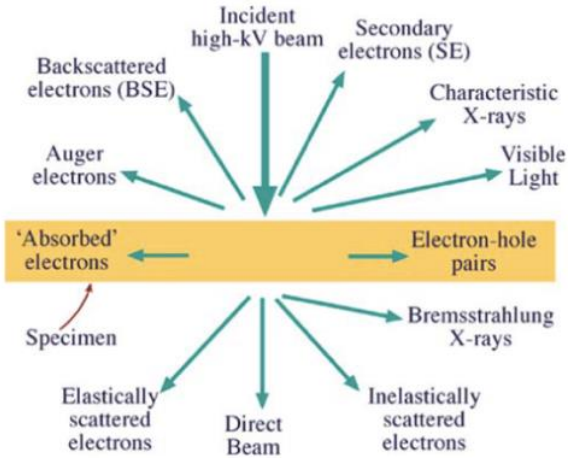

Figure 2. 5 Schematic showing many of the signals generated from interaction of electrons with matter. Directions are depicted in a relative manner.[5]

The major techniques for electron microscopy can be summarized as: selected-area electron diffraction (SAED), conventional bright/dark-field TEM, convergent-beam electron diffraction (CBED), high-resolution TEM (HRTEM), scanning transmission electron microscopy (STEM), high-angle annular-dark-field-imaging (HAADF) also known as Z-contrast imaging, energy-dispersive X-ray spectroscopy (EDS), and electron energy-loss spectroscopy (EELS). In this section, a brief overview of SAED, conventional bright-field TEM, two-beam imaging and dislocation visibility criteria, HRTEM, STEM, HAADF and EDS is provided.

2.3.1. SAED

Bragg's law specifies how a fast electron beam that is passing through a thin crystalline sample will create a diffraction pattern after exiting the sample. A distribution of scattered intensity is formed at the back focal plane of objective lens from the electrons that are elastically scattered at small angles (typically ≤ 1 to 2°) with respect to the undeviated transmitted beam. This pattern, which is formed at the back focal plane of the objective lens, can be magnified and projected onto the final viewing screen camera by the proper alignment and focusing of intermediate and projector lenses beneath the objective lens. To confine the information acquired to a selected small portion of the specimen, for example near an interface, an aperture is inserted at the first intermediate image plane. Diffraction patterns provide a wide range of useful specimen information, such as crystallinity, phase identification, and orientation relationships between different materials.[5-7]

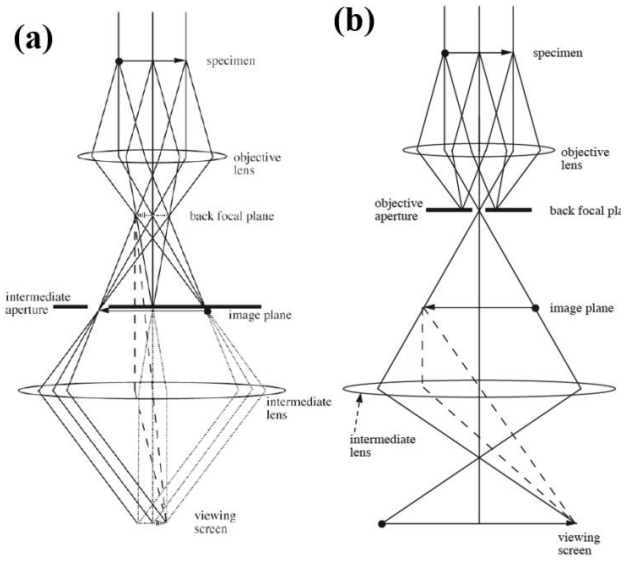

Figure 2. 6 (a) Geometry and ray diagram for selected-area electron diffraction (SAED); and (b) Geometry and ray diagram for TEM imaging.[7]

2.3.2. Bright-Field Imaging in TEM

Bright-field images are formed when an objective aperture is inserted in the back focal plane of the objective lens. When the objective aperture selects only the transmitted beam and no diffracted beams, the image formed is called bright-field (BF). This imaging mode is commonly known as amplitude or diffraction contrast. When a specific diffracted beam is selected, the image formed is referred to as dark-field (DF). These two imaging modes are of paramount importance for imaging defects in materials.[5,7]

2.3.3. Two-Beam Bright-Field Imaging

The two-beam condition refers to a situation where the sample is tilted so that a specific diffracted beam is excited in addition to the central transmitted beam. This geometry is the preferred mode of imaging for studying defects such as dislocations in transmission electron microscopy.[5,7] This condition is shown both experimentally and schematically in Fig. 2.7.

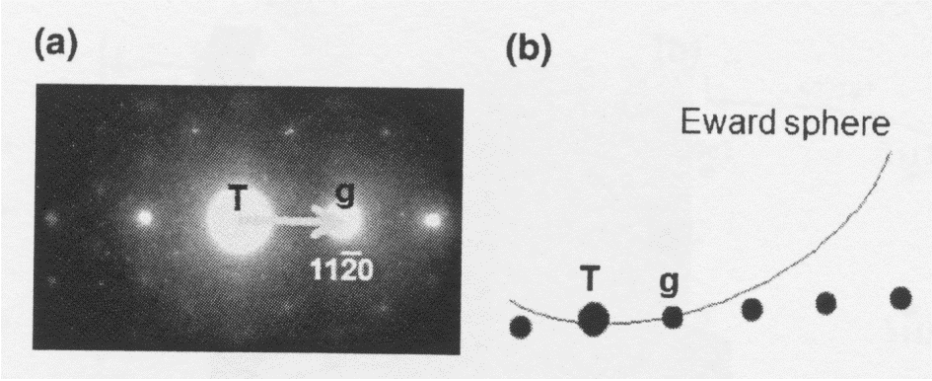

Figure 2. 7 (a) Two-beam condition in an hcp material with a <0001> zone axis, and 11$\bar{2}$0 beam excited, (b) Two-beam condition and Ewald sphere.[8]

In a crystalline material, translational vectors associated with the displacement of atoms from their regular position are used to describe many types of defects. The

kinematical amplitude of electron scattering from a crystal is given in equation 2.1, where s is the excitation error, r_i is the atomic coordination vector, g is the scattering vector, and R is the displacement vector for the defect.[9]

$$\psi \sim \int_{Crystal}[\exp(2\pi i s.r_i)\exp(2\pi i g.R)]dt \quad (2.1)$$

Thus, the phase factor $2\pi\mathbf{g}.\mathbf{R}=n2\pi$ where n can be zero, fractional, or integer, modifies the amplitude scattered by the crystal. The special case of $\mathbf{g}.\mathbf{R}=0$ is of central importance in studying defects. For specific **g**, when the displacement vector **R** lies in the reflecting plane, such that the path difference between the diffracted and transmitted waves is unaffected, i.e. $\mathbf{g}.\mathbf{R}=0$, then the condition for zero contrast for displacement vector **R** is met. For dislocations, the displacement vector **R** can be replaced by the Burgers vector **b**, so that the invisibility criteria becomes $\mathbf{g}.\mathbf{b}=0$.[9]

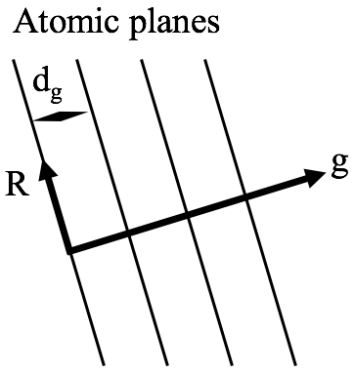

Figure 2. 8 Schematic illustrating the disappearance of dislocation contrast under the g.R=0 condition.[10]

The Burgers vector for a specific dislocation is fixed but one can simply change the value of $2\pi\mathbf{g}.\mathbf{b}$ by varying the value of **g**. This can be simply done in a microscope equipped with a double-tilt holder, which allows tilting the specimen to different two-

beam conditions, where the strongly excited beam is different in each case. Depending on the specific **g** vector, the contrast of the dislocation may change. In practice, if the dislocation goes out of contrast under two different two-beam diffracting conditions, $\mathbf{g}_1$ and $\mathbf{g}_2$, then the Burgers vector can be determined using $\mathbf{b}=\mathbf{g}_1\times\mathbf{g}_2$. Table 2.2 give an example of different **g**.**b** values for perfect and imperfect dislocations for face-centered-cubic (FCC) crystal structure.[9] This imaging technique was essential for completing the defect studies described in chapter 4.

Plane of Dislocation	b	g.b		
		g=		
		$1\bar{1}1$	$\bar{1}11$	$11\bar{1}$
$(1\bar{1}1)$ or $(1\bar{1}\bar{1})$	$\frac{1}{2}[110]$	0	0	1
$(1\bar{1}\bar{1})$ or $(11\bar{1})$	$\frac{1}{2}[101]$	1	0	0
$(1\bar{1}1)$ or $(11\bar{1})$	$\frac{1}{2}[011]$	0	1	0
(111) or $(11\bar{1})$	$\frac{1}{2}[1\bar{1}0]$	1	$\bar{1}$	0
(111) or $(1\bar{1}1)$	$\frac{1}{2}[10\bar{1}]$	0	$\bar{1}$	1
(111) or $(\bar{1}11)$	$\frac{1}{2}[0\bar{1}1]$	1	0	$\bar{1}$

Table 2. 2 Values of **g**.**b** for perfect dislocations in FCC crystals.[9]

2.3.4. High-Resolution Electron Microscopy (HREM)

In contrast to amplitude or diffraction contrast mode, the HREM imaging mode uses a large objective aperture (or sometimes none at all). Thus, the image formation process is the result of interference between the direct transmitted beam and diffracted beams. Since the relative phases of the various beams determine the image contrast, the HREM imaging mode is often referred to as phase-contrast imaging.[11] In this mode, individual atomic columns of crystalline materials can nowadays be easily resolved. However, image interpretability in terms of the projected crystal potential depends heavily on many factors such as the spherical aberration coefficient C_s, defocus, and image astigmatism as well as the sample thickness.[11] Due to the complex nature of the interference, image simulations are often required for image interpretation. Electrons that interact with a thin crystalline sample oriented at a high-symmetry-low-index zone axis contain valuable information about the specimen. However, the objective lens will affect the electrons during their transfer to the recording medium (e.g., CCD camera). This effect, which is specimen-independent, can be modeled with a mathematical function known as the phase-contrast transfer function (PCTF). The PCTF has an oscillatory nature, and intuitive image interpretation beyond the first crossover, known as interpretable image resolution, can be quite complicated difficult due to contrast reversals.[11]

2.3.5. Scanning Transmission Electron Microscopy (STEM)

STEM imaging is different from TEM imaging. In TEM the specimen is illuminated with a wide almost-parallel beam of electrons, and imaging is done in parallel, whereas imaging in STEM is done by accumulating the image in serial fashion as a fine

electron probe is scanned across the specimen. These fundamental differences are depicted schematically in Fig 2.8.

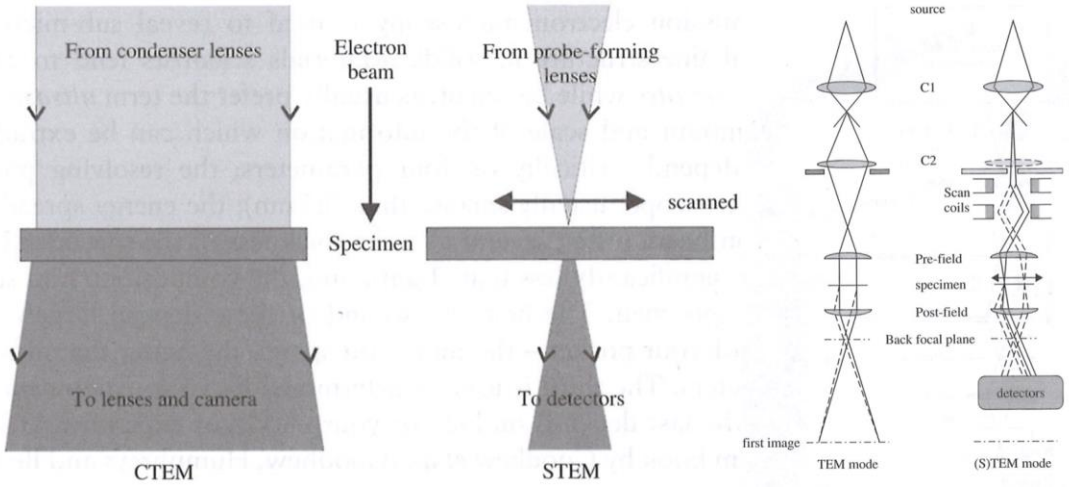

Figure 2. 9 Right: Electron beam paths in TEM and STEM. Left: Comparison of TEM and STEM imaging modes.[12]

The ability to collect information in a point-by-point manner makes the STEM an ideal tool for performing analytical microscopy with high spatial resolution. Depending on the position and geometry of the detector, STEM imaging can be performed in annular-bright-field (ABF), annular-dark-field (ADF), medium-angle-annular-dark-field (MAADF) and high-angle-annular-dark-field (HAADF).

2.3.6. High-Angle Annular-Dark-Field (HAADF)

The first point-by-point imaging of individual heavy atoms on an amorphous substrate used an annular-dark-field detector.[12] The ADF signal largely comes from Rutherford scattering by the atomic nuclei, so that the image intensity is a function of both atomic number and the number of atoms illuminated by the beam. The initial ADF detectors were not effective for acquiring interpretable images when applied to crystalline

samples, since they collected a mixture of incoherently scattered and Bragg diffracted electrons. This problem was later resolved by enlarging the inner angle of the ADF detector to exceed typical Bragg diffraction angles. Use of an ADF detector with a larger inner angle, i.e. high-angle-annular-dark-field (HAADF), excludes almost all diffraction contrast and provides an almost purely Z-contrast condition.[12] In practice, the annular range for collection of scattered electrons in HAADF is in the range of 50-200 mrad. In this context, these relatively few large-angle Rutherford-scattered electrons are mostly beyond any diffraction spots of significant intensity and are therefore insensitive to orientation and structure. However, their strong dependence on atomic number Z, with the intensity varying as $Z^{ß}$, $1.5<ß<2$, makes them ideal for determining the location of heavy atoms.[12]

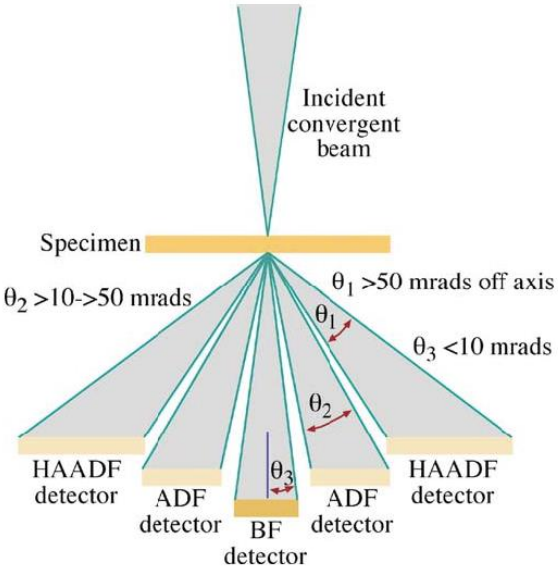

Figure 2. 10 Schematic of different detectors in STEM and their corresponding collection scattering angle.[5]

HAADF has become the most common mode of STEM imaging due to its ease of image interpretation. With the recent advent of aberration-corrected STEM, compositional information at the atomic scale is possible using the HAADF mode.

2.3.7. Fundamentals of EDS

When a TEM specimen is illuminated by a fine probe of electrons, many atoms are excited into higher energy states as a result of inner-shell ionization by the high-energy incident electrons. Following excitation, relaxation can occur by emission of characteristic X-rays or Auger electrons due to transition of electrons from higher energy levels into the vacancy created in the inner shell. The transition energy (ΔE) between the excited and relaxed states corresponds to characteristic X-ray wavelengths ($\lambda = hc/\Delta E$) which are finger-prints for the atom, and allow for elemental identification. The typical EDS detector consists of a silicon drift detector located within a few mm of the sample surface and roughly in the same plane to maximize collection of the characteristic X-rays. The collected X-rays are converted to electrical pulses proportional to their energy, which are then processed for chemical composition analysis.[12] Figure 2.10 illustrates the relaxation mechanism for generation of characteristic X-rays for an atom which has undergone K-shell ionization by an energetic electron. Characteristic X-rays are labeled depending on the inner-shell excitation: using Bohr's term involved K, L, M, N, etc, and the subsequent filling electrons from lower-binding levels: α, ß, γ, as well as subscripts 1, 2, 3.[12]

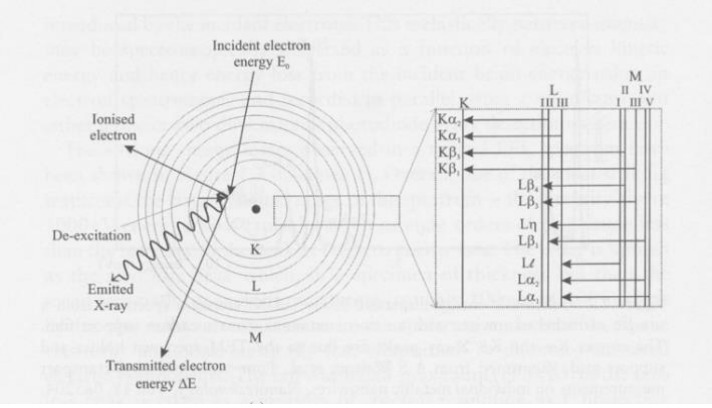

Figure 2. 11 Relaxation mechanism for an atom that has that has undergone K-shell ionization by a high energy incident electron.[12]

2.3.7. Instrumentation

Four transmission electron microscopes and one dual-beam (FIB/SEM) at the John. M. Cowley Center for High Resolution Electron Microscopy were used in the research described in this dissertation. Figure 2.11 shows photographs of these microscopes. The 400 keV JEOL JEM-4000EX high-resolution electron microscope, and the Philips-FEI CM-200 were used to collect diffraction contrast and HRTEM images. HAADF STEM images and EDS spectrums were acquired with 200keV JEOL JEM-2010F and 200keV JEOL JEM-ARM200F which are both equipped with and energy-dispersive X-ray spectrometer (EDS). The Nova 200 FEI nanolab system were used for site-specific TEM lamella preparation.

Figure 2. 12 Microscopes used for the research described in this dissertation.

References

[1]C. Wang, D. J. Smith, S. Tobin, T. Parados, J. Zhao, Y. Chang, S. Sivananthan, J. Vac. Sci. Technol. A 24, **995** (2006).

[2]L. A. Giannuzzi, Introduction to Focused Ion Beam, Springer, New York (2005).

[3]N. Yao, Focused Ion Beam Systems Basics and Applications, Cambridge University Press, Cambridge (2007).

[4]A. Garnier, G. Filoni, T. Hrncir, L. Hladik, Microelectron. Reliab. **55**, 2135-2141 (2015).

[5]D. B. Williams, and C. B. Carter, Transmission Electron Microscopy A textbook for Materials Science 2nd edition, Springer, (2009).

[6]C. B. Carter, and D. B. Williams, Transmission Electron Microscopy Diffraction, Imaging, and Spectrometry, Springer, (2016).

[7]B. Fultz, and J. M. Howe, Transmission Electron Microscopy and Diffractometry of Materials 3rd edition, Springer, (2008).

[8]T. Yao, and Soon-Ku Hong, Oxide and Nitride Semiconductors Processing, Properties, and Application, Springer, (2009).

[9]G. Thomas, and M. J. Goringe, Transmission Electron Microscopy of Materials, Wiley–Interscience, New York, (1979).

[10]Z. L. Wang, and Z. C. Kang, Functional and Smart Materials Structural Evolution and Structure Analysis, PLENUM PRESS. New York and London, (1998).

[11]J. Hutchison and A. Kirkland, Nanocharacterization, RSC Publishing, (2007).

[12]R. Brydson, Aberration-Corrected Analytical Transmission Electron Microscopy, RMS-Wiley Imprint, (2011).

CHAPTER 3

STRUCTURAL CHARACTERIZATION of HgCdTe/HgTe/CdTe/ZnTe/Si(211) GROWN BY MOLECULAR BEAM EPITAXY

This chapter describes the characterization of MBE-grown HgCdTe/HgTe/CdTe/ZnTe/Si(211) heterostructures grown by molecular beam epitaxy (MBE). This project was carried out in collaboration with Dr. Yuanping Chen and colleagues at Army Research Lab (ARL) who provided the materials that were studied.

3.1. Introduction

Mercury cadmium telluride, $Hg_{1-x}Cd_xTe$ (MCT), has been the primary material used for infrared (IR) detectors and sensors due to its superior physical and electronic properties.[1-2] Cadmium zinc telluride, CdZnTe (CZT), has been the preferred substrate for MCT growth for many years due to its close lattice-match with MCT, and it remains the current substrate of choice for state-of-the-art MCT IR technology.[1] However, serious limitations such as larger defect densities (on the order of 10^5 cm^{-2}) which cause defects in MCT during growth, high price (300-400 $/$cm^2$), smaller available wafer sizes (~36-49 cm^2), and lack of major commercial suppliers, have combined to slow progress in the development of the next generation of IR focal plane arrays (FPAs). These shortcomings have motivated researchers to explore the possibility of growth on alternative substrates, such as Si, GaAs and GaSb.[3-6] Si is of much interest due to several attractive features which include lower price (0.56 $/$cm^2$), larger available wafer size (5228 cm^2), extremely low impurity levels, and compatibility with Si read-out circuits in a flip-chip bonded configuration.[3,7]

The Si (211) surface normal benefits from two energetically non-equivalent lattice sites for nucleation of polar semiconductors, which has made it a preferred substrate for growth of a range of II-VI semiconductors (e.g., ZnTe). However, direct epitaxial growth of MCT on Si will generate highly defective films due to the very large lattice mismatch (19.5%) between the two materials. Detector performance parameters such as operability, sensitivity, and uniformity among FPA are deteriorated through dislocation cores and segregated impurities that create surface charge and shunting paths.[8] Therefore, growth of composite layers of thick (>8μm) CdTe on thin (~15nm) ZnTe buffer layers with As-passivated Si (211) substrates was explored as an approach to entangle dislocations and effectively minimize defect propagation into MCT layers.[9] For long-wavelength IR applications, defect densities should ideally be suppressed below 5×10^5 cm^{-2}.[10]

In this chapter, the HgCdTe/CdTe/ZnTe/Si(211) system has been revisited to investigate the effect of growth of a thin HgTe buffer layer between HgCdTe and CdTe in order to block dislocation propagation into the MCT layer and to improve crystal quality. A series of microcopy techniques including low, medium and high magnification diffraction contrast imaging, high-resolution electron microscopy (HREM), high-angle annular-dark-field (HAADF) imaging, and energy-dispersive X-ray spectroscopy (EDS) were used for characterization.

3.2. Characterization of HgCdTe/HgTe/CdTe/ZnTe/Si(211) Heterostuctures

A series of five samples, listed in Table 3.1, were prepared by standard mechanical polishing and ion-milling for investigation in the <011> cross-sectional geometry. Details about cross-sectional XTEM sample preparation were explained in section 2.1. Figure 3.1 shows a schematic illustration (not to scale) of the sample geometry.

$Hg_{1-x}Cd_xTe$ Sample #	Intended Application	x-value	HgTe growth length	Absorber layer thickness (μm)	CdTe cap	EPD
		Cd %	seconds (s)			(*10^6 cm^{-2})
MCT021214	SWIR	0.445	15	5.85	yes	4.4
MCT022814	SWIR	0.438	0	5.71	yes	17
MCT030714	SWIR	0.432	60	5.72	yes	18
MCT062414	LWIR	0.213	60	4.22	no	26
MCT062614	LWIR	0.219	15	3.99	no	12

Table 3. 1 List of samples studied and their specification.

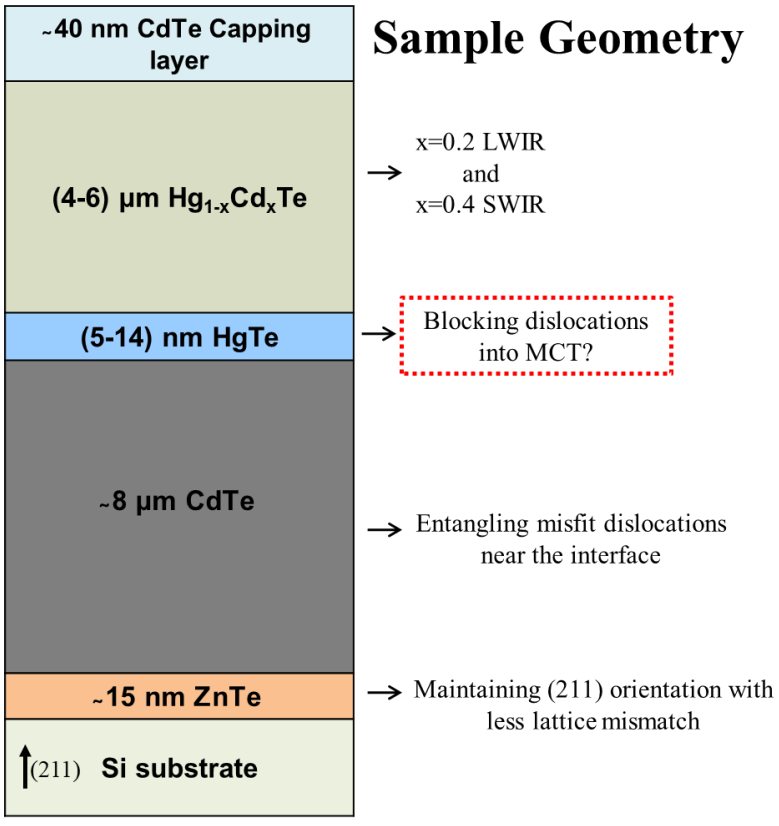

Figure 3. 1 Schematic illustration of the sample geometry (not to scale).

The microstructure in all samples is similar close to the substrate. Figure 3.2 shows a low magnification XTEM image of the CdTe/Si (211) region. A high density of defects due to the large lattice mismatch (i.e. 19.5%) is observed at the interface, but the density of defects drops off rapidly away from the substrate. Selected-area-electron-diffraction (SAED) patterns from this region indicate single crystalline growth with 3.7° rotation between the CdTe and Si crystal lattices. This angle is in good agreement with a recent structural model that proposed minimization of strain energy of closed-packed planes projected along the interface in (211)-oriented films.[11]

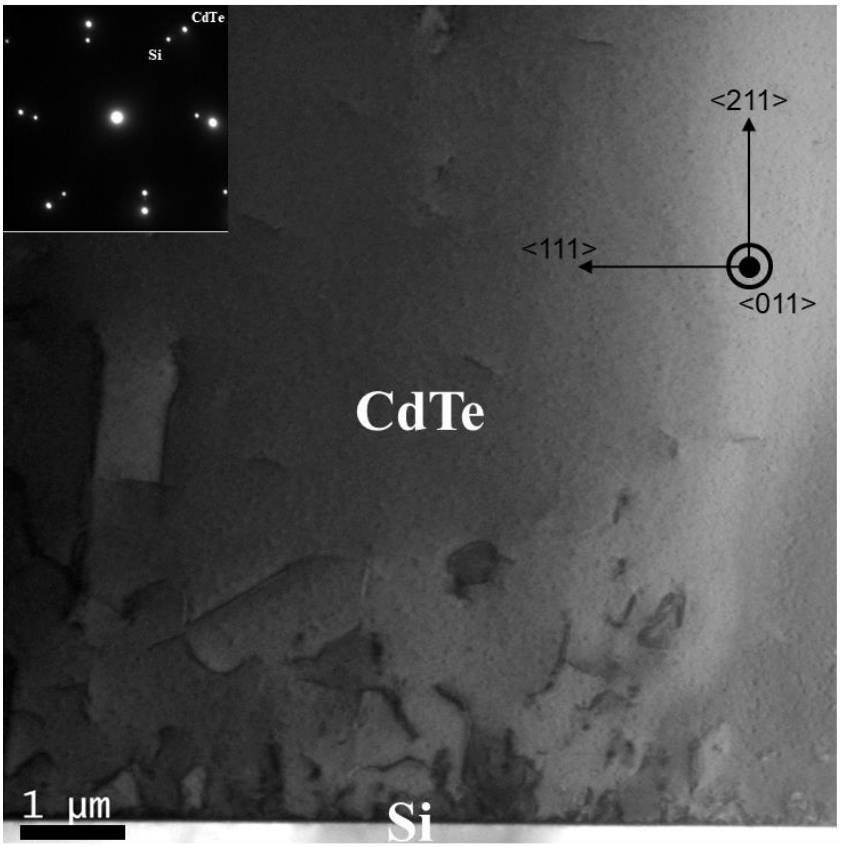

Figure 3. 2 Bright-field XTEM image of CdTe/Si interface; SAED pattern is inserted as an inset.

High-resolution imaging from the interface region shows a thin and defective buffer layer between CdTe and Si in all samples. After calibration of the image magnification based on Si lattice spacing, comparison of the interplanar spacing measured for 200 spots showed that the corresponding value matched closely with ZnTe.

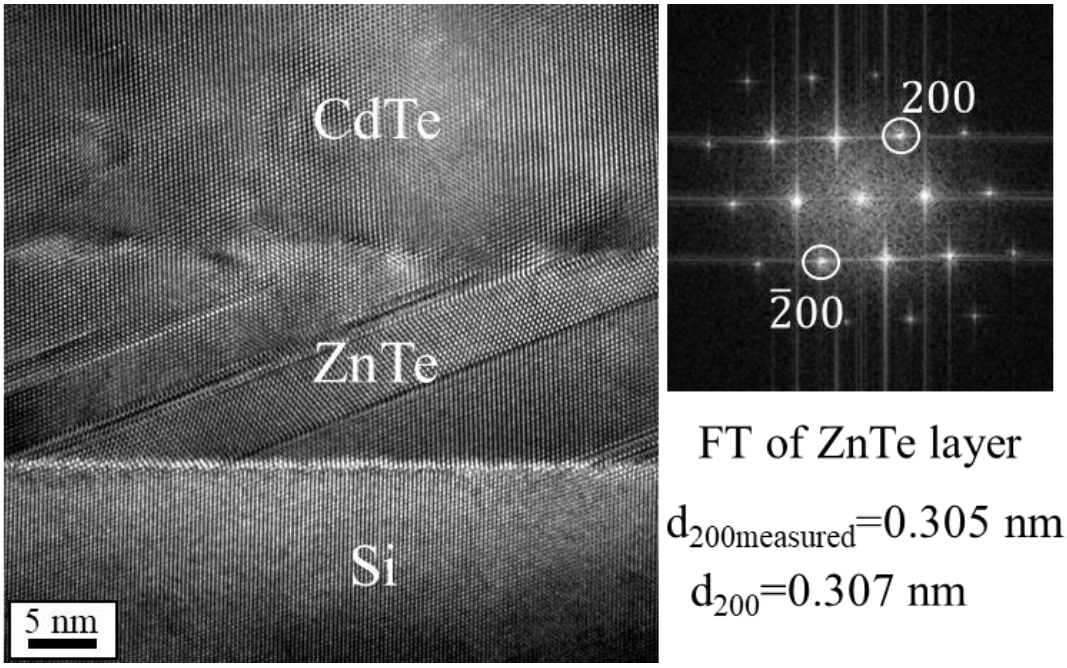

Figure 3. 3 High-resolution XTEM image of CdTe/Si interface with ZnTe buffer layer; Fourier Transform (FT) of ZnTe, and the measured and calculated d_{200} are shown on the right.

EDS line profiles were acquired along these interfaces to confirm the crystallographic measurements based on HRTEM images. Figure 3.4 shows the presence of the thin ZnTe layer in the EDS line scan. From the growth design point of view, the ZnTe buffer layer helps to mediate the large misfit strain between CdTe and Si due to its smaller lattice mismatch with Si (i.e. 12%).

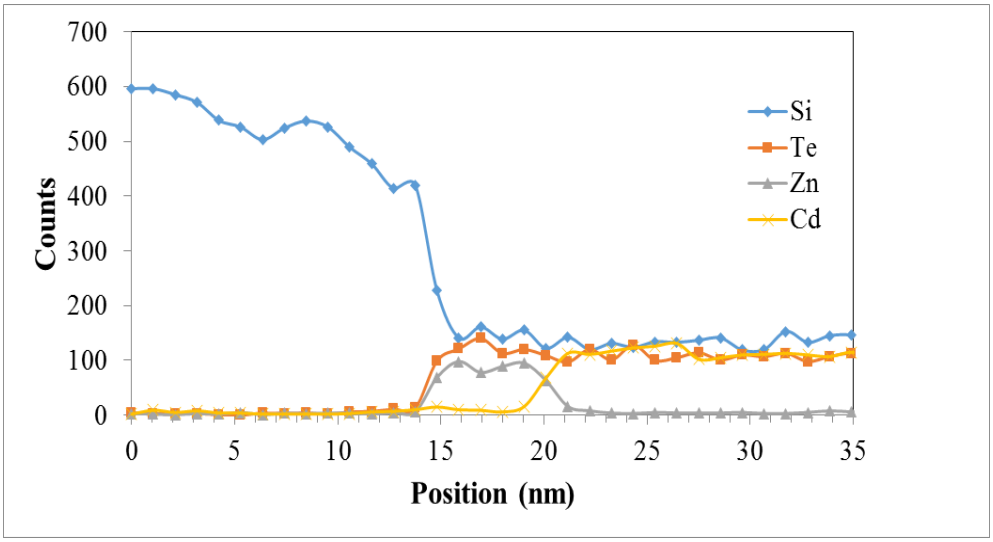

Figure 3. 4 EDS line profile along the CdTe/Si interface. The ZnTe thin layer is clearly revealed.

Figure 3.5(a) shows a low magnification XTEM image of the SWIR sample MCT022814, which had no HgTe buffer layer between HgCdTe and CdTe. Dislocations often thread from the bottom interface all the way into upper regions: a long and continuous defect (arrowed) threads from the HgCdTe/CdTe interface all the way through HgCdTe to the capping layer. Low-, medium- and high-magnification XTEM images show highly defective areas in the vicinity of the interface and also in the top capping layer which has an uneven top surface, see Figs. 3.5(b,c, and d). Similar imaging was done on other SWIR samples. Figures 3.6 and 3.7 show a series of low/medium magnification XTEM images of these samples. In both cases, the HgCdTe films seem to be less defective than the sample with no HgTe buffer layer, (i.e., MCT022814) as visible in Figs 3.6(a) and 3.7(a). Higher magnification XTEM images reveal the HgTe thin layer deposited during a 60-second growth interval, Fig. 3.6(c), whereas the HgTe buffer layer is not visible for the sample having the shorter, 15-second growth interval, Fig. 3.7(c, d).

For both samples with HgTe buffer layers, the capping layers seem to have reasonable quality, Fig. 3.6(b) and Fig. 3.7(b).

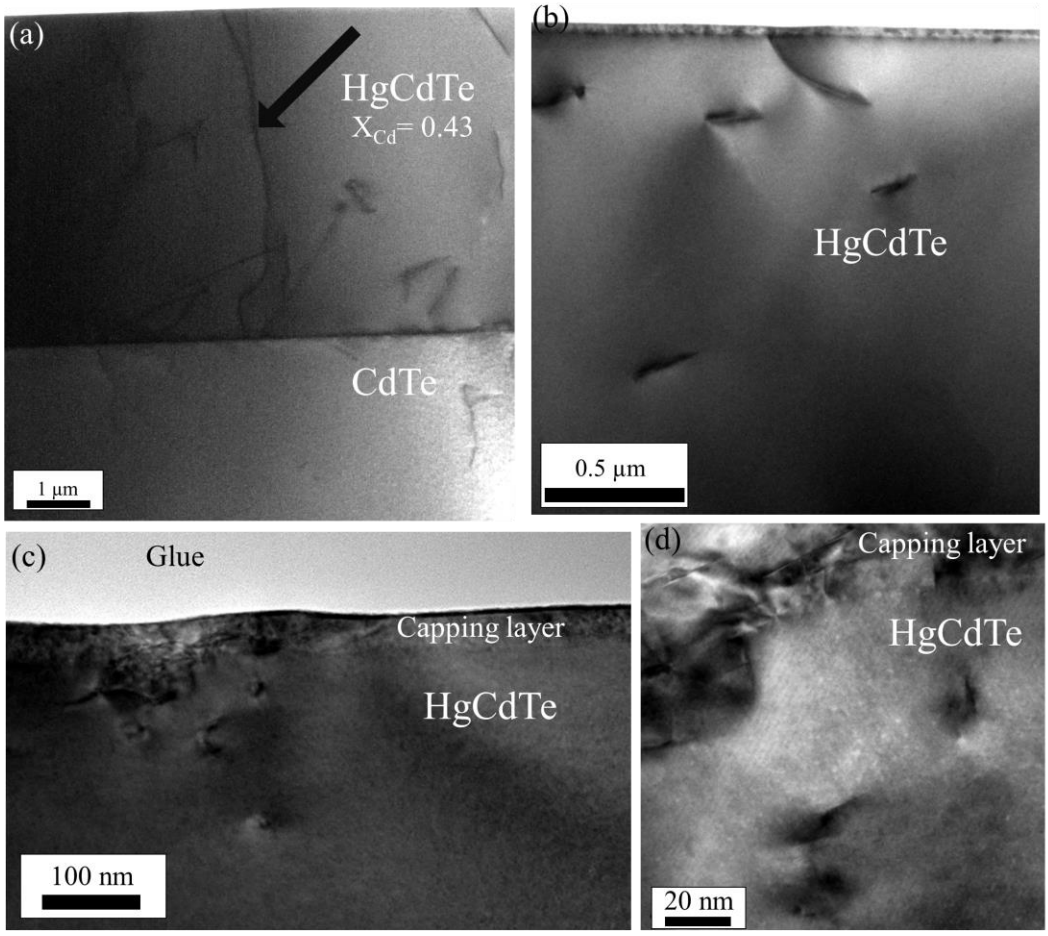

Figure 3. 5 XTEM micrographs for SWIR sample MCT022814: (a) Low-magnification XTEM image of MCT/CdTe. Long dislocation thread is marked with an arrow, (b) Low-magnification XTEM image of the upper region of MCT, (c) Medium-magnification image of the upper parts of the MCT layer, and (d) High-magnification image showing MCT/CdTe region.

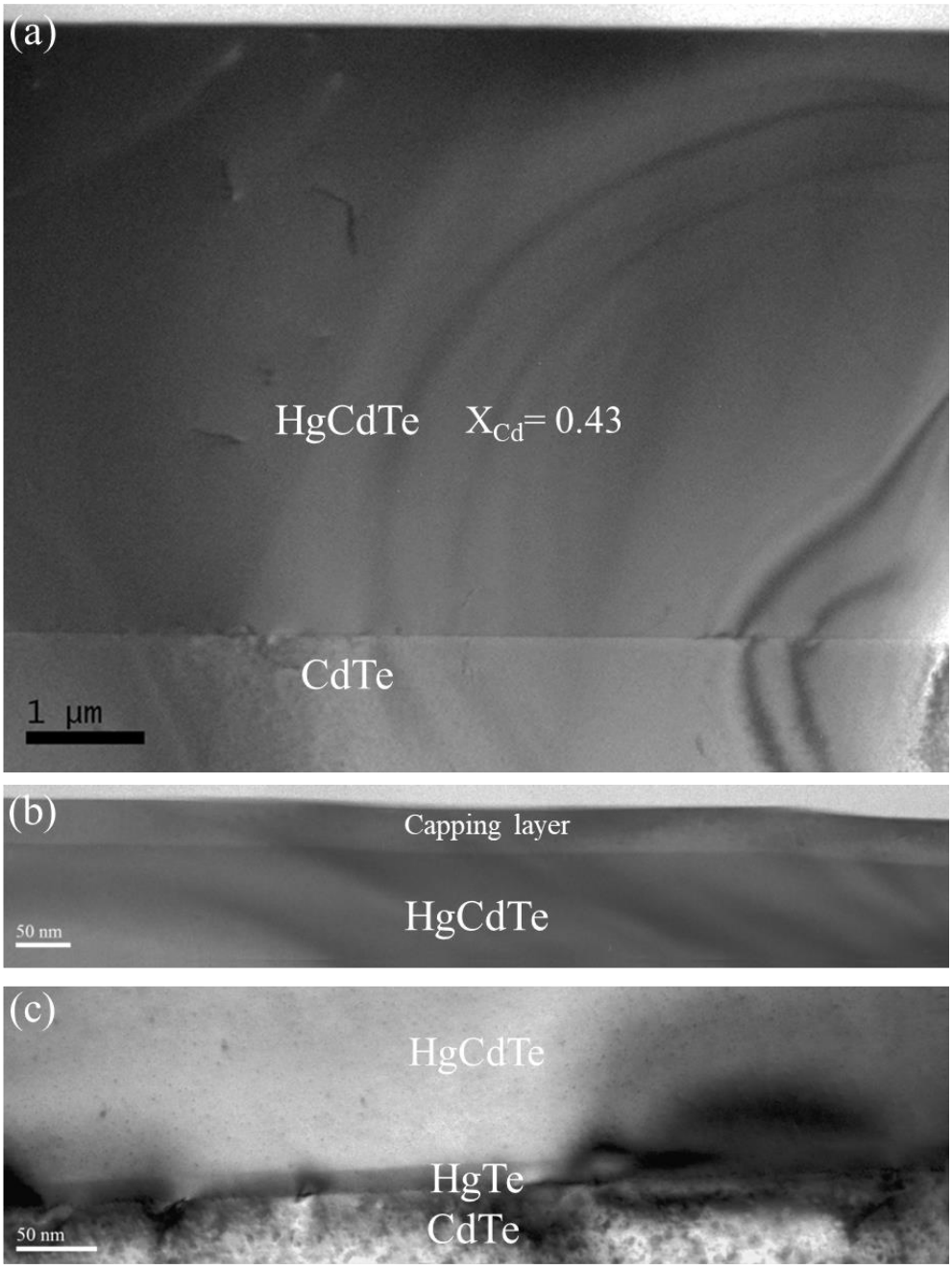

Figure 3. 6 XTEM micrographs for SWIR sample MCT030714 with thin HgTe spacer layer deposited during 60-s growth period. (a) Low-magnification XTEM image of MCT/CdTe, (b) Medium-magnification XTEM image showing the upper region of MCT with capping layer, and (c) Medium-magnification image of the MCT/CdTe interface, where the HgTe layer is clearly visible.

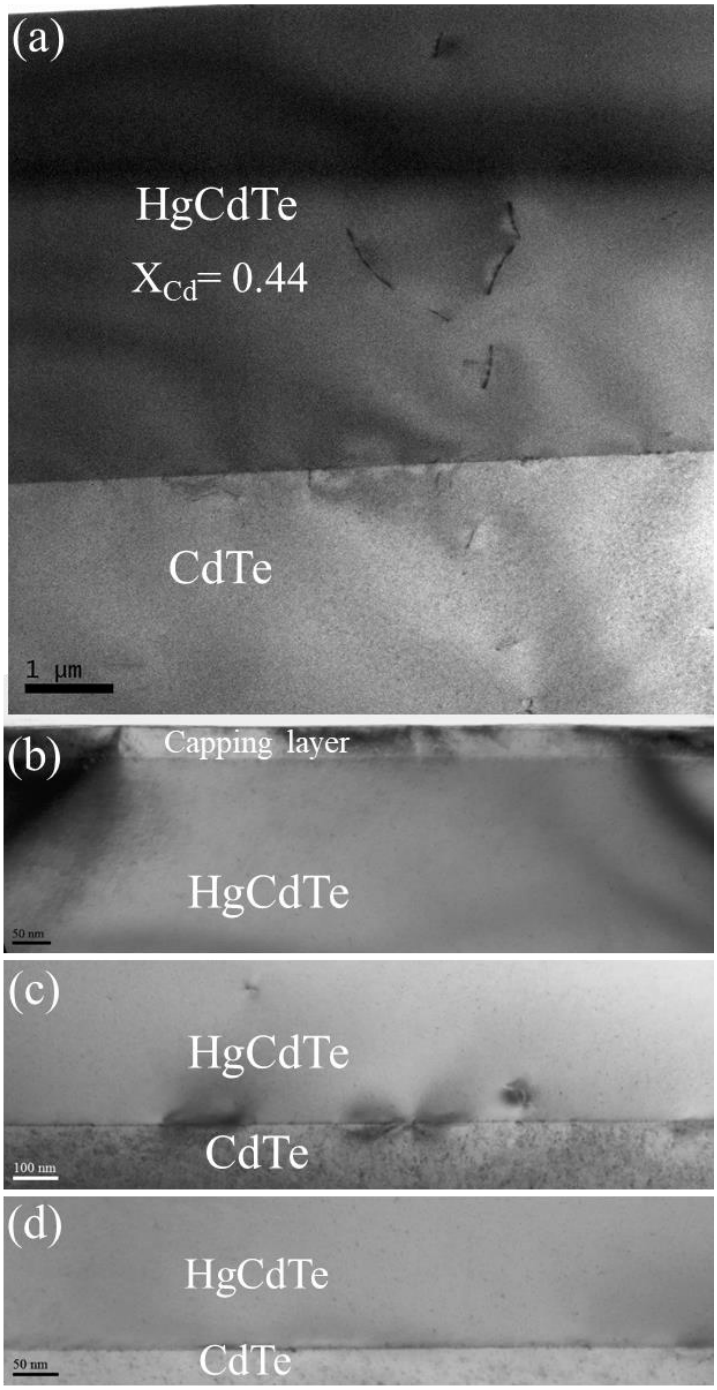

Figure 3. 7 XTEM micrographs for SWIR MCT030714 supposedly with HgTe spacer layer deposited during a 15-s growth period: (a) Low-magnification XTEM image of MCT/CdTe, (b) Medium-magnification XTEM image of the upper region of MCT with capping layer, and (c,d) Medium-magnification image of the MCT/CdTe interface.

Similar observations were made for the LWIR samples. In both samples observed, Figs 3.8(a) and 3.8 (c), the HgCdTe film seems to be of good structural quality with relatively few defects in the bulk of the film. Since BF diffraction-contrast imaging did not clearly reveal the thin HgTe layers, especially for the shorter growth period of 15s, the HAADF imaging technique was used to reveal the HgTe thin buffer layer. HAADF images, as shown in Figs. 3.9 & 3.10, confirmed the presence of HgTe in both samples.

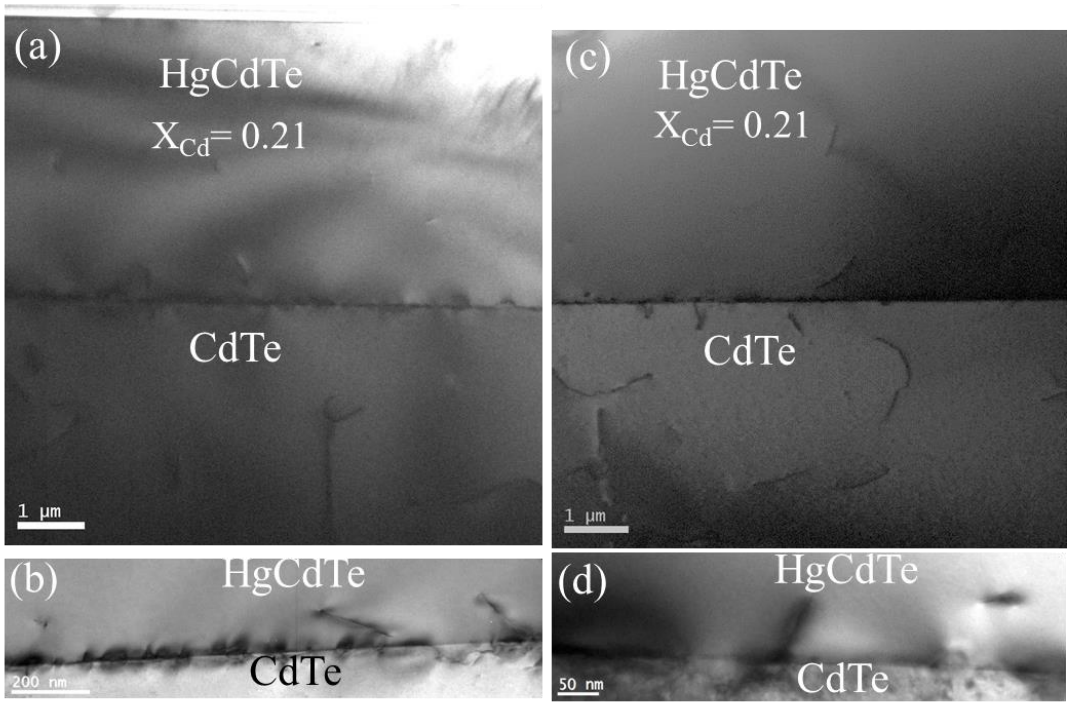

Figure 3. 8 XTEM micrographs for LWIR samples MCT062614 and MCT062414. MCT062614: (a) Low-magnification XTEM image of MCT/CdTe, (b) Medium-magnification XTEM image of the MCT/CdTe interface, MCT062414: (c) Low-magnification XTEM image of MCT/CdTe, and (d) Medium-magnification XTEM image of the MCT/CdTe interface.

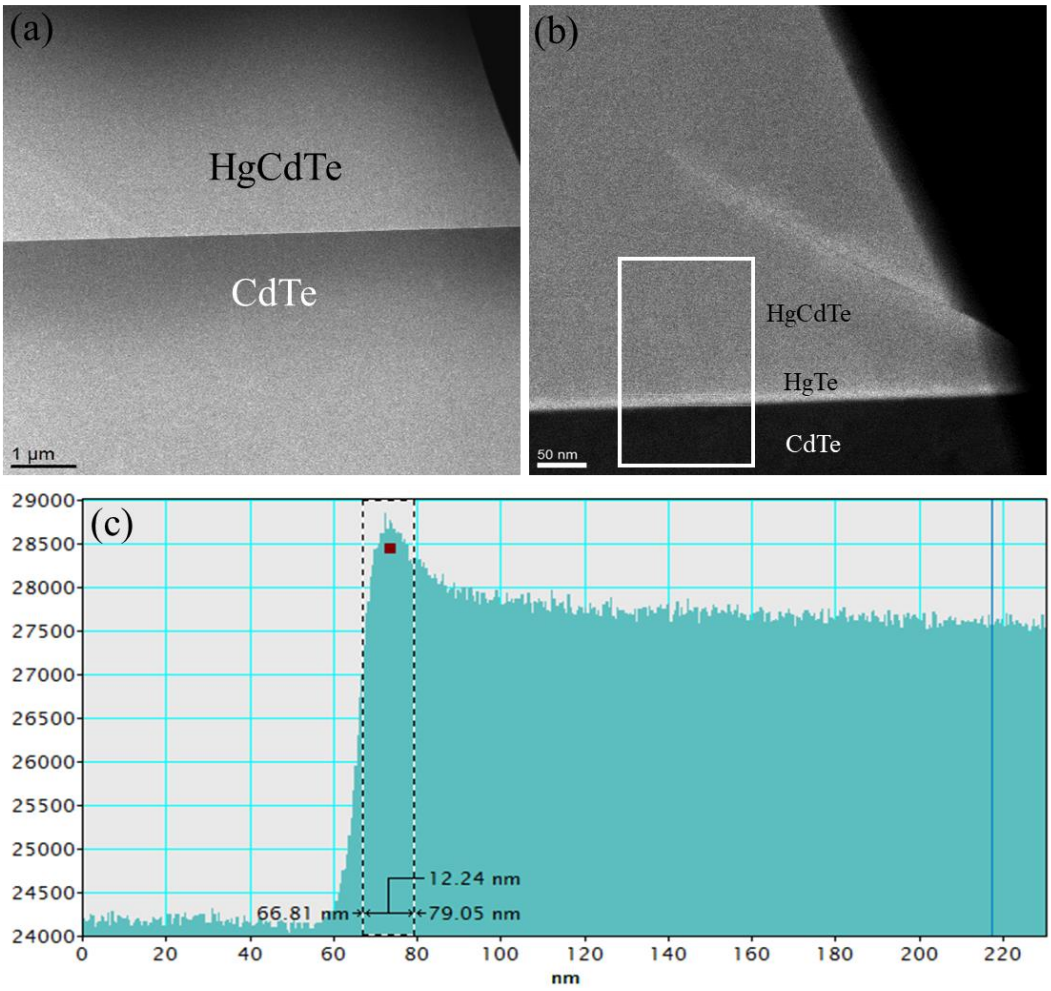

Figure 3. 9 Micrographs for sample MCT062414: (a) Low-magnification HAADF STEM image of HgCdTe/HgTe/CdTe, (b) Higher-magnification HAADF STEM image of HgCdTe/HgTe/CdTe, (c) Intensity profile of the boxed area in Fig 3.9(b).

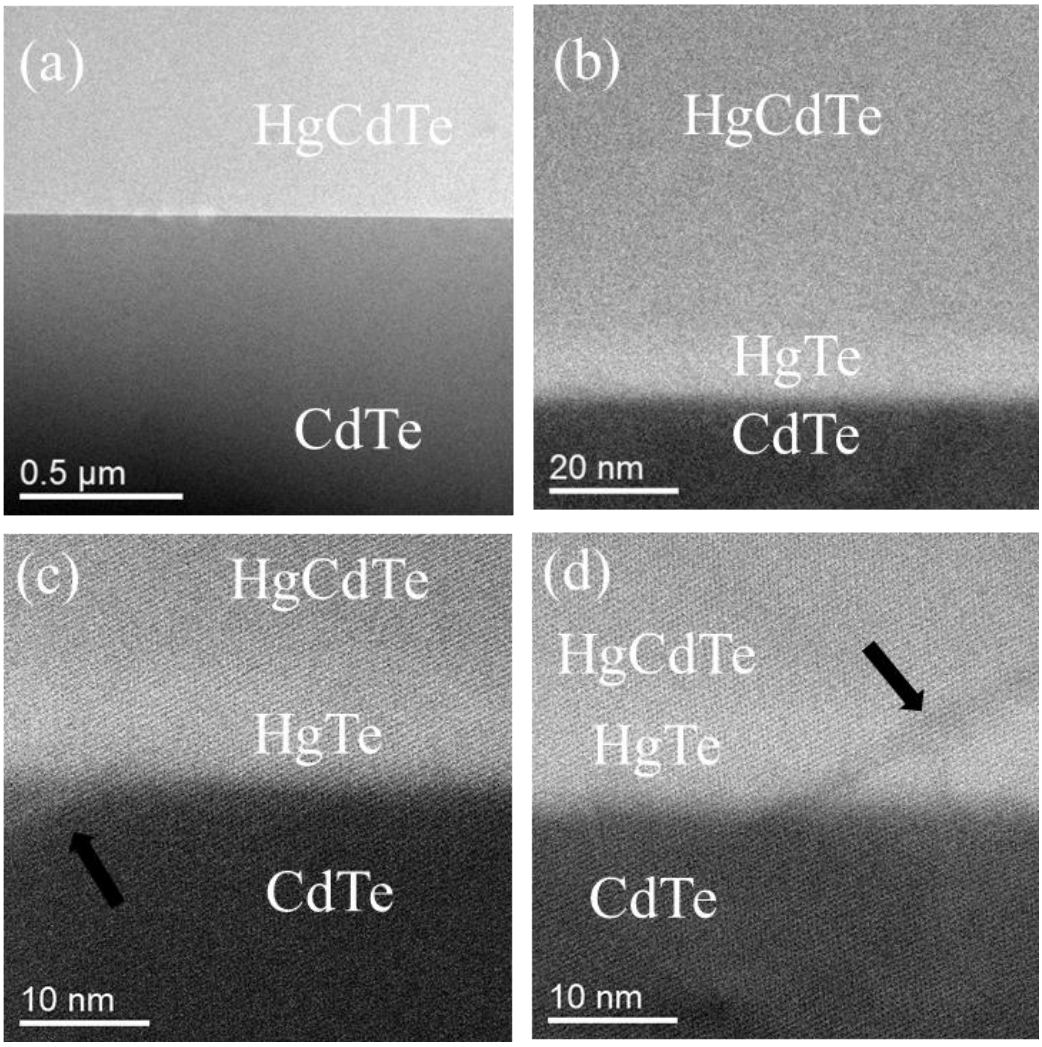

Figure 3. 10 Micrographs for LWIR sample MCT062614: (a) Low-magnification HAADF STEM image of HgCdTe/HgTe/CdTe, (b, c and d) Higher-magnification HAADF STEM image of HgCdTe/HgTe/CdTe from different areas.

The HgTe layer thickness for LWIR sample MCT062414 was measured to be ~12nm, but the upper interface for sample with the shorter growth interval was unclear in the HAADF images. This ill-defined interface is also unclear in the EDS line profiles, such as Fig 3.11, where elemental signals are noisy across the transition region.

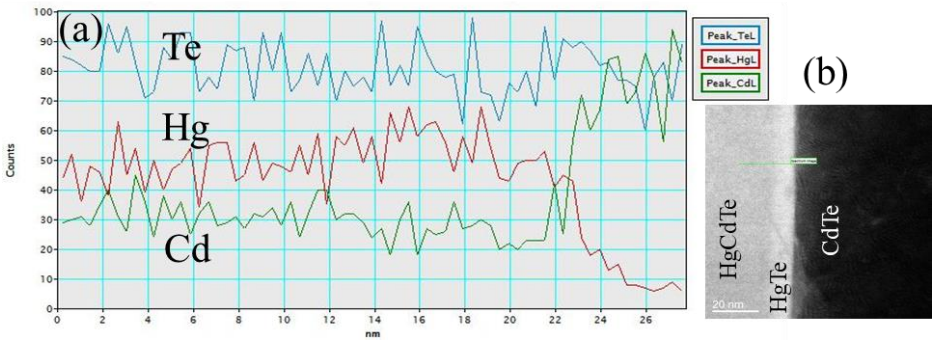

Figure 3. 11 (a) EDS line profile across HgCdTe/HgTe/CdTe for sample MCT062614, and (b) corresponding STEM HAADF image. Position of line profile is marked with green color.

Overall, it appears that the HgTe layer blocks some defects, but others seem to pass straight through, as visible in Fig. 3.10(d). A similar trend seems to be in effect for the SWIR sample, as shown in Figure 3.12.

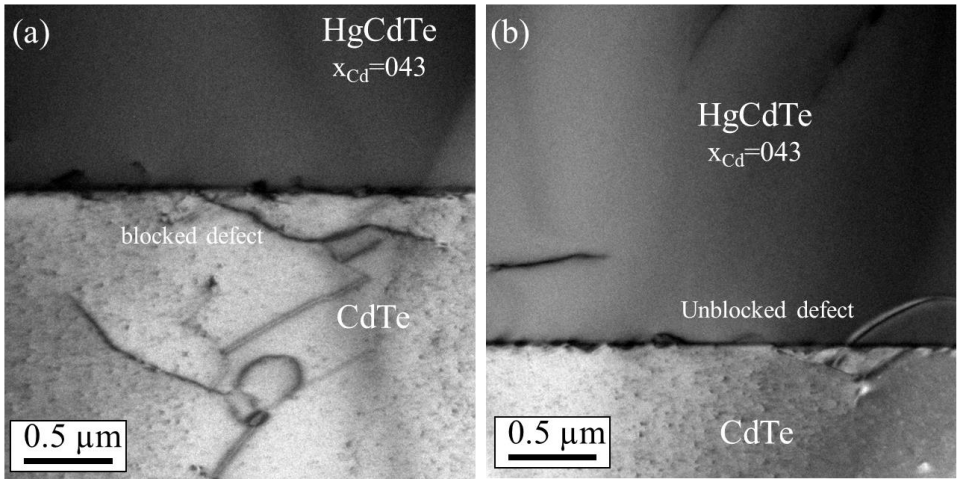

Figure 3. 12 XTEM micrographs for MCT030714: (a) successful blocking of defects, and (b) unsuccessful blocking of defects.

The absence of an LWIR sample with no HgTe buffer layer, and discrepancy between the etch-pit-density values in Table 3.1, weaken the hypothesis that increased HgTe buffer-layer thickness results in improvement of HgCdTe quality.

3.3. Discussion and Conclusions

Microstructural studies show large dislocation densities at CdTe/Si(211) interfaces in all samples, which drop off rapidly with increasing CdTe thickness. A lattice rotation of 3.7° between CdTe and Si is recorded in SAED patterns. XTEM and EDS micrographs show a thin (~15 nm) ZnTe buffer layer between CdTe and Si which serves to mediate the large lattice mismatch by lowering the misfit strain.

For the SWIR series, low magnification XTEM shows that the sample with no HgTe buffer layer between HgCdTe and CdTe is more defective, while samples with HgTe buffer layers have more defect-free areas. However, etch-pit-density measurements did not follow the same trend, low (i.e., 4.4×10^{6} cm^{-2}) for 15 seconds HgTe growth window sample and almost equal (i.e., 18×10^{6} cm^{-2} vs 17×10^{6} cm^{-2}) for the samples with 60 seconds, and no HgTe buffer layer. Hence, it cannot be concluded that the HgTe buffer layer reduces the density of defects in the HgCdTe layer.

For the LWIR series, the lack of a sample without an HgTe layer makes it difficult to draw any conclusion. In samples with short and long HgTe growth windows, XTEM images show high quality HgCdTe layer with few threading defects present in HgCdTe. Higher magnification diffraction contrast images did not show the presence of the HgTe buffer layer in either sample, although HAADF imaging did reveal the HgTe buffer layer with brighter contrast in both samples. Similarly, higher etch pit density values for the sample with longer HgTe growth window (i.e., 26×10^{6} cm^{-2}) compared to those for the shorter one (i.e. 12×10^{6} cm^{-2}) weaken the suggestion of better HgCdTe quality for the longer HgTe buffer layer growth window. In both SWIR and LWIR samples, the HgTe

buffer layer successfully blocks defects in some locations from passing through into the HgCdTe layer, but defects at other places are not blocked.

References

[1]A. Rogalski, J. Antoszewski, and L. Faraone, J. Appl. Phys. **105**. 091101 (2009).

[2]P. Norton, Opto-Electron. Rev. **10(3)**, 159-174 (2009).

[3]J. W. Garland, and S. Sivananthan, in Springer Handbook of Crystal Growth, ed. By G. Dhanaraj, K. Byrappa, V. Prasad, and M. Dudley, Springer Heidelberg Dordrecht London New York, Chapter 32. p. 1076 (2010).

[4]J. D. Benson, L. O. Bubulac, P. J. Smith, R. N. Jacobs, J. K. Markunas1 M. Jaime-Vasquez, L. A. Almeida, A. Stoltz, J. M. Arias, G. Brill, Y. Chen, P. S. Wijewarnasuriya, S. Farrell, and U. Lee, J. Electron. Mater. **41**. 2971 (2012).

[5]J. J. Kim, R. N. Jacobs, L. A. Almeida, M. Jaime-Vasquez, C. Nozaki, and David J. Smith, J. Electron. Mater. **42**. 3142 (2013).

[6]W. Lei, R. J. Gu, J. Antoszewski, J. Dell, and L. Faraone, J. Electron. Mater. **43**. 2788 (2014).

[7]A. Rogalski, J. Antoszewski, and L. Faraone, Appl. Phys. Rev. **2**. 041303 (2015).

[8]P. Wijewarnasuriya, Y. Chen, G. Brill, N. Dhar, D. Benson, L. Bubulac, and D. Edwall, J. Electron. Mater. **39**. 1110 (2010).

[9]W. F. Zhao, R. N. Jacobs, M. Jaime-Vasques, L. O. Bubulac, and D. J. Smith, J. Electron. Mater. **40**. 1733 (2011).

[10]K. Jówikowski, and A. Rogalski, J. Electron. Mater. **29**, 736 (2000).

[11]S. Y. Woo, G. A. Devenyi, S. Ghanad-Tavakoli, R. N. Kleiman, J. S. Preston, and G. A. Botton, Appl. Phys. Lett. **40**. 132103 (2011).

CHAPTER 4

CORRELATION OF ETCH PITS AND DISLOCATIONS IN HgCdTe(211) FILMS

This chapter describes the characterization of etch pits in as-grown and thermal-cycle-annealed HgCdTe(211) films. This project was carried out in collaboration with Dr. Randolph Jacobs and his colleagues at U.S. Army Night Vision and Electronic Sensors Directorate who provided the samples. The major findings of this study have been recently published.[2]

4.1. Introduction

The challenge to reduce dislocation densities in HgCdTe grown on alternative substrates such as Si rather than traditional CdZnTe substrates, has motivated researchers to explore strategies for reduction of dislocations in these different heterostuctures. Strategies for further reduction of dislocation density in HgCdTe(211) that have been explored so far include: localized substrate thinning, *ex situ* thermal cycle annealing (TCA), and a combination of dry-etching of novel mesa structures and *ex situ* TCA.[1,2,3] Localized substrate thinning was shown to reduce dislocation density in some cases by up to 42%.[1] Dislocation pinning near the interface due to reduced image forces in the thinned substrates was suggested as the reason for the reduction in etch-pit-density (EPD).[1] Annealing has long been recognized as an effective post-processing technique that can reduce the density of defects in metals and alloys.[4,5] *Ex situ* TCA has recently been explored as a way to reduce the density of defects in HgCdTe films.[6] Early attempts were focused on establishing the optimum experimental parameters for maximum reduction of dislocation density. The key parameters in TCA processing are annealing

temperature and the number of cycles.[2,7] Figure 4.1 shows that for an equal number of cycles and the same temperature ramp, dislocations were immobile for annealing temperatures below 360°C, while increasing temperatures to higher than 500°C did not lead to further decrease in EPD. Similarly, fixing the annealing temperature at its upper limit, i.e. 500°C, did not reduce the dislocation density further after four annealing cycles, i.e. saturation limit.[7]

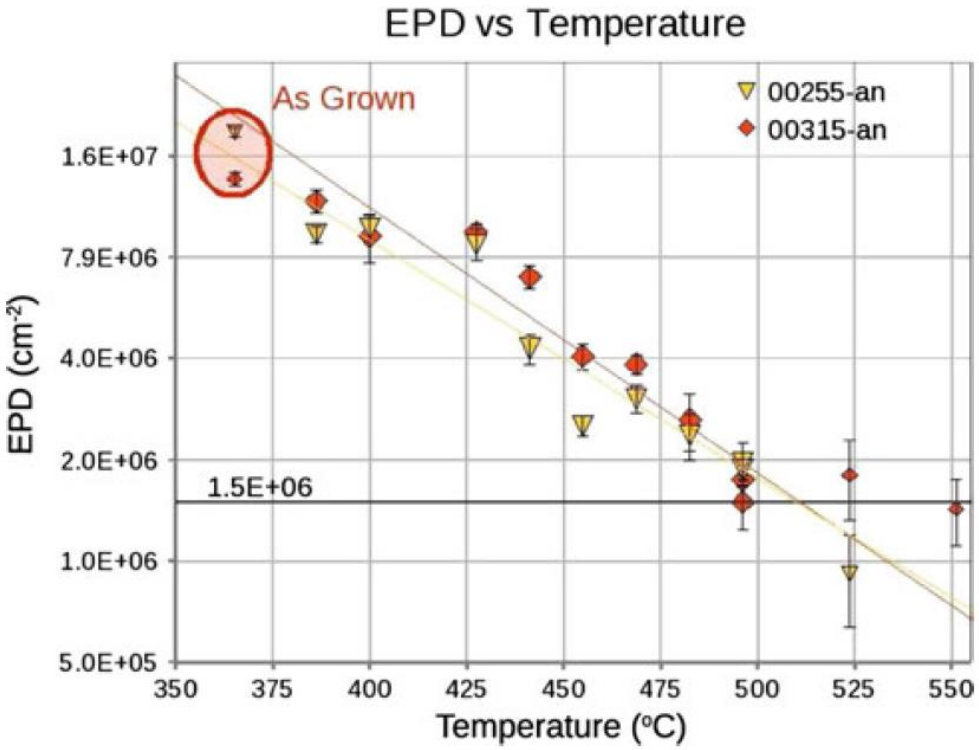

Figure 4. 1 Variation of etch-pit-density vs. temperature for four TCA processes in HgCdTe/CdTe/Si (211) films.[7]

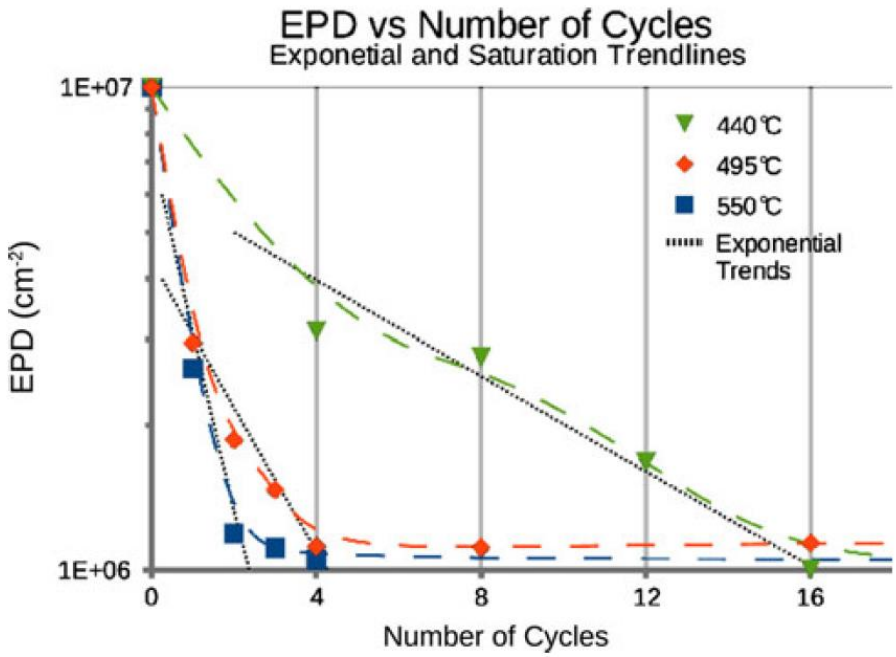

Figure 4. 2 Exponential decay in EPD vs. number of annealing cycles for variation of EPD vs. annealing temperatures of 440°C, 495°C, and 550°C.[7]

The model of Yamaguchi was extended to describe the underlying mechanism of dislocation reduction in TCA MCT samples.[2] Dislocation annihilation and dislocation coalescence with re-emission were shown to be primarily responsible. For an *n*-type HgCdTe(211), the activation energy for dislocation motion was calculated to be 0.93±0.1 eV.[2] Basically, TCA provides thermal energy that allows the dislocations to be activated and become mobile. These dislocations can then interact with each other through several different mechanisms such as slip on the same plane for dislocations with the same slip plane, cross-slip or glide for dislocation in close proximity and in parallel planes, interaction of two dislocations lying on non-parallel slip planes at their intersection, and movement to the edge of the layer or through a grain boundary to leave the crystal.[7] Figure 4.3 shows a schematic representation of dislocations inside HgCdTe layers and

their coalescence and annihilation.[7] It was also shown that the EPD saturation limit was independent of annealing temperature, but the number of annealing cycles required to reach that point was inversely proportional to the TCA temperature. For example, saturation in the dislocation density at temperatures of 441°C, 494°C, and 551°C occurred for 16, 8, and 2 cycles respectively.[2]

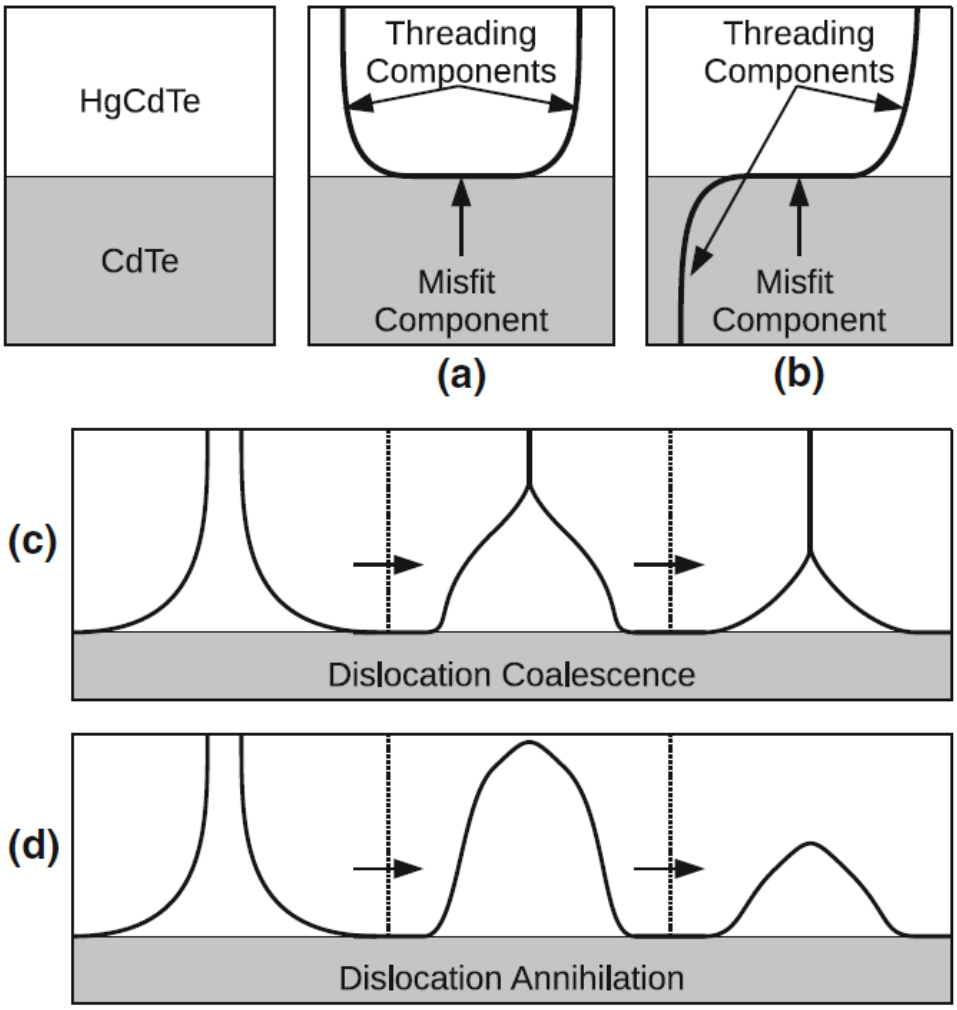

Figure 4. 3 Schematic illustration of: (a) threading dislocations generated from misfit dislocations, (b) threading dislocation emerging from a seeded misfit from CdTe layer, (c) coalescence of two dislocations into a single dislocation, and (d) dislocation annihilation and loop relaxation.[7]

The combination of plasma processing for fabrication of reticulated mesa bars with relatively flat side walls as stress-free regions for dislocations to glide together and TCA was used to reduce dislocation density by an order of magnitude compared with TCA samples alone.[8,9] It was also found that, among different reticulated shapes, rectangular bars with length>50μm and width> 20μm aligned along $[0\bar{1}1]$ directions were more effective in gettering defects.[10] Further studies involved the concept of image force on flat mesa surfaces, and it was shown that dislocation gettering by TCA mesa bars depended on mesa etch depth, mesa width and angle of tilt away from $[0\bar{1}1]$ direction.[10]

Evaluation of defect density in HgCdTe is of paramount importance for next generation of IR detectors. Among several different techniques for identification of defect density, such as high-resolution XRD and TEM, the approach of etching the material with a suitable etchant, which results in etch pits with 1:1 correspondence to dislocations, is easier and less expensive.[11] Basically, the enhanced etching rate of strained regions around the dislocations is expected to reveal the point of emergence of the dislocation at the top surface.[12,13] Plan-view phase-contrast Nomarski microscopy or scanning electron microscopy (SEM) can then be used to investigate the pits and estimate their density in the etched material. However, due to its better resolution, SEM is generally to be preferred since there have been reports that the Nomarski technique missed smaller etch pits.[12] Different etchants for delineation of defects in HgCdTe, such as Schaake and Benson etchants, have been developed and compared.[14] Different etch pit shapes were identified in as-grown and TCA samples, but the nature of the dislocations corresponding to each type of pit was not reported.

In this work, Focused-Ion-Beam (FIB) milling has been used for preparing site-specific cross-section specimens for etch pits of different shape in as-grown and TCA MCT samples. Conventional two-beam bright-field (BF) imaging was used for determination of Burgers vectors. These observations correlate the different types of etch pits with the dislocations present in as-grown MCT (211) films, and provide insight into the reduction and transformation of dislocations during annealing.

4.2. Experimental details

Samples of LWIR $Hg_{1-x}Cd_xTe$ (x~0.2) were grown on 7.6 cm (3") diameter Si (211) substrates by molecular beam epitaxy (MBE) in a modified Fisons VG 80 reactor. Details about Si surface preparation before growth, CdTe buffer layer deposition, flux of constituent elements (e.g., Hg) and compounds (CdTe), substrate temperature and growth rate can be found elsewhere.[15] The TCA sample examined in this study were subjected to 4 annealing cycles between 250°C and 494°C. The estimated error in sample temperature during each cycle was 7-10°C. Since threading dislocation reduction is based on dislocation movement, high temperature ramp rates were desirable, and a ramp up of approximately $50°C.min^{-1}$ was used. The ramp rate was determined mostly by the need to limit surface damage and/or Hg desorption. After maintaining the maximum temperature for 5 min, the furnace was allowed to cool to 250°C. This annealing cycle was repeated 4 times for each sample under investigation. Cooling from the maximum temperature occurred in 12 min. Both as-grown and TCA samples were then defect-decorated using the Benson etchant.[16] This procedure reveals etch pits that correspond to threading dislocations that are present at the growth surface.

FIB milling with an FEI Nova200 dual-beam system was used to prepare cross-section (XTEM) specimens from sample regions containing the pits. For protection against Ga+ damage, the areas of interest were coated with a thin layer of carbon, followed by 200-300nm of Pt deposition in electron mode and deposition of 2μm of Pt in Ga^+ mode. The samples were subsequently thinned to electron transparency at 0.1nA with 30keV Ga^+ ions. Most samples were prepared for imaging in $<0\bar{1}1>$ projection since this orientation provided more diffraction spots for two-beam imaging. Some samples were also prepared for viewing along $<\bar{1}11>$.

A Philips FEI CM-200 operated at 200keV microscope was used for these studies. The samples were tilted to various orientations for two-beam imaging namely: $\boldsymbol{g_1}=\pm<111>$, $\boldsymbol{g_2}=\pm<\bar{1}11>$, $\boldsymbol{g_3}=\pm<022>$, $\boldsymbol{g_4}=\pm<400>$ and $\boldsymbol{g_5}=\pm<311>$ in $<0\,\bar{1}1>$ zone, $\boldsymbol{g_1}=\pm<02\bar{2}>$, $\boldsymbol{g_2}=\pm<\bar{2}\bar{2}0>$, $\boldsymbol{g_3}=\pm<\bar{2}0\bar{2}>$, $\boldsymbol{g_4}=\pm<422>$ and $\boldsymbol{g_5}=\pm<2\bar{2}4>$ in $<\bar{1}11>$ zone, and $\boldsymbol{g_1}=\pm<040>$, $\boldsymbol{g_2}=\pm<\bar{2}20>$, $\boldsymbol{g_3}=\pm<220>$, and $\boldsymbol{g_4}=\pm<400>$ in <001> zone. This analysis was necessary for the determination of Burgers vectors associated with dislocation segments appearing in the XTEM images. During these studies, it was important not to confuse FIB-induced curtaining as dislocation segments. Curtains are artefacts of the FIB sample preparation process that appear as vertical strips roughly perpendicular to the top surface of the foil. The distinction between these features is obvious since the curtains appear clearly in both SEM/TEM micrographs whereas dislocation segments go in and out of contrast upon specimen tilting in the TEM.

4.3. Results and discussion

4.3.1. As-grown HgCdTe(211)

Figure 4.4 shows SEM images of an as-grown MCT sample after etching, which is decorated with surface pits. The primary etch-pit morphologies can be designated as triangular, skew or wedge-shape, and fish-eye. Scanning across the as-grown sample in a total area of ~1000 μm^2 (10 SEM micrographs) showed that the distribution of the pits in the as-grown sample was roughly 43% triangular, 29% skew, 26% fish-eye, and 2% others. The total EPD was ~1.1×10^8 cm^{-2} and the corresponding etch-pit density for each pit shape was triangular pits ~4.8×10^7 cm^{-2}, skew pits ~3.3×10^7 cm^{-2}, fish-eye ~2.9×10^7 cm^{-2} and others ~2.4×10^6 cm^{-2}. These results are tabulated in table 4.1.

Shape	**Triangular**	**Skew**	**Fish-eye**	**Other**
Fraction	43%	29%	26%	2%
EPD (cm^{-2})	4.80E+07	3.30E+07	2.90E+07	2.40E+06
Total EPD (cm^{-2})	1.10E+08			

Table 4. 1 Morphology of etch pits and corresponding EPD distribution in as-grown HgCdTe film.

Interestingly, the fish-eye shapes always lined up along one $<\bar{1}11>$ direction. Moreover, no two fish-eye pits were observed in head-to-head configuration while skew pits lined up in different directions, sometimes close to $<2\bar{3}\bar{1}>$ and $<\bar{2}\bar{1}3>$ directions. Although the triangular pits appeared with a range of different sizes, they always lined up along $<\bar{1}11>$. Figures 4.5 (a-j) show $<0\,\bar{1}1>$ BF TEM micrographs of the region highlighted in Fig. 4.4 for $\mathbf{g_1{:}g_5}$ two-beam conditions along skew, triangular and other morphology (bone-shape) pits. Unfortunately, the skew pit was not visible in the final XTEM sample after thinning. The dislocation corresponding to the triangular pit marked

"B" appears beneath the pit at a right angle with respect to the MCT surface, while the dislocation segment "A" could be correlated with one of the skew pits in the vicinity of the triangular pit. Table 4.4 shows the results of dislocation analysis for each segment, where "V" and "I" notations represent visible and invisible for the specific dislocation segments. Based on **g.b** analysis, the corresponding dislocations for triangular pits are identified as sessile Frank partial dislocations with Burgers vector $\mathbf{b}=\frac{1}{3}[111]$ type. The other segments are Shockley partial dislocations with Burgers vector of $\mathbf{b}=\frac{1}{6}[112]$ type.

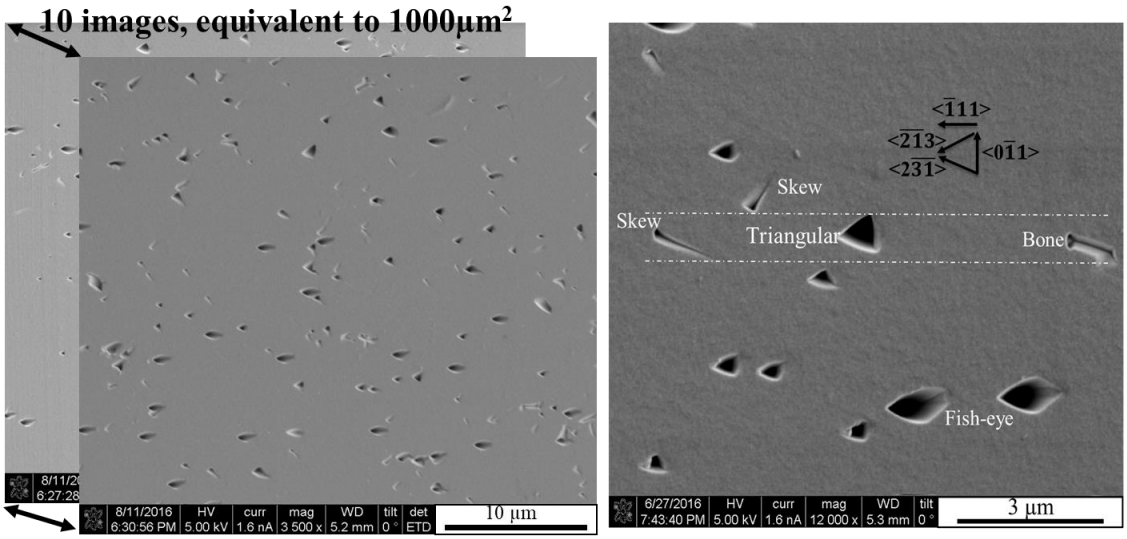

Figure 4. 4 SEM micrographs of as-grown MCT sample. Triangular, skewed and fish-eye shapes are marked.

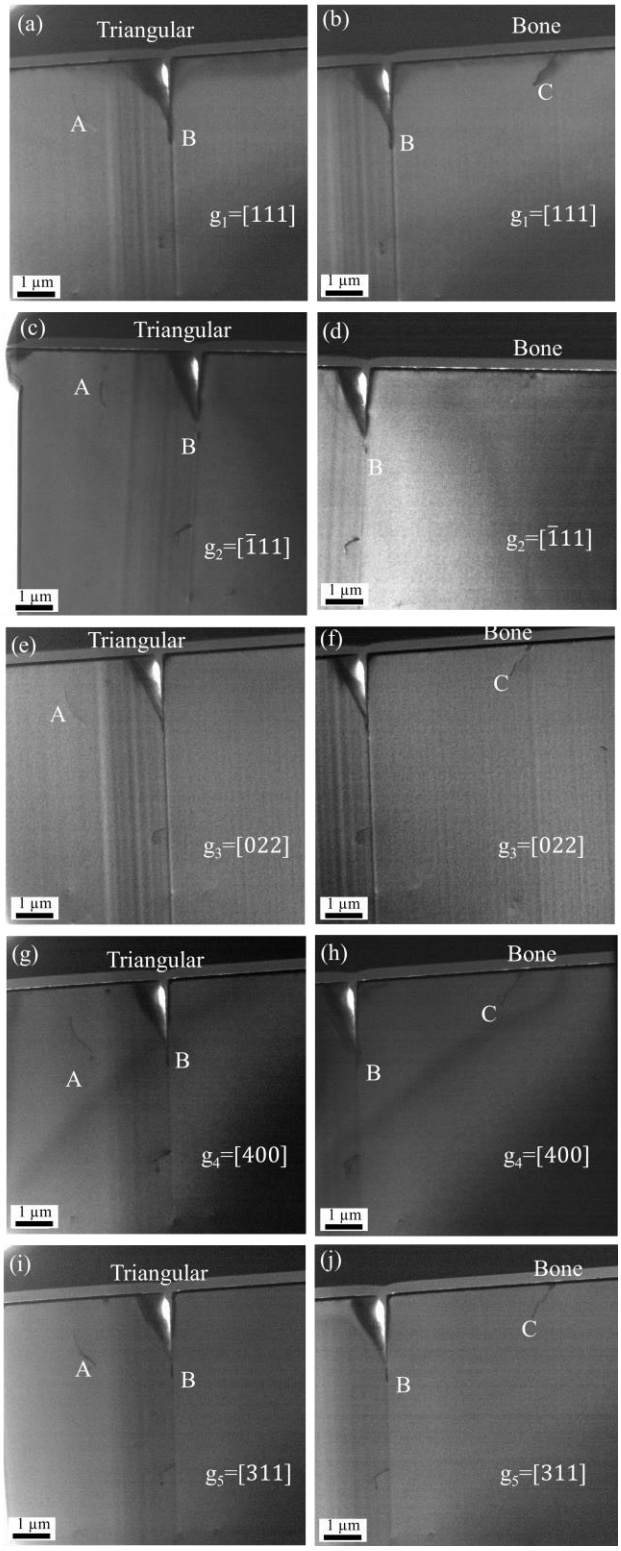

Figure 4. 5 XTEM micrographs of triangular and bone-shape pits in as-grown MCT sample at $\mathbf{g_1}$:$\mathbf{g_5}$. Burgers vector analysis summarized in Table 4.2.

g	**A**	**B**	**C**
$\mathbf{g_1}$	I	V	V
$\mathbf{g_2}$	V	V	I
$\mathbf{g_3}$	V	I	V
$\mathbf{g_4}$	V	V	V
$\mathbf{g_5}$	V	V	V
b (**predicted)**	$\frac{1}{6}[2\bar{1}\bar{1}]$ $\frac{1}{6}[\bar{1}2\bar{1}]$	$\frac{1}{3}[11\bar{1}]$ $\frac{1}{3}[1\bar{1}1]$	$\frac{1}{6}[\bar{2}\bar{1}\bar{1}]$ $\frac{1}{6}[12\bar{1}]$
Fault Plane	(111)	$(1\bar{1}1)/(\bar{1}11)$	$(\bar{1}11)$

Table 4. 2 **g.b** analysis and Burgers vector identification for dislocation segments appearing in Fig. 4.5.

Figure 4.6 (a) shows an SEM micrograph corresponding to a series of fish-eye pits, marked 1-6, as selected for FIB sample preparation. Two-beam BF imaging for $\boldsymbol{g_1}$:$\boldsymbol{g_5}$ conditions along these pits is shown in Figs. 4.6(b-f). The dislocation segments marked A, B and C appear at the sharp tip of the fish-eye pit with an angle of ~30° with respect to the flat surface. Based on the **g.b** analysis results shown in Table 4.2, these pits represent perfect dislocations with Burgers vector of $\mathbf{b}=\frac{1}{2}[011]$ type.

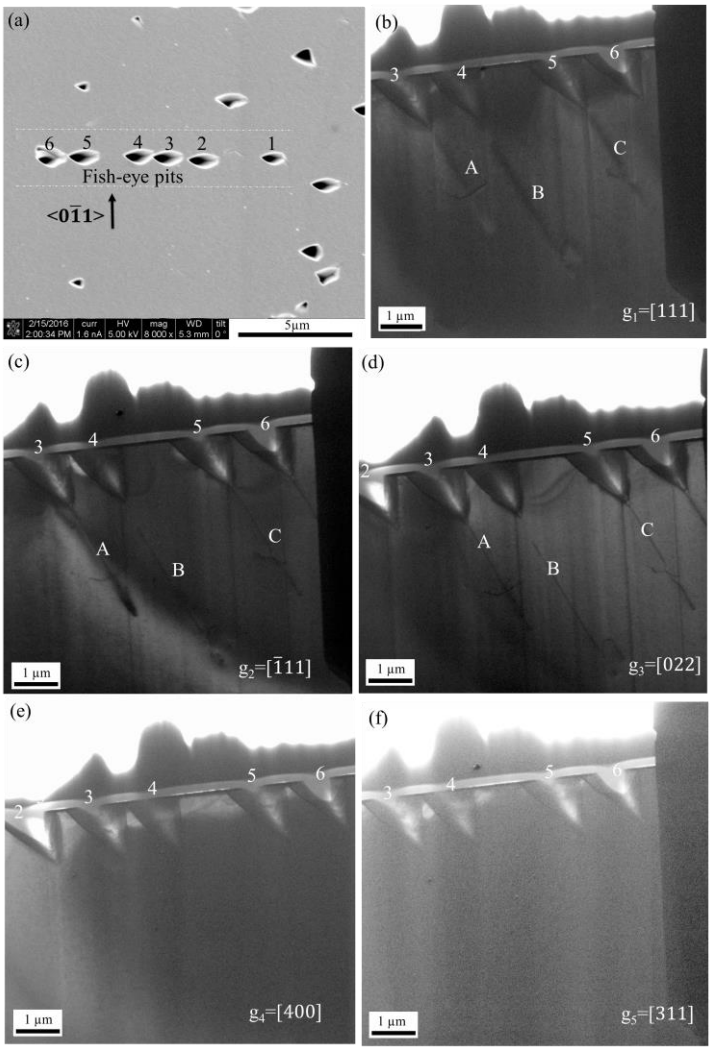

Figure 4. 6 (a) SEM micrograph of as-grown MCT sample: fish-eye pits were targeted for FIB lift out, (b-f) XTEM micrographs of fish-eye shape pits in as-grown MCT sample at $\mathbf{g_1}$:$\mathbf{g_5}$.

g	**A**	**B**	**C**
$\mathbf{g_1}$	V	V	V
$\mathbf{g_2}$	V	V	V
$\mathbf{g_3}$	V	V	V
$\mathbf{g_4}$	I	I	I
$\mathbf{g_5}$	I	I	I
b (**predicted)**	$\frac{1}{2}[0\bar{1}1]$	$\frac{1}{2}[0\bar{1}1]$	$\frac{1}{2}[0\bar{1}1]$
Fault Plane	$(111)/(\bar{1}11)$	$(111)/(\bar{1}11)$	$(111)/(\bar{1}11)$

Table 4. 3 **g.b** analysis and Burgers vector identification for dislocation segments appearing in Fig. 4.6.

For better understanding of the nature of dislocations in triangular and fish-eye shape pits, a FIB sample was prepared for observation along the orthogonal $[\bar{1}11]$ direction. Figure 4.7 shows an SEM micrograph for a series of fish-eye and triangular pits, marked 1-7, which were selected for FIB sample preparation. Two-beam BF imaging at $\boldsymbol{g_1}$:$\boldsymbol{g_5}$ along the pits labeled #3 to #7 are shown in Figs. 4.8 (a-f). These results, summarized in Table 4.4, confirm that the triangular pits most likely correspond to Frank partial dislocations in the as-grown MCT, since two-third of the dislocation segments have $\mathbf{b}=\frac{1}{3}[111]$ type. XTEM images show that individual singular fish-eye shape pits do not have segments visible in the $[\bar{1}11]$ zone in this FIB-prepared sample. However, when they are merged with other pits, (compare the appearance of pit#5 with pit#3 or #1 in Fig. 4.4), they represent a long thread marked as "D" all the way from the lower CdTe interface to upper MCT regions, (see Fig 4.8(f).).

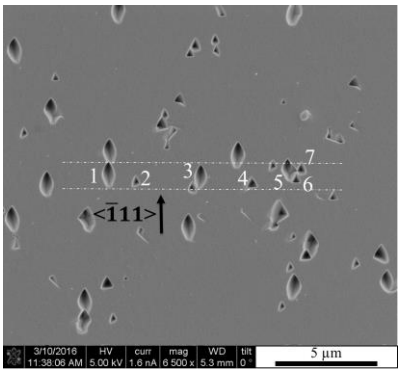

Figure 4. 7 SEM micrograph of as-grown MCT sample: fish-eye and triangular pits were targeted for FIB lift-out in orthogonal direction.

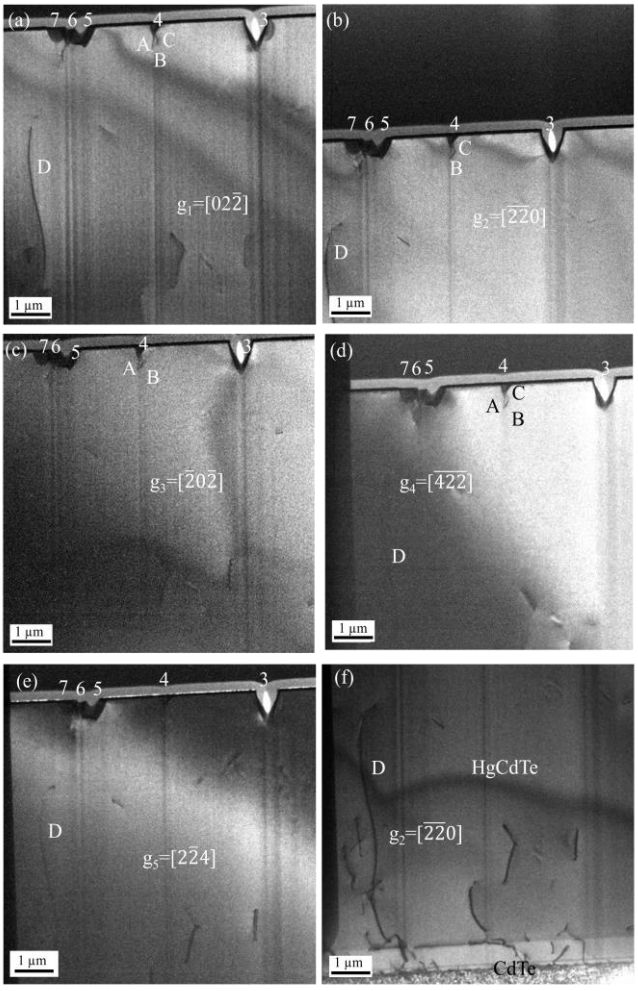

Figure 4. 8 XTEM micrographs of fish-eye shape and triangular pits in orthogonal zone at $\mathbf{g_1}$:$\mathbf{g_5}$.

g	**A**	**B**	**C**	**D**
$\mathbf{g_1}$	V	V	V	V
$\mathbf{g_2}$	I	V	V	V
$\mathbf{g_3}$	V	V	I	I
$\mathbf{g_4}$	V	V	V	V
$\mathbf{g_5}$	I	I	I	V
b (predicted)	$\frac{1}{3}[\bar{1}11]$	$\frac{1}{2}[110]$ $\frac{1}{6}[110]$	$\frac{1}{3}[\bar{1}11]$	$\frac{1}{2}[10\bar{1}]$ $\frac{1}{6}[10\bar{1}]$
Fault Plane	$(\bar{1}11)$	(111) $(\bar{1}11)$	$(\bar{1}11)$	(111) $(\bar{1}11)$

Table 4. 4 **g.b** analysis and Burgers vector prediction for fish-eye shape and triangular pits in orthogonal <$\bar{1}$11> direction in as-grown sample (See Fig. 4.8).

Identifying dislocations corresponding to skewed pits was very difficult in practice as they always lined up at an angle with respect to the <0$\bar{1}$1> direction. Figures 4.9 (a-b) show an SEM micrograph for a set of skew pits, and an XTEM image of a couple of pits that were present in the final thinned sample. Dislocation analysis summarized in Table 4.5 showed that the skew pits had a complex structure consisting of perfect dislocations and Shockley partials. These dislocation segments clearly did not start right beneath the pits when the sample was prepared on the <0$\bar{1}$1> zone axis. Therefore, the FIB was used to make a lift-out sample of a skewed pit parallel to <2$\bar{3}\bar{1}$>, as shown in Figs. 4.10 (a-f). At the new orientation after rotation, the dislocation segment marked "A" appears right beneath the sharp tip of the pit, Fig 4.10 (c-f). Since the <001> zone does not provide many diffraction spots, determination of the Burgers vector relied more on vector algebra

prediction. Therefore, dislocation “A” and “B” might both be perfect dislocations with $\mathbf{b}=\frac{1}{2}[011]$ and $\mathbf{b}=\frac{1}{2}[101]$, respectively (see Table 4.6).

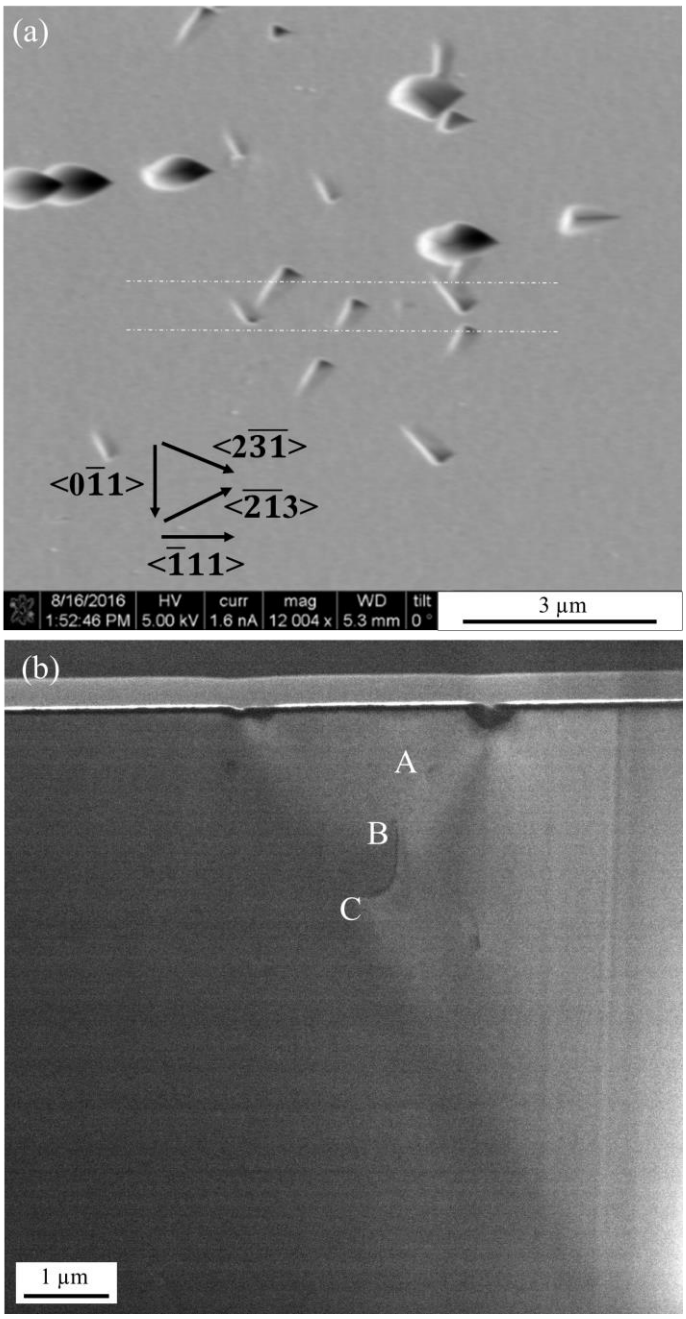

Figure 4. 9 (a) SEM micrograph of skewed pits targeted for FIB lift-out, and (b) XTEM micrograph.

g	**A**	**B**	**C**
$\mathbf{g_1}$	V	I	V
$\mathbf{g_2}$	V	V	V
$\mathbf{g_3}$	I	V	V
$\mathbf{g_4}$	V	V	V
$\mathbf{g_5}$	I	I	I
b (predicted)	$\frac{1}{2}[0\bar{1}1]$	$\frac{1}{2}[0\bar{1}1]$	$\frac{1}{6}[\bar{1}21]$
Fault Plane	(111) $(\bar{1}11)$	(111) $(\bar{1}11)$	$(11\bar{1})$

Table 4. 5 **g.b** analysis and Burgers vector prediction for dislocations associated with skew etch-pits in as-grown sample (See fig. 4.9(b)).

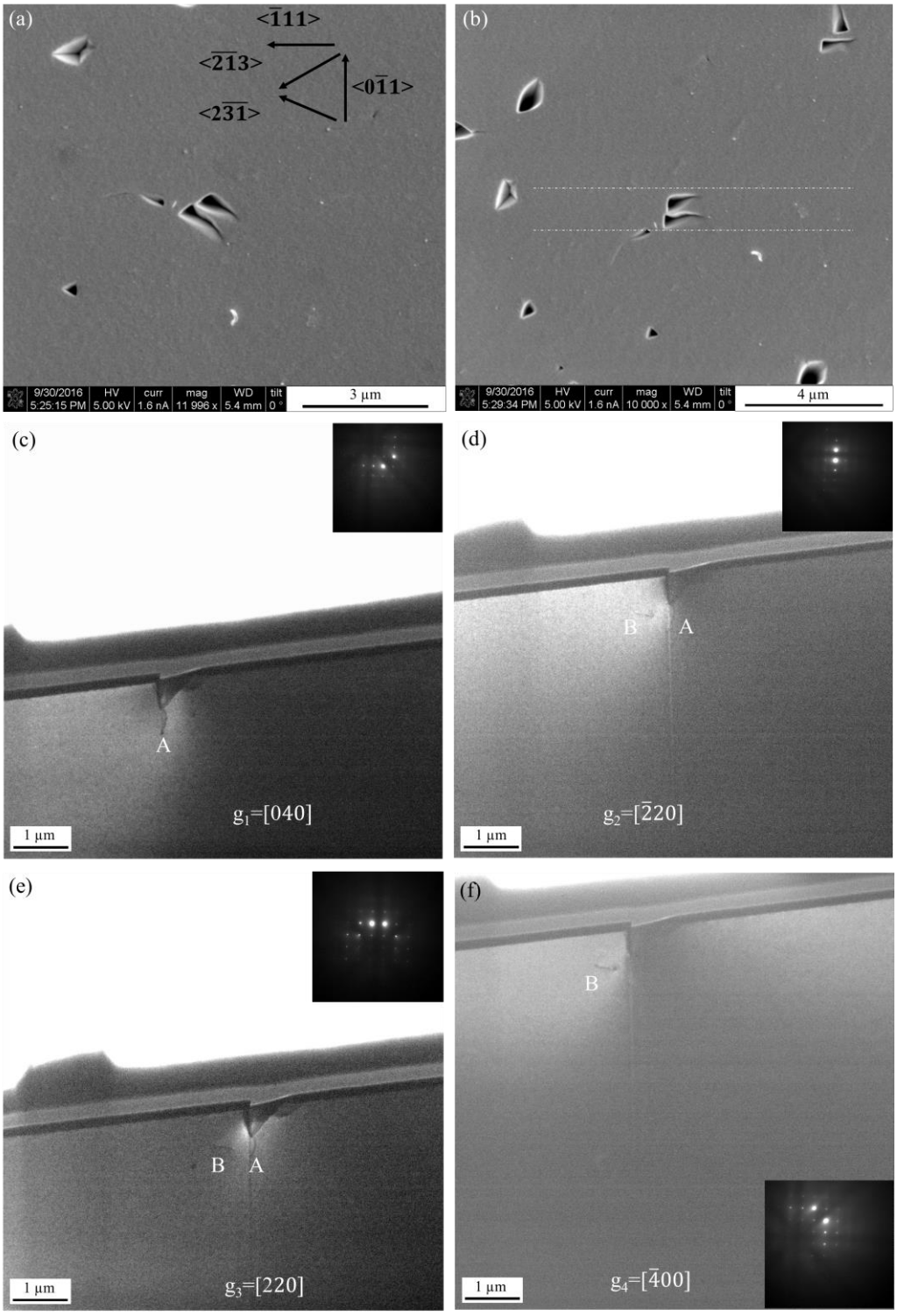

Figure 4. 10 (a&b) SEM micrographs of skewed pits not-rotated and rotated, (c-f) XTEM micrographs of rotated skewed pits at different $\mathbf{g_1}$:$\mathbf{g_4}$.

g	**A**	**B**
g_1	V	I
g_2	V	V
g_3	V	V
g_4	I	V
b (predicted)	$\frac{1}{2}[011] / \frac{1}{2}[0\bar{1}1]$	$\frac{1}{2}[101] / \frac{1}{2}[10\bar{1}]$
Fault Plane	$(1\bar{1}1)/(11\bar{1})$ $(111)/(\bar{1}11)$	$(1\bar{1}\bar{1})/(11\bar{1})$ $(111)/(1\bar{1}1)$

Table 4. 6 **g.b** analysis and Burgers vector prediction for dislocations related to rotated skew pits in as-grown sample (See fig. 4.10).

4.3.2. Thermal-Cycle-Annealing

Figures 4.11 (a,b) compare SEM micrographs of as-grown and TCA samples side by side. It is clear that a major reduction, (~72%), in etch pit densities has occurred because of the TCA treatment. Comparison of the shape and density of the pits after TCA showed that one of the three primary pit morphologies present in the as-grown MCT, i.e. fish-eye shapes, was absent in the annealed sample. This finding establishes that fish-eye pits must correspond to mobile dislocations that react with other dislocations during TCA. The TCA sample was imaged over a total area of ~1000 μm^2 to determine the pit distribution, which was 51% triangular, 29% skew, 20% others (i.e. rod-shape, polygonal, and irregular shapes). The total EPD was ~3.1×10^7 cm^{-2} and the corresponding EPD for each type of pit was triangular pits ~1.6×10^7 cm^{-2}, skew pits ~9.2×10^6 cm^{-2} and others ~6.2×10^6 cm^{-2}. These results are tabulated in table 4.7. It is interesting that many of triangular and skew pits do not have the exact same morphology as their counterparts in the as-grown sample. For example, it was more likely for triangular pits in the TCA sample to deviate from the equilateral shape with sides at an angle with respect to $<\bar{1}11>$, and for the skew pits to be narrower, i.e., more skewed.

Shape	**Triangular**	**Skew**	**Fish-eye**	**Other**
Fraction	51%	29%	Absent	20%
EPD (cm^{-2})	1.60E+07	9.20E+06	0.00E+00	6.20E+06
Total EPD (cm^{-2})	3.10E+07			

Table 4. 7 Morphology of etch pits and corresponding EPD distribution in TCA HgCdTe film.

Figures 4.12 (b-f) show XTEM micrographs of the section highlighted in the SEM micrograph, Fig 4.12 (a), for $\mathbf{g_1}$:$\mathbf{g_5}$ values along triangular pits parallel and antiparallel to $<\bar{1}11>$, and disk-shape pits. The **g**.**b** analysis summarized in Table 4.8 reveals that the majority of segments are perfect dislocations with $\frac{1}{2}[0\bar{1}1]$ Burgers vector, and the remainder are Shockley partials. The dislocation types have clearly changed after TCA. Segments in the TCA sample appeared more fragmented in the bulk of the film rather than being close to the surface.

Analysis of an area of "other" type of pit morphology was done to create a more complete picture of the nature of dislocations after TCA. These pits often lined up along $<0\bar{1}1>$ rather than $<\bar{1}11>$. Therefore, XTEM analysis was done along $<\bar{1}11>$ projection. Figure 4.13(a) is an SEM micrograph showing a series of these "other" pits lined up along $<0\bar{1}1>$. The odd morphology of these pits is attributed to the transformation and reaction of dislocations during TCA. Figures 4.13(b-f) show dislocations associated with these pits. Although determination of some segments was entirely (e.g. "C") or partially (e.g. "A") impossible, the results in Table 4.9 show that some dislocations corresponding to "other" morphology pits are different from the ones predicted in $<0\bar{1}1>$ projection. A detailed study of the mechanism responsible for defect reduction after TCA, and the dislocation-dislocation interactions and reactions should be the subject of future studies.

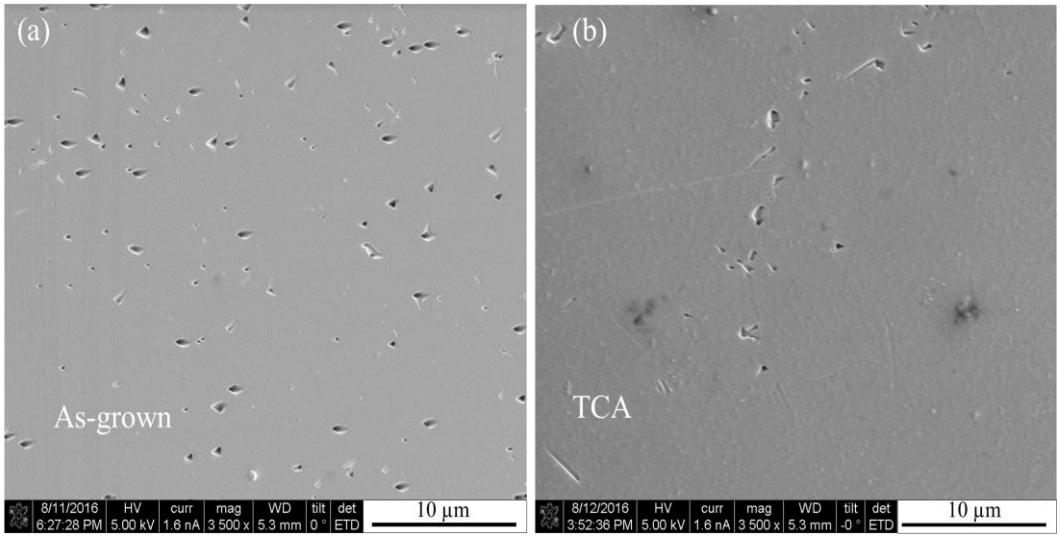

Figure 4. 11 SEM micrographs comparing the MCT surface morphology after etching: (a) as-grown sample, and (b) TCA sample.

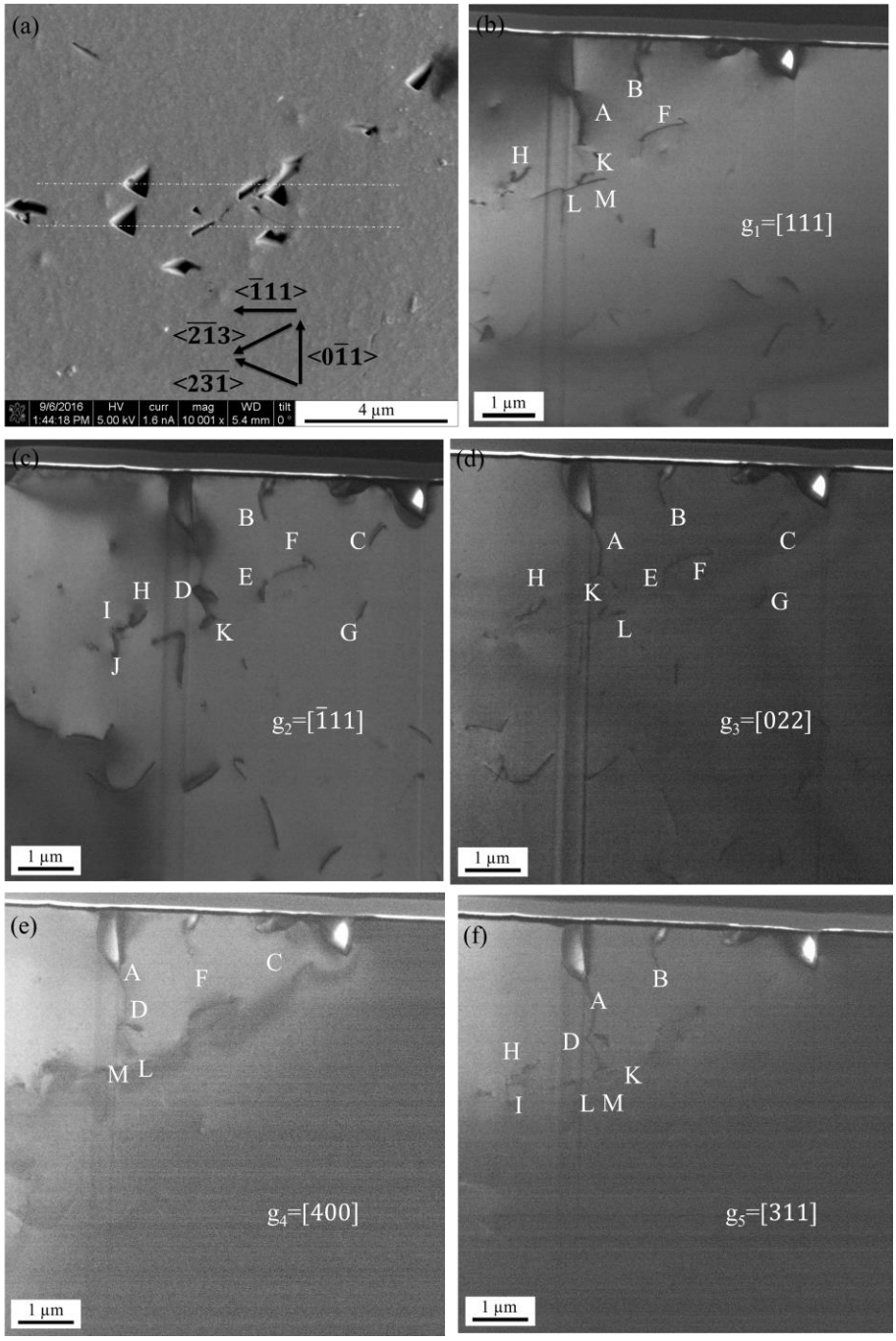

Figure 4. 12 (a) SEM micrograph of TCA sample: area with populated pits was chosen for FIB lift-out. (b-f) XTEM micrographs of TCA sample at different $\mathbf{g_1}$:$\mathbf{g_5}$.

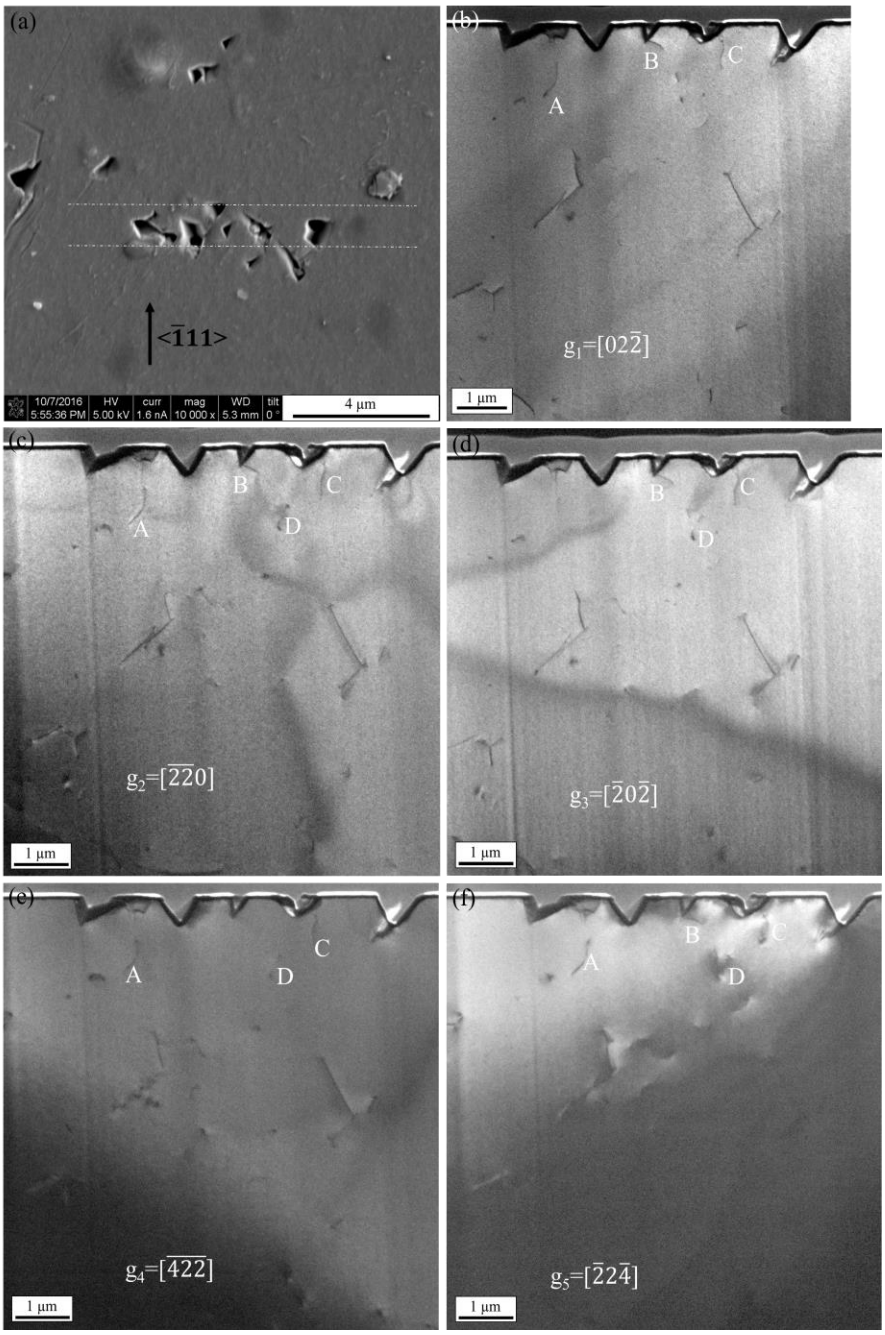

Figure 4. 13 (a) SEM micrograph of TCA sample: region with series of pits with "other" morphologies was selected for FIB lift-out along $< \bar{1}11 >$ projection. (b-f) XTEM micrographs of TCA sample at $\mathbf{g_1}$:$\mathbf{g_5}$.

g	A	B	C	D	E	F	G	H	I	J	K	L	M
g_1	V	V	I	I	I	V	I	V	I	I	V	V	V
g_2	I	V	V	V	V	V	V	V	V	V	V	I	I
g_3	V	V	V	I	V	V	V	V	I	I	V	V	I
g_4	V	I	V	V	I	V	I	I	I	I	I	V	V
g_5	V	V	I	V	I	I	I	V	V	I	V	V	V
b predicted	$\frac{1}{6}[211]$ $\frac{1}{6}[12\bar{1}]$	$\frac{1}{6}[011]$	$\frac{1}{2}[0\bar{1}1]$	$\frac{1}{2}[0\bar{1}1]$	$\frac{1}{2}[0\bar{1}1]$	$\frac{1}{6}[\bar{1}21]$	$\frac{1}{2}[0\bar{1}1]$	$\frac{1}{6}[011]$	$\frac{1}{2}[0\bar{1}1]$	$\frac{1}{2}[0\bar{1}1]$	$\frac{1}{6}[011]$	$\frac{1}{6}[211]$ $\frac{1}{6}[12\bar{1}]$	$\frac{1}{2}[0\bar{1}1]$
Fault Plane	$(\bar{1}11)$	$(1\bar{1}1)$ $(11\bar{1})$	(111) $(\bar{1}11)$	(111) $(\bar{1}11)$	(111) $(\bar{1}11)$	$(11\bar{1})$	(111) $(\bar{1}11)$	$(1\bar{1}1)$ $(11\bar{1})$	(111) $(\bar{1}11)$	(111) $(\bar{1}11)$	$(1\bar{1}1)$ $(11\bar{1})$	$(\bar{1}11)$	(111) $(\bar{1}11)$

Table 4. 8 **g.b** analysis and Burgers vector prediction for dislocation segments in TCA sample (See fig. 4.8).

g	A	B	C	D
g_1	V	V	V	I
g_2	V	V	V	V
g_3	I	V	V	V
g_4	V	I	V	V
g_5	V	V	V	V
b (predicted)	$\frac{1}{3}[11\bar{1}]$ $\frac{1}{6}[12\bar{1}]$	$\frac{1}{2}[01\bar{1}]$	Undetermined	$\frac{1}{6}[21\bar{1}]$ $\frac{1}{6}[2\bar{1}1]$
Fault Plane	$(11\bar{1})$ $(\bar{1}11)$	(111) $(\bar{1}11)$	Undetermined	$(1\bar{1}1)$ $(11\bar{1})$

Table 4. 9 **g.b** analysis and Burgers vector prediction for TCA sample in orthogonal projection (See fig. 4.9).

4.4. Large Pits

Additional very large pits with similar density were observed in both as-grown and TCA samples, as shown in Figs. 4.14 (a,b). The observed density of these features in as-grown and TCA samples was 13 pits in 0.62 mm^2 and 12 pits in 0.62 mm^2, respectively, roughly corresponding to ~2×10^3 cm^{-2}. Higher magnification SEM images for the as-grown MCT sample shown in Figs. 4.14 (c), 4.16 (a) and 4.18 (a,d) indicate that these features are large deep pits that often penetrate all the way down to the CdTe buffer layer, with a dark contrast feature at the bottom with decorated walls on both sides with triangular pits. For the TCA MCT sample, these features appear as a central pit on a rough surface that is decorated with concentric circles of irregular pits.

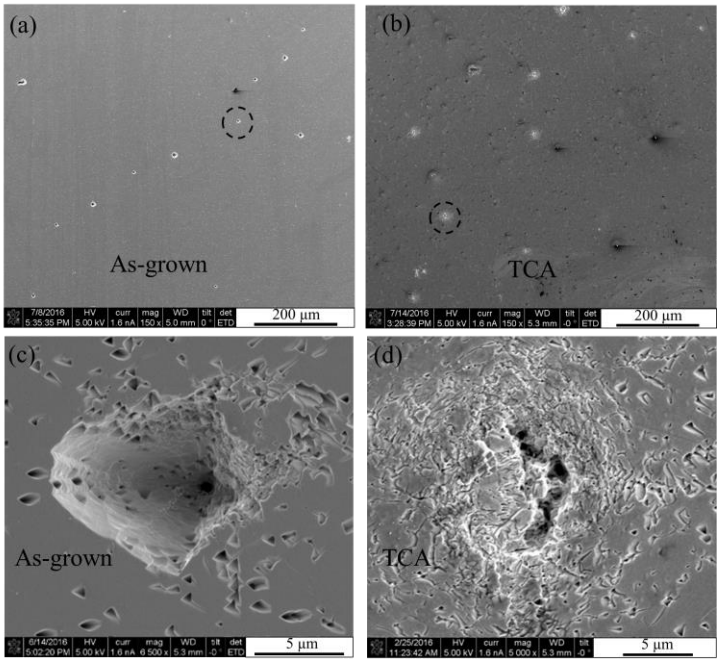

Figure 4. 14 (a) & (b) Low-magnification SEM micrographs of as-grown and TCA samples, respectively. A typical large pit is marked with a circle in each sample. (c) & (d) higher-magnification SEM micrographs of large pits in as-grown and TCA samples, respectively.

Figures 4.15 (b,e) show XTEM micrographs of two of these features observed in <0$\bar{1}$1> and <$\bar{1}$11> projections in the TCA sample. In both cases, long dislocation threads are observed beneath the large pit that extend all the way from the CdTe interface to upper HgCdTe regions. In some case, Figs. 4.15 (d), it appears that there are some discontinuities inside the MCT region close to the CdTe interface.

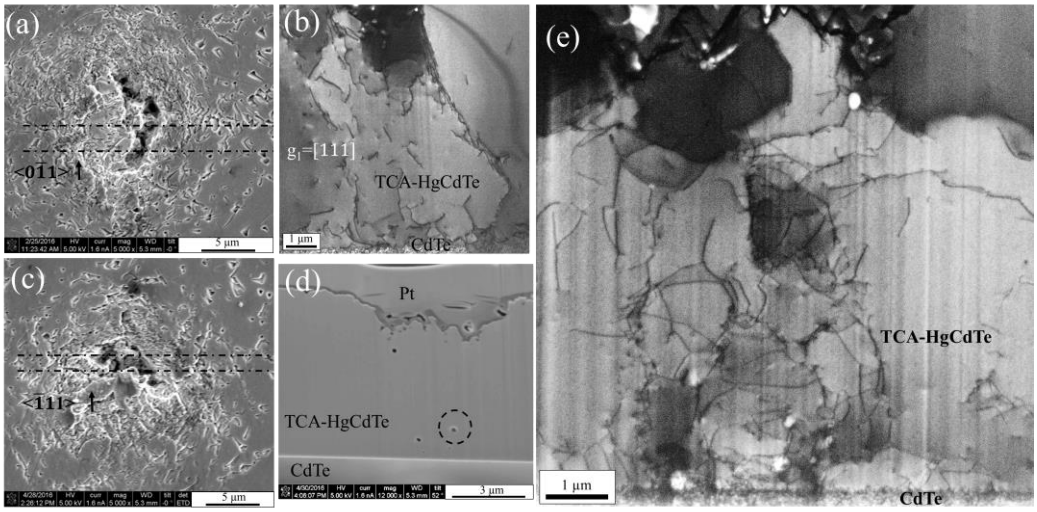

Figure 4. 15 (a) Low-magnification SEM micrographs of targeted large pit in TCA sample, (b) XTEM micrograph of the large pit in micrograph (a), (c) Low-magnification SEM micrograph of another targeted large pit in TCA sample oriented for orthogonal imaging along <$\bar{1}$11>, (d) SEM micrograph of FIB lamella prepared along <$\bar{1}$11> zone; one discontinuity is marked with a circle, and (e) XTEM micrograph of large pit prepared in orthogonal direction.

Similar analysis of as-grown MCT shows that CdTe beneath these large pits is dented, defective and not continuous at some places. However, since these large pits always penetrate all the way down, the likelihood of etchant diffusion and reaction with CdTe through the large hole weakens the hypothesis for correlation of these pits with defective CdTe regions. Figure 4.16 (a-c) shows SEM micrographs of one of these deep pits. A defective area in CdTe is observable before and after thinning the lamella. TEM micrographs of the sample shown in Fig. 4.16(c) shows that CdTe is completely detached from MCT, Fig. 4.17. Observation of pits with shorter depth, Figs. 4.18 (a,d), upon thinning with FIB also shows that micro-canals in some areas connect the bottom of the pits with the CdTe surface, and it is possible that these transfer corrosive liquid etchants to react with CdTe leaving dents and discontinuity behind in the CdTe, as shown in Figs. 4.18 (b,c,e,f). However, these discontinuities exist at some distance away from the bottom of the pit. Figure 4.19 shows a schematic of the models proposed for formation of these large pits.

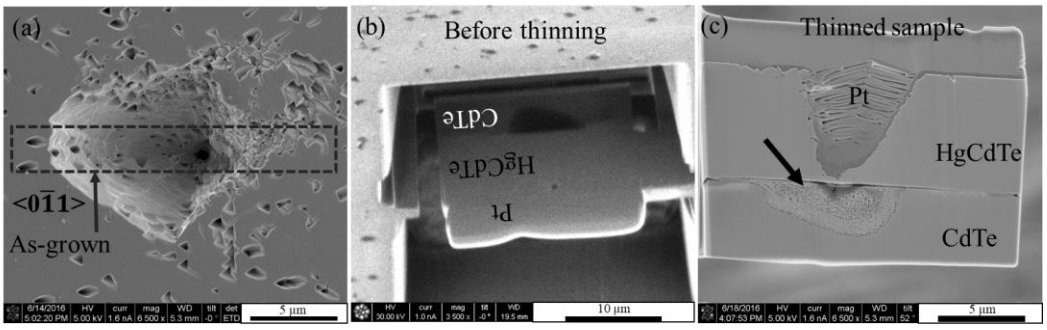

Figure 4. 16 (a) Low-magnification SEM micrographs of targeted large deep pit in as-grown sample, (b) Undercut section, CdTe has a large region with dark contrast, (c) thinned lamella with defective area marked with an arrow.

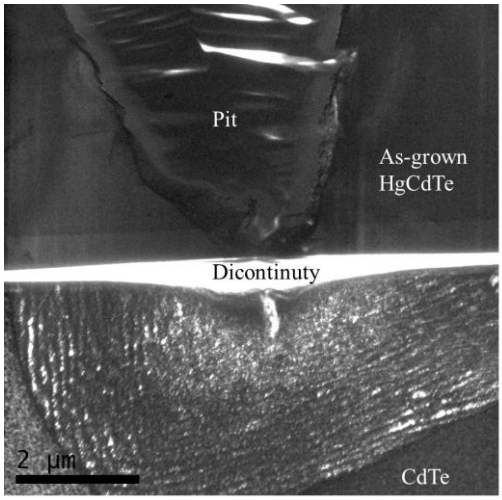

Figure 4. 17 TEM micrograph of the lamella from Fig.4.16.

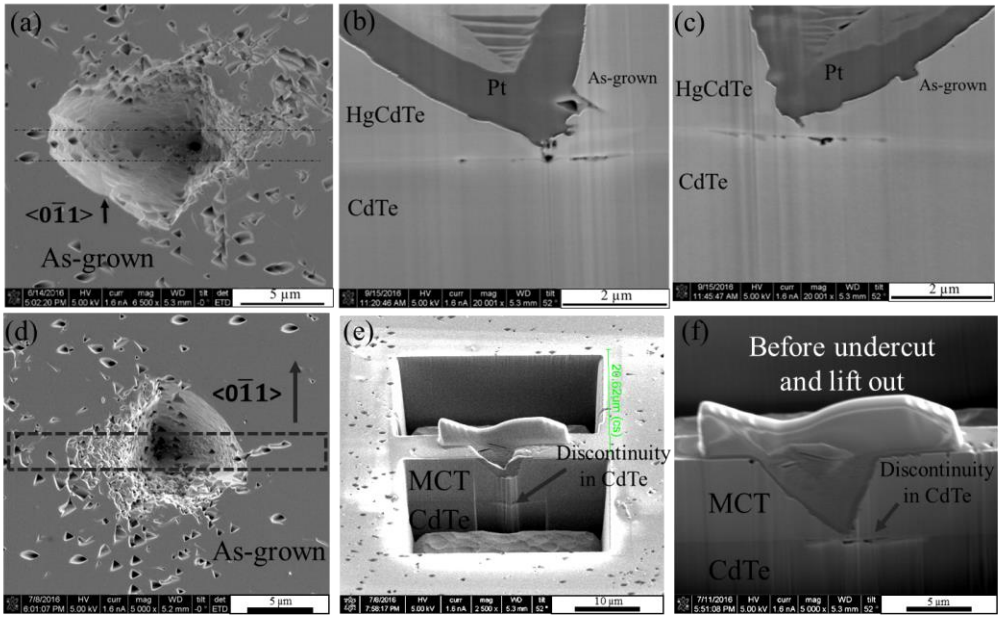

Figure 4. 18 (a) Low-magnification SEM micrograph of targeted large pit as-grown sample, (b,c) front- and back-side SEM micrographs of the targeted area in Fig. 4.18(a), (d) Low-magnification SEM micrograph of another large pit, (e) SEM micrograph at the beginning of trenching. Discontinuity in CdTe is clearly observed at the beginning of the trenching, and (f) SEM micrograph showing the bottom of the pit touching the CdTe interface.

Overall, the similar density of these large pits in as-grown and TCA samples, supports the idea that they represent a specific defect type. Unfortunately, the very fast reactivity of these areas in as-grown sample during chemical etching does not leave enough area remaining for detailed XTEM analysis. The different morphology of these pits observed in the TCA sample could be due to the fact that these defects partly reconstruct during the TCA process.

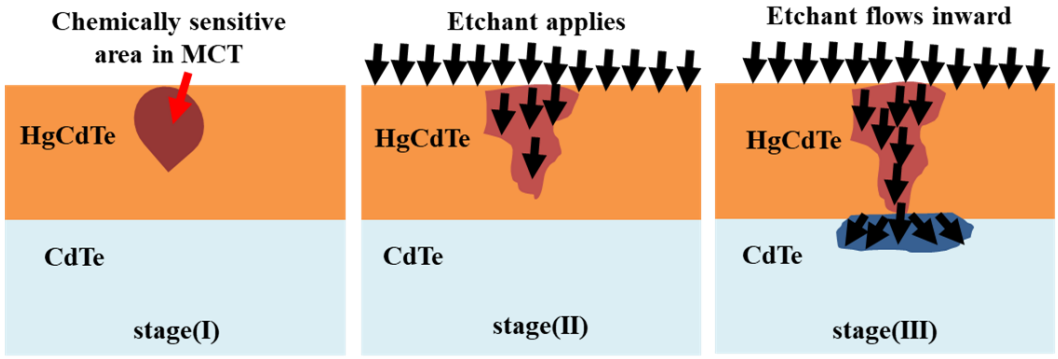

Figure 4. 19 Schematic of the proposed model for formation of large pits in as-grown material.

4.5 Conclusions

In summary, a detailed dislocation analysis was performed on as-grown and TCA HgCdTe/CdTe/Si(211) heterostructures to determine dislocation correspondence with etch pit. FIB lift-out in combination with SEM images was used to target different etch-pit morphologies in both as-grown and TCA samples.

Triangular pits in the as-grown sample were associated with Frank partial dislocations, while fish-eye pits were associated with perfect dislocations with $\frac{1}{2}[0\bar{1}1]$Burgers vector. Skew pits were determined to have a more complex nature than fish-eye and triangular pits. It was shown that TCA reduced EPD by 72%. Although TCA processing eliminated the fish-eye pits, $\frac{1}{2}[0\bar{1}1]$ dislocations reappeared in shorter segments in TCA sample. Large pits were observed in both as-grown and TCA samples. The nature of defects associated with these pits is unknown.

Overall, these results represent useful information about the nature of defects in as-grown and TCA HgCdTe/CdTe/Si heterostructures and should help in the development of the next generation of HgCdTe-based IR detectors.

References

[1]R. N. Jacobs, P. J. Smith, J. K. Markunas, J. D. Benson, and J. Pellegrino, J. Electron. Mater. **39**. 1036 (2010).

[2]J. D. Benson, S. Farrell, G. Brill, Y. Chen, P. S. Wijewarnasuriya , L. O. Bubulac, P. J. Smith, R. N. Jacobs, J. K. Markunas, M. Jaime-Vasquez, L. A. Almeida, A. Stoltz, U. Lee, M. F. Vileal, J. Peterson, S. M. Johnson, D. D. Lofgreen, D. Rhiger, E. A. Patten, and P. M. Goetz, J. Electron. Mater. **40**. 1847 (2011).

[3]R. N. Jacobs, A. J. Stoltz, J. D. Benson, P. Smith, C. M. Lennon, L. A. Almeida, S. Farrell, P. S. Wijewarnasuriya, G. Brill, Y. Chen, M. Salmon, and J. Zu, J. Electron. Mater. **42**. 3148 (2013).

[4]M. Nastasi, D. M. Parkin, and H. Gleiter, Mechanical properties and deformation behavior of materials having ultra-fine microstructures, Springer-Science+Business Media, B.V, (1992).

[5]R. E. Smallman, and R. J. Bishop, Modern physical metallurgy and materials engineering science, process, and application 6th edition, Butterworth-Heinemann, (1999).

[6]S. Farrell, G. Brill, Y. Chen, P. S. Wijewarnasuriya, M. V. Rao, N. Dhar, and K. Harris, J. Electron. Mater. **39**. 43 (2010).

[7]S. Farrell, M. V. Rao, G. Brill, Y. Chen, P. Wijewarnasuriya, N. Dhar, D. Benson, and K. Harris, J. Electron. Mater. **40**. 1727 (2011).

[8]A. J. Stoltz, J. D. Benson, M. Carmody, S. Farrell, P.S. Wijewarnasuriya, G. Brill, R. Jacobs, Y. Chen, J. Electron. Mater. **40**. 1785 (2011).

[9]A. J. Stoltz, J. D. Benson, R. Jacobs, P. Smith, L. A. Almeida, M. Carmody, S. Farrell, P. Wijewarnasuriya, G. Brill, and Y. Chen, J. Electron. Mater. **41**. 2949 (2012).

[10]S. Simingalam, J. Pattison, Y. Chen, P. Wijewarnasuriya, and M. V. Rao, J. Electron. Mater. **45**. 4668 (2016).

[11]J. D. Benson, P. J. Smith, R. N. Jacobs, J. K. Markunas, M. Jaime-Vasquez, L. A. Almeida, A. Stoltz, L. O. Bubulac, M. Groenert, P. S. Wijewarnasuriya, G. Brill, Y.Chen, and U. Lee, J. Electron. Mater. **38**. 1771 (2009).

[12]W. J. Everson, C. K. Ard, J. L. Sepich, B. E. Dean, G. T. Neugebauer, and H. F. Schaake, J. Electron. Mater. **24**, 505 (1995).

[13]J. E. Ayers, Hetero-Epitaxy of Semiconductors: Theory, Growth, and Characterization New York, NY: CRC Press, pp. 332–338, (2007)

[14]S. Farrell, M. V. Rao, G. Brill, Y. Chen, P. Wijewarnasuriya, N. Dhar, D. Benson, and K. Harris, J. Electron. Mater. **40**. 1727 (2011).

[15]R. N. Jacobs, J. Markunas, J. Pellegrino, L. A. Almeida, M. Groenert, M. Jaime-Vasquez, N. Mahadik, C. Andrews, and S.B. Qadri, J. Cryst. Growth. **310**. 2960 (2008).

[16]J. D. Benson, L. O. Bubulac, P. J. Smith, R. N. Jacobs, J. K. Markunas, M. Jaime-Vasquez, L. A. Almeida, A. Stoltz, P. S. Wijewarnasuriya, G. Brill, Y. Chen, U. Lee, M. F. Villa, J. Peterson, S. M. Johnson, D. D. Lofgren, D. Rhiger, E.A. Patten, and P. M. Goetz, J. Electron. Mater. **39**. 1080 (2010).

CHAPTER 5

MICROSTRUCTURAL CHARACTERIZATION OF DEFECTS AND CHEMICAL ETCHING FOR HgCdSe/ZnTe/Si(211)HETEROSTUCTURES

This chapter describes defect characterization in HgCdSe/ZnTe/Si(211) films and attempts to identify an etchant suitable for delineation of defects through etch pit decoration in HgCdSe(211). This project was carried out in collaboration with: Dr. Kevin Doyle and Dr. Priyalal Wijewarnasuriya at Army Research Laboratory. The major findings have been submitted for publication recently.

5.1. Introduction

Defects in $Hg_{1-x}Cd_xTe$ (MCT) have long been recognized as a major factor causing deterioration of IR detectors.[1] Since efforts to reduce dislocation density below 10^6 cm^{-2} for MCT grown on large-area substrates such as Si have not proven to be effective, the search for alternative materials to substitute for MCT has been the focus of ongoing research.[2] Some of the potential candidates include $Pb_{1-x}Sn_xTe$, $Pb_{1-x}Sn_xSe$, $In_{1-x}Ga_xAs$, InSb and $Hg_{1-x}Cd_xSe$.[3] The last of these materials, $Hg_{1-x}Cd_xSe$ (MCS), has many properties that suggest optimal IR device performance but MCS has so far not been well explored for IR applications. The similar semiconductor-to-semimetal transitions, and tunable band gaps of MCS and MCT mean that the two materials should have comparable IR performance.[4] Figure 5.1 illustrates the similarity of variation of bandgap energy and cut-off wavelength as a function of Cd concentration x for both HgCdTe and HgCdSe at 77K and 300K.[5]

A major difference between the materials is that as-grown MCS appears to have *n*-type intrinsic defects such as Se vacancies, while most as-grown MCT contains *p*-type Hg vacancies [4]. Moreover, CdSe crystallizes in the hexagonal wurtzite structure, with lattice parameter *a* ranging from 4.299 to 4.309 Å and *c* ranging from 7.009-7.024 Å at room temperature, compared to HgSe, HgTe, and CdTe which crystallize in the cubic zincblende structure [4,6]. Zincblende and Wurtzite structures are shown next to each other in Fig 5.2.[7]

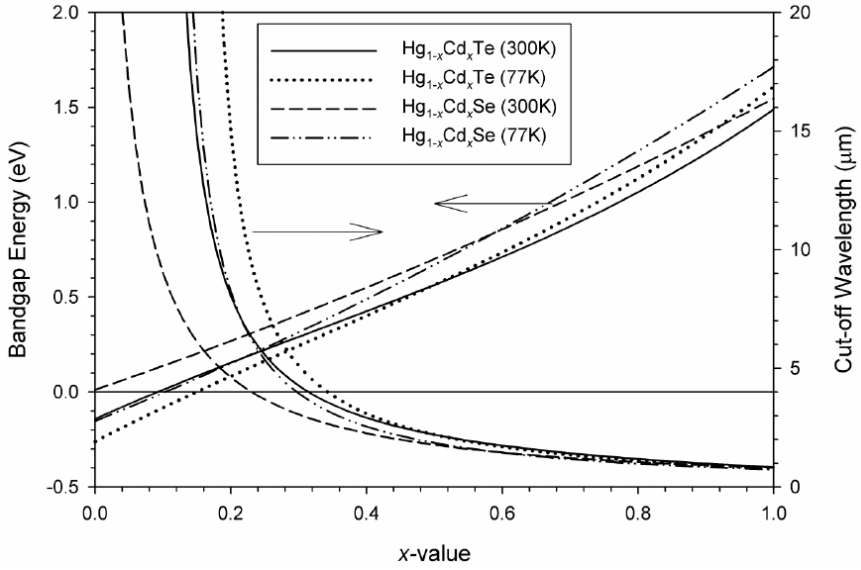

Figure 5. 1 Comparison of bandgap and cut-off wavelength variation for both $Hg_{1-x}Cd_xSe$ and $Hg_{1-x}Cd_xTe$ as a function of Cd concentration "*x*".[5]

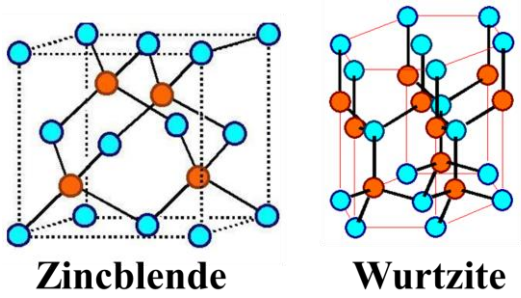

Figure 5. 2 Schematic of zincblende and wurtzite crystal structures.[7]

For all possible infrared applications (x<0.77), $Hg_{1-x}Cd_xSe$ crystallizes in a single-phase zincblende structure which would match with potential substrates such as GaSb and Si which have the zincblende structure.[6] Additionally, since variations in a_0 (i.e., lattice constant) with composition x are much reduced for MCS compared to MCT, then MCS might possibly be a preferred option for multijunction focal-plane arrays (FPA).[6] In other words, a multijunction of LWIR $Hg_{1-x}Cd_xTe$ on MWIR $Hg_{1-x}Cd_xTe$ is more susceptible to generation of misfit dislocations and subsequently device deterioration than $Hg_{1-x}Cd_xSe$ ones. Moreover, the availability of commercial bulk wafers of III-V compounds such as GaSb with initial low dislocation densities (~ 10^4 cm^{-2}) and close lattice-matching to MCS, would appear to make HgCdSe attractive for the next generation of IR detectors.[8]

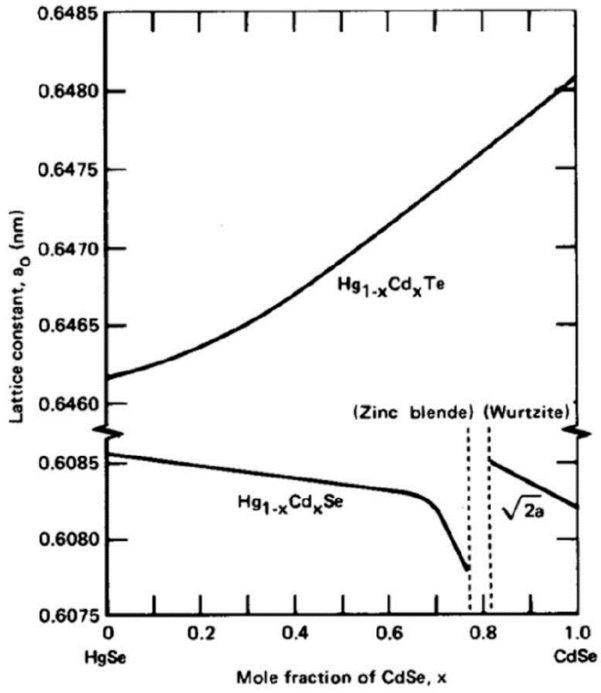

Figure 5. 3 Comparison of lattice constant (a_0) variation for $Hg_{1-x}Cd_xSe$ and $Hg_{1-x}Cd_xTe$ as a function of Cd concentration "x", the change of crystal structure from zincblende to wurtzite is shown as split close to x=0.8.[5]

Many other factors, such as lower price, larger available wafer size, and Si-based read-out integrated circuits for IR detectors, make Si a more attractive substrate.[9] Because of the large lattice mismatch (12.3%) between MCS and Si, direct epitaxial growth of MCS on Si is likely to generate highly defective films that will result in poor detector performance. Previous attempts to grow MCS by molecular beam epitaxy (MBE) have been reported.[10,11] Details about growth rate, effect of choice of Se effusion cell on Cd/Se ratio, optimal substrate temperature, electron concentration and impurity characterization, correlation of growth temperature and defects, can be found elsewhere.[10-12] The growth of composite layers to mediate the large lattice mismatch between MCS and Si should continue to be investigated in order to achieve lower defect densities within the MCS layer.

The development of chemical solutions that will etch IR materials selectively at defective regions to provide a reliable estimate of defect density via correlation with etch pits is recognized an important step in efforts towards developing next-generation IR materials.[4] Different chemical solutions such as Schaake and Benson etchants have been developed for delineating dislocations in MCT (211), and one-to-one correspondence between different etch pits and dislocations in MCT (211) has been demonstrated.[2,13] However, these etchants proved to be ineffective for MCS due to differences in selenide and telluride chemistry, and there have been no reported attempts to develop etchants suitable for evaluating MCS (211) films. In this chapter, high-resolution (scanning) transmission electron microscopy (HR(S)TEM) techniques have been used to study HgCdSe/ZnTe/Si (211) heterostructures etched in different solutions. In addition, Focused-Ion-Beam (FIB) milling has been used to prepare site-specific cross-section

specimens containing etch pits that had been created using different etchants. These observations provide microstructural information about the defects that are induced during MCS growth in addition to providing insight for developing solutions for future measurements of etch-pit density.

5.2. Experimental details

Samples of $Hg_{1-x}Cd_xSe$ with x ranging from 0.19 to 0.33 with typical thicknesses of 2 or 4μm were grown by molecular beam epitaxy (MBE) with a DCA 400 system using 20cm×20cm pieces of Si(211) substrates and ~ 9 μm ZnTe buffer layers. Sample details are provided in Table 5.1, and information about ZnTe growth on Si (211) can be found elsewhere.[14] Approximate thicknesses of 0.5μm of ZnTe were removed before MCS growth using a methanol-base dilute solution of bromine. Residual oxide layers were removed after several methanol rinses followed by a dilute aqueous HCl dip, and then rinsed with running deionized water. Upon loading in the MBE chamber, the samples were heated to remove excess Te. To avoid surface roughness, final heating was performed under Te overpressure. Reflection-high-energy electron diffraction (RHEED) was used to monitor growth. Elemental sources of Hg, Cd and Se with nominal fluxes of ~ 2×10^{-4} Torr, ~4×10^{-6} Torr and ~ 7×10^{-7} Torr respectively were used for MBE growth. The growths were conducted at temperatures ranging from 120°C to 190°C.

Sample number	Growth Temperature (°C)	x value	$Hg_{1-x}Cd_xSe$ Thickness (μm)	ZnTe Thickness (μm)
SZ73	122	0.33	2.4	8.7
SZ74	123	0.31	3.6	9.2
SZ79	122	0.22	4.2	8.9
SZ54	185	0.20	3.4	9.1
SZ59	162	0.19	3.8	9.1

Table 5. 1 Description of MCS samples studied in this chapter.

For the first set of samples, buffering agents included H_2O, HF, CH_3COOH, H_3PO_4 and $C_3H_6O_3$ were selected for etching.[15] However, based on previous documented investigations that demonstrated solutions of HNO_3 and HCl were serving as preferential etchants for HgSe and CdSe, solutions of HNO_3, HCl, and several buffering agents in varying ratios were later tested on the MCS samples. These solutions were found to produce roughly triangular pits on MCS samples of optimal shape and size as viewed under Nomarski microscopy.[16]

Cross-section TEM (XTEM) observations were made to check for a 1:1 correspondence between visible etch pits and threading dislocations. XTEM samples of the as-grown MCS were prepared using standard mechanical polishing and dimpling to thicknesses of about 10 μm, followed by Ar-ion milling at liquid nitrogen temperature to produce electron-transparent films.[11] To reduce the effect of ion-beam-induced damage, final thinning was conducted at 2.0 keV. For the etched samples, an FEI Nova200 dual-

beam system was used for site-specific XTEM sample preparation. Deposition of a thin layer of carbon, followed by 200-300 nm of Pt in electron-beam mode and 2μm Pt in Ga^+ beam-mode, were implemented for protection against ion-milling damage. Samples were then thinned at 0.1nA using 30keV Ga^+ ions. Most samples were prepared for TEM imaging in $<0\bar{1}1>$ projection while some were prepared along $<\bar{1}11>$. Philips FEI CM-200, JEOL JEM-4000EX, and JEOL ARM-200F electron microscopes were used for microstructural characterization.

5.3. Results and discussion

5.3.1. As-grown Materials

Figure 5.4 shows low-magnification BF (bright-field) TEM images of samples labelled SZ79 and SZ73. In both cases, the dislocation density is highest close to the ZnTe/Si interface, but dislocations entangle as the ZnTe layer gets thicker so that the upper regions are less defective near the MCS/ZnTe interface. The high density of defects at the ZnTe/Si interface can be attributed to the large lattice mismatch between Si and ZnTe. Selected-area electron diffraction patterns (SAED) for samples SZ79 and SZ59 showed ~ 2.5° rotation tilt between ZnTe and Si, which is in agreement with predictions for minimization of strain energy of closed-packed planes projected along the interfaces of (211) films.[17]

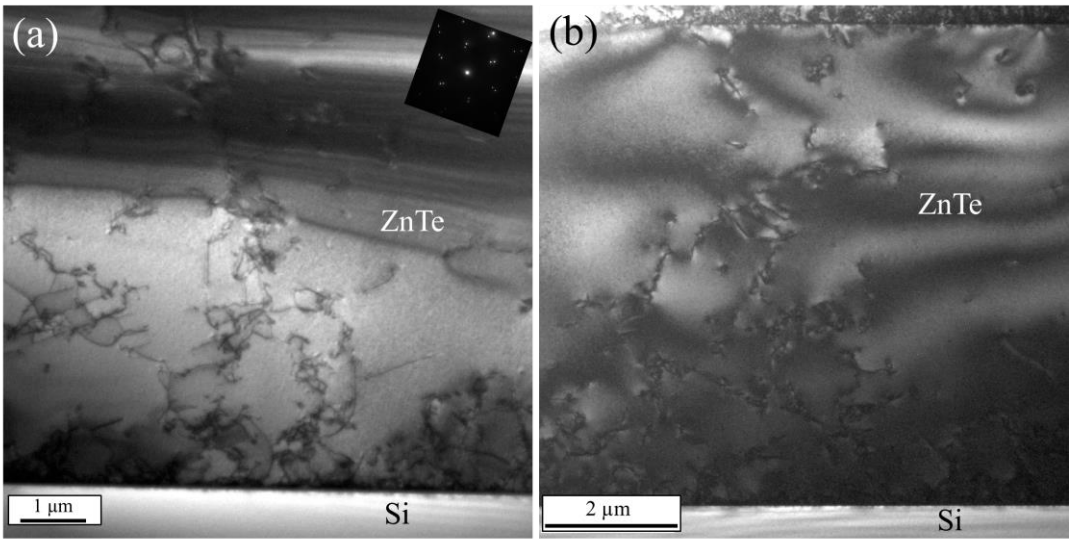

Figure 5. 4 XTEM micrographs of as-grown ZnTe/Si samples viewed in $<0\,\bar{1}1>$ projections: (a) sample SZ79; (b) sample SZ73.

The microstructure of the ZnTe/Si(211) interfaces was very similar in all samples. Figure 5.5(a) shows the rough saw-tooth structure of the ZnTe/Si interface, while the lattice images visible in Figures 5.5(b) and 5.6(a) show that the interface is often decorated with stacking faults (SFs) that are inclined at ~ 19° and ~ 90° with respect to the interface plane. Similar SFs have been previously reported at ZnTe/Si interfaces.[18,19] Image analysis was carried out by taking Fourier transforms (FT) of a square boxed region around the defect, selecting pairs of corresponding (111) spots and then applying an inverse Fourier transform (IFT).

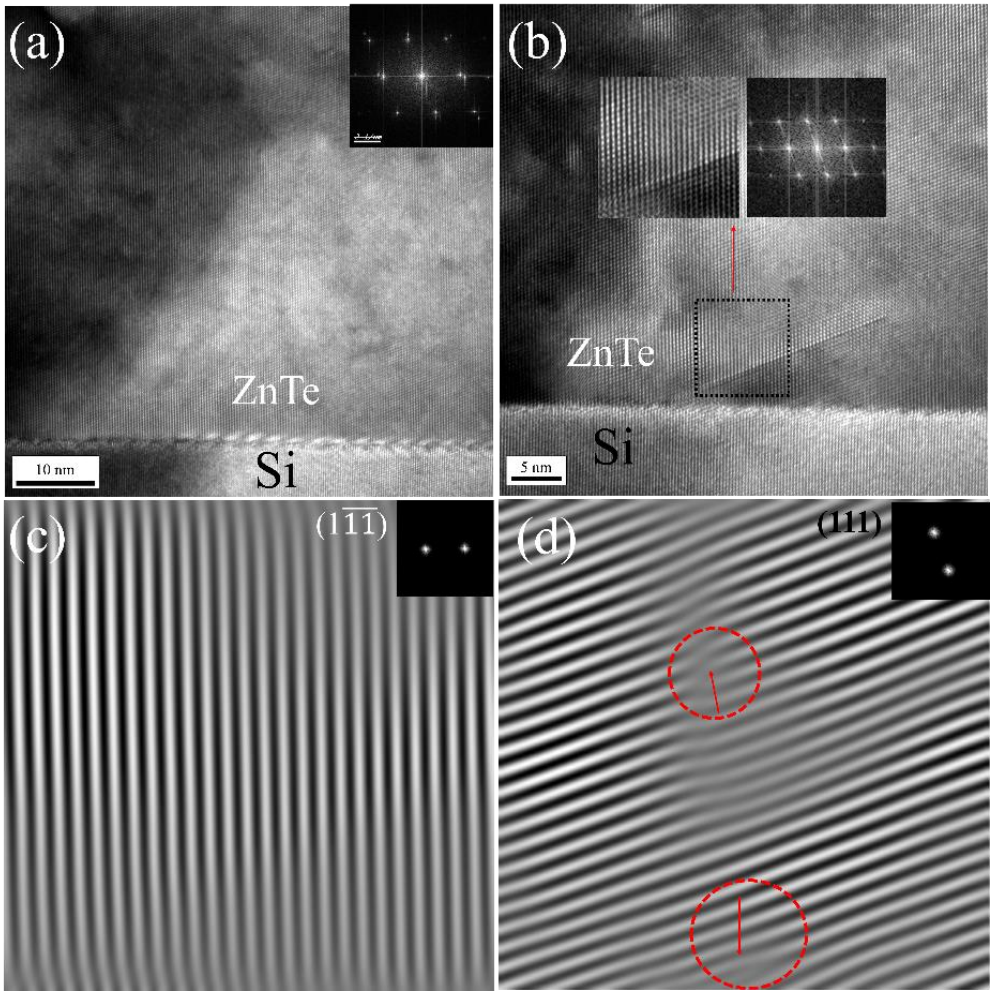

Figure 5. 5 HR-XTEM images: (a) ZnTe/Si saw-tooth interface in sample SZ79 with FT inset; (b) ZnTe/Si interface in SZ79 with ~ 19° SF. Area used for reconstruction is enclosed by black square with corresponding FFT as inset, (c) reconstructed (1$\bar{1}\bar{1}$), and (d) reconstructed (111) planes for ~ 19° SF.

The extra half-planes for the 19° SFs lie on (111) planes, as shown in Fig. 5.5(d). This is expected since these (111) lattice planes make a 19.4° angle with respect to the (211) surface normal and the SF extends along this plane. Since these planes are the fault planes for defects with $\frac{1}{6} < 211 >$ Burgers vector, they can be attributed to Shockley

partial dislocations. The extra half planes for the 90° SFs are inserted along $(\bar{1}11)$ planes that are normal to (211), as visible in Fig 5.6(b). Thus, these SFs are identified as extrinsic Frank partial dislocations associated with Burgers vector of $\frac{1}{3}\langle\bar{1}11\rangle$. Formation of these low-energy SFs in zincblende semiconductors is commonly attributed to non-optimized growth conditions.[20]

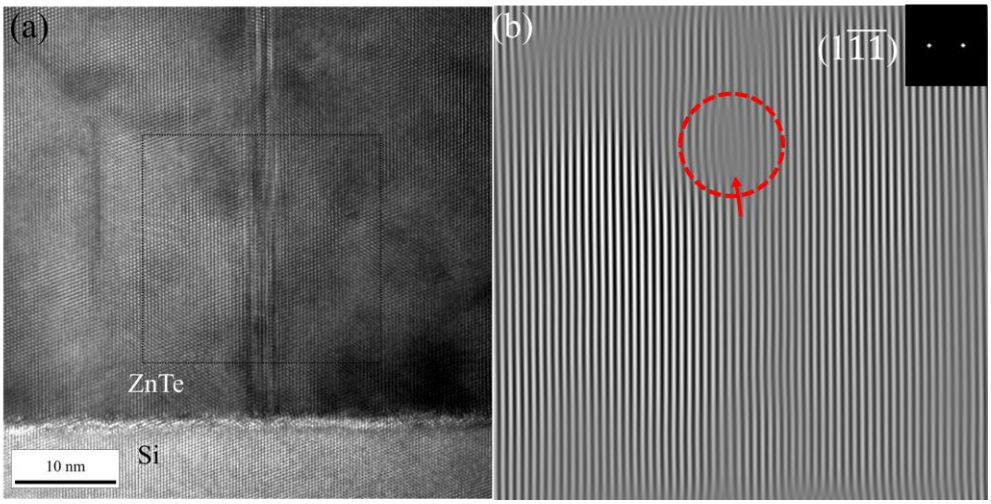

Figure 5. 6 (a) HR-XTEM image of ZnTe/Si interface in sample SZ73 showing ~ 90° SF. Area used for analysis is enclosed by a black square, and (b) corresponding reconstructed $(1\bar{1}\bar{1})$ FFT.

Figure 5.7 (a) shows a BF STEM micrograph of the ZnTe/Si region for the sample SZ74. Fourier analysis was performed to identify extra half-planes at the interface. For a 16 nm length along this interface, 71% of the extra half-planes lie along $(\bar{1}11)$ planes. Construction of a Burgers circuit around one of these dislocations showed that the corresponding Burgers vector was $\frac{a}{3}\langle\bar{1}11\rangle$, while dislocations with an extra half plane on (111) had Burgers vector at an approximate 45 degree with length of $\frac{a}{3}\langle111\rangle\ /Cos(45)$.

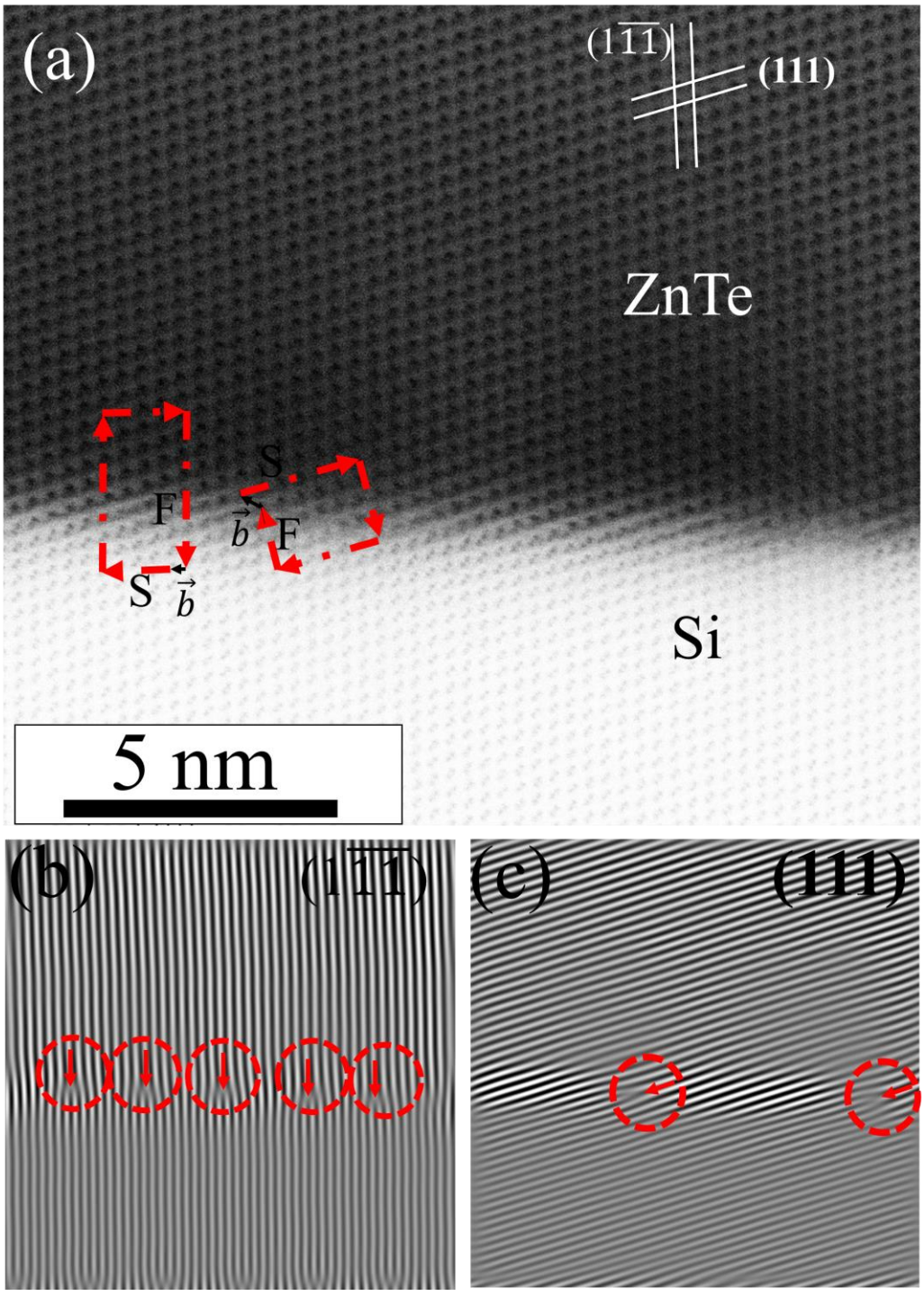

Figure 5. 7 BF STEM micrograph of ZnTe/Si of sample SZ74 showing Burgers circuit analysis, (b) reconstructed (1$\bar{1}\bar{1}$), and (c) reconstructed (111) planes. Positions of extra planes are circled.

The MCS/ZnTe interface in all four samples studied was very defective, with many defects threaded all the way to the top MCS surface, as shown in Figs. 5.8 (a-f). The MCS quality for sample SZ73 was considerably lower than the rest of the set, Fig. 5.8(c).

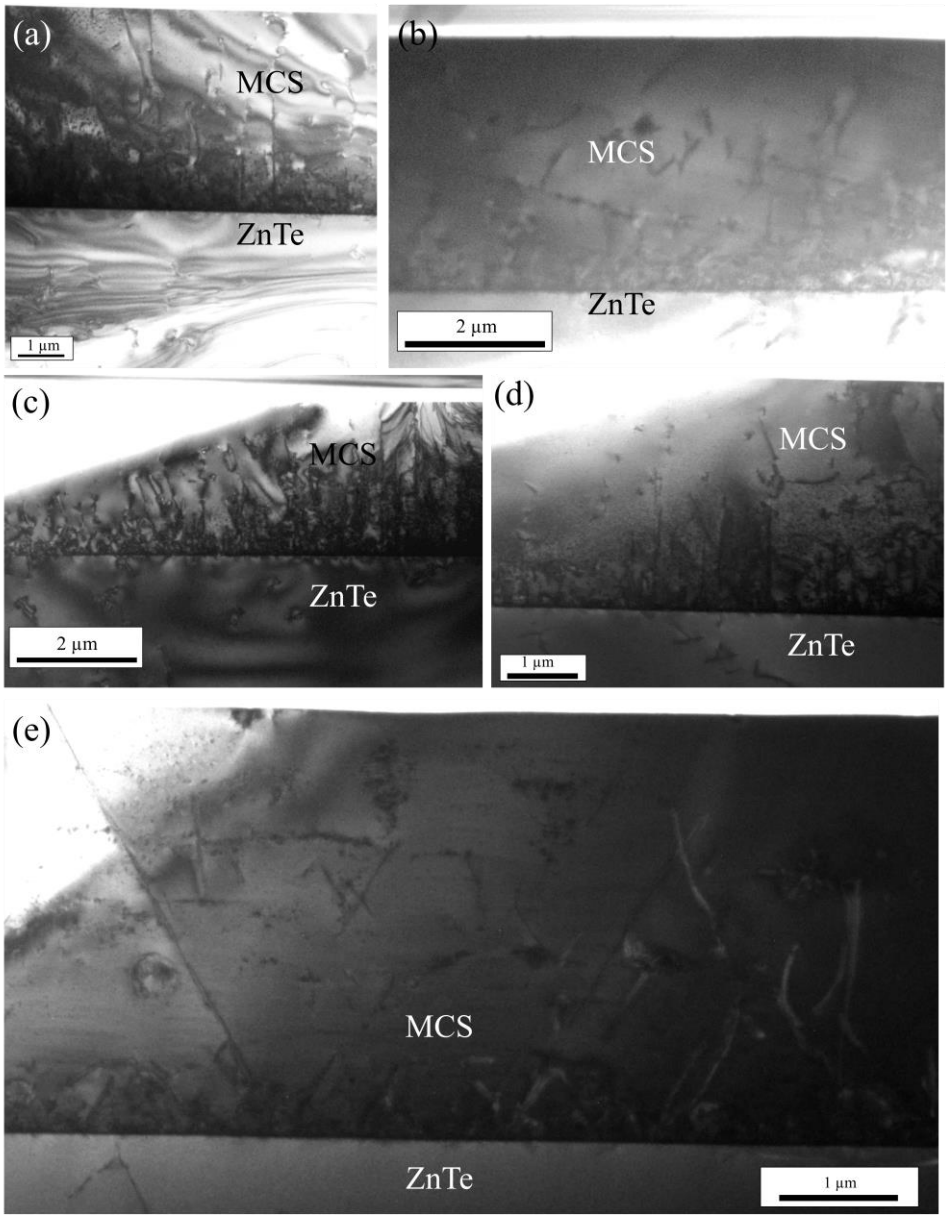

Figure 5. 8 Low-magnification XTEM micrographs of: (a) sample SZ79, (b) sample SZ59, (c) sample SZ73, and (d) sample SZ74 with <0$\bar{1}$1> zone axis; and (e) sample SZ54 with <$\bar{1}$11> zone axis.

High-resolution imaging, Fig. 5.9 (a), showed that MCS/ZnTe had a saw-tooth interface with stacking faults again appearing at 19° and 90° angles with respect to the interface plane. Similar SFs are also present near the top surface in all of these MCS samples, as shown by the examples in Figs. 5.9(b,c).

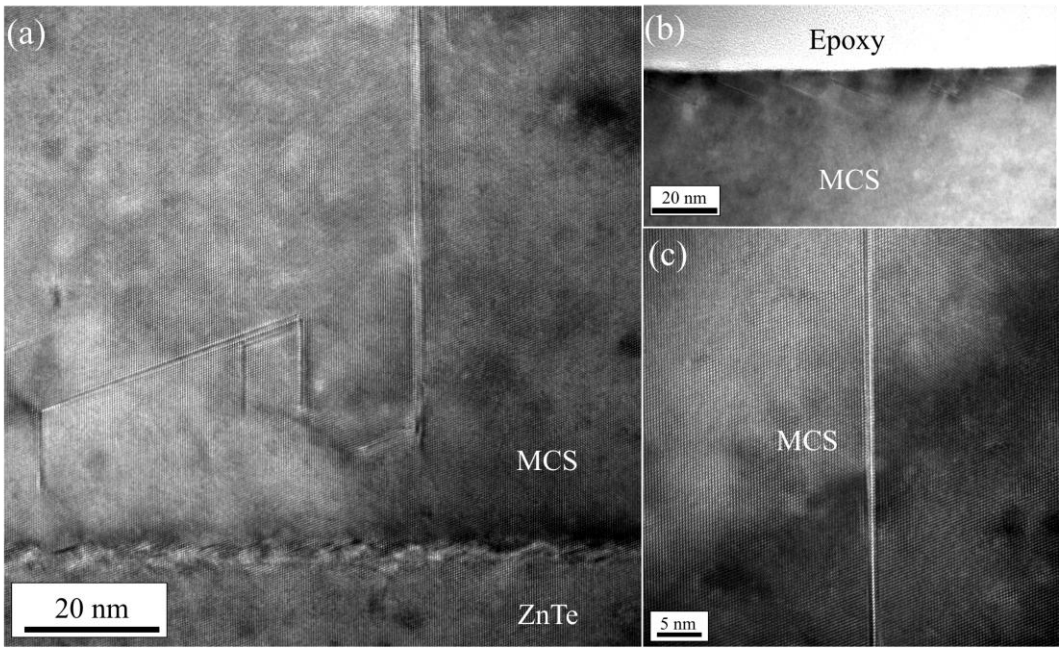

Figure 5. 9 HR-XTEM micrographs of MCS/ZnTe with <0$\bar{1}$1> orientation: (a) sample SZ73, (b) sample SZ59, and (c) sample SZ79.

Figures 5.10(a-d) show BF, high-angle annular-dark-field (HAADF) and reconstructed (1$\bar{1}\bar{1}$) and (111) planes at the MCS/ZnTe interface for sample SZ74. All of the extra half-planes along 13 nm of this interface were observed to lie on (1$\bar{1}\bar{1}$) planes with $\frac{a}{3}\langle\bar{1}11\rangle$ Burgers vector.

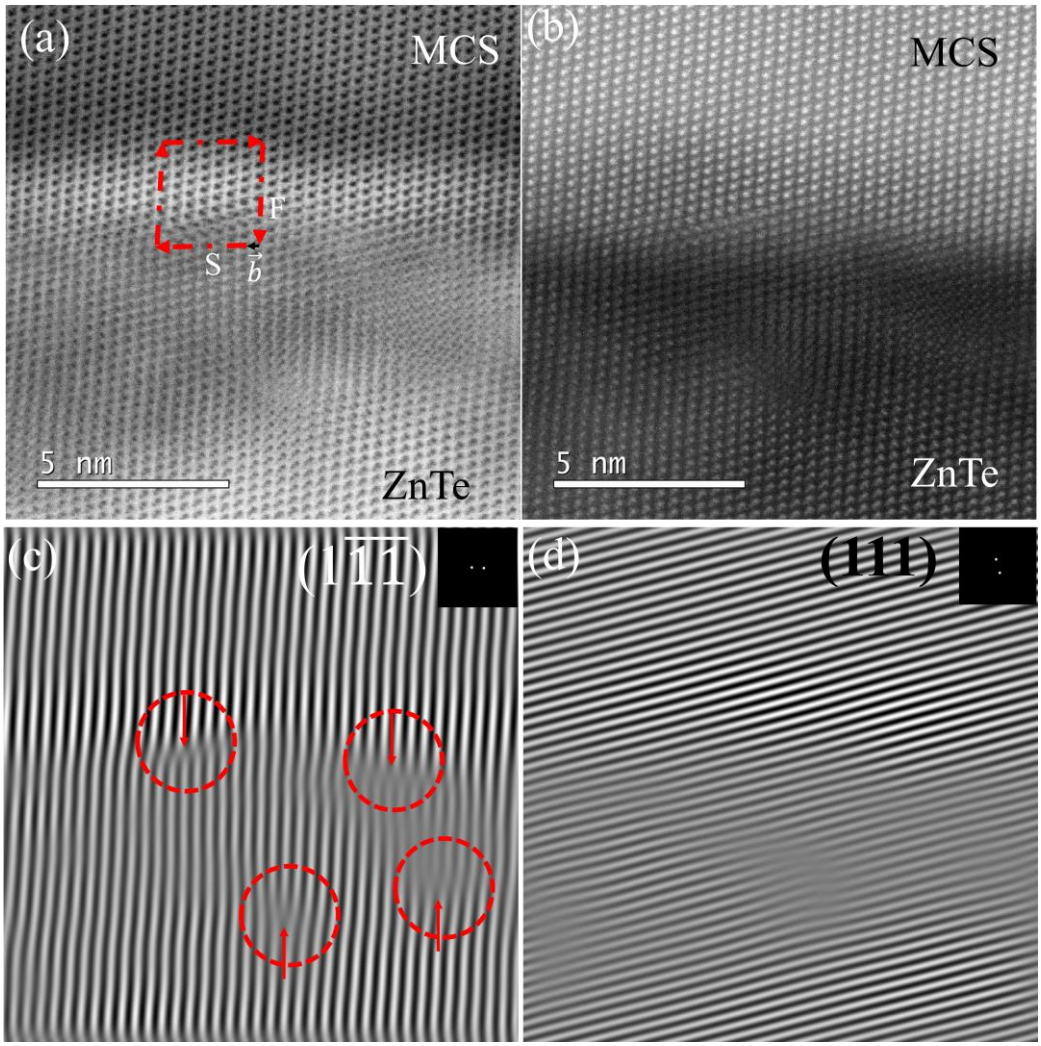

Figure 5. 10 (a,b) BF and HAADF STEM images of MCS/ZnTe of sample SZ74, (c,d) reconstructed $(1\bar{1}\bar{1})$ and (111) planes. Extra planes are circled.

5.3.2. Etched Materials

A series of chemical solutions with buffering agents including H_2O, HF, CH_3COOH, H_3PO_4 and $C_3H_6O_3$ were prepared to selectively etch the MCS surface in attempts to correlate defects in the MCS layers with etch pits on the surface. Figures 5.11(a,c) show a plan-view SEM micrograph of a selected pit for SZ73A. This image shows pits that are roughly round with relatively large diameters. The first piece selected for observation was deliberately extracted from an area away from the pits, as shown in Fig. 5.11(a). Although the XTEM micrograph in Fig. 5.11(b) shows relatively defect-free MCS in the upper regions, short defects are still visible near the top of the MCS film. Figures 5.11(c,d) show another pit and the corresponding XTEM image. Several threading dislocations are visible under the pit in this case. Similar analysis was also done for sample SZ73-B, as shown in Figs. 5.11(e,f). In this case, the pit had a smaller depth and there are several terminated dislocations, but some were missed by the etchant on the left hand side. Figure. 5.11(g) shows a higher magnification image of one of these defects that was not etched.

After unsuccessful experiments with buffering agents included H_2O, HF, CH_3COOH, H_3PO_4 and $C_3H_6O_3$ etchants, another set of chemical etchant solutions, labeled in table 5.2 as E1, E3 and E6, were prepared and tested. In all cases, the etch pit morphology was close to an isosceles triangle with rough edges, as shown in Figs. 5. 12(a,c,e), However, for XTEM cross-sections of E1 and E3 pits, some defects were again excluded from the etched area, as shown on the left hand side of Figs. 5.12(b,d). E6 solution produced a sharper triangular morphology, but its depth was so large that it extended almost as deep as the MCS/ZnTe interface.

Overall, it appears all of the etchants captured several defects while missing some. The last chemical solution, i.e. E6 with concentration ratio of HNO_3:HCl:Lactic 4:0.3:1 and etching time 50 seconds, seems to be the next starting point for setting the concentration and time for developing an etchant with pits that have one-to-one correspondence with defects.

Etchant code	**Sample number**	**Chemical ratio**	**Etching time**
E1	SZ74	HNO_3:HCl:Lactic 20:0.8:4	50 seconds
E3	SZ74	HNO_3:HCl:Lactic 20:0.8:6	45 seconds
E6	SZ54	HNO_3:HCl:Lactic 4:0.3:1	50 seconds

Table 5. 2 Description of nitric acid base solutions for selective etching of MCS samples.

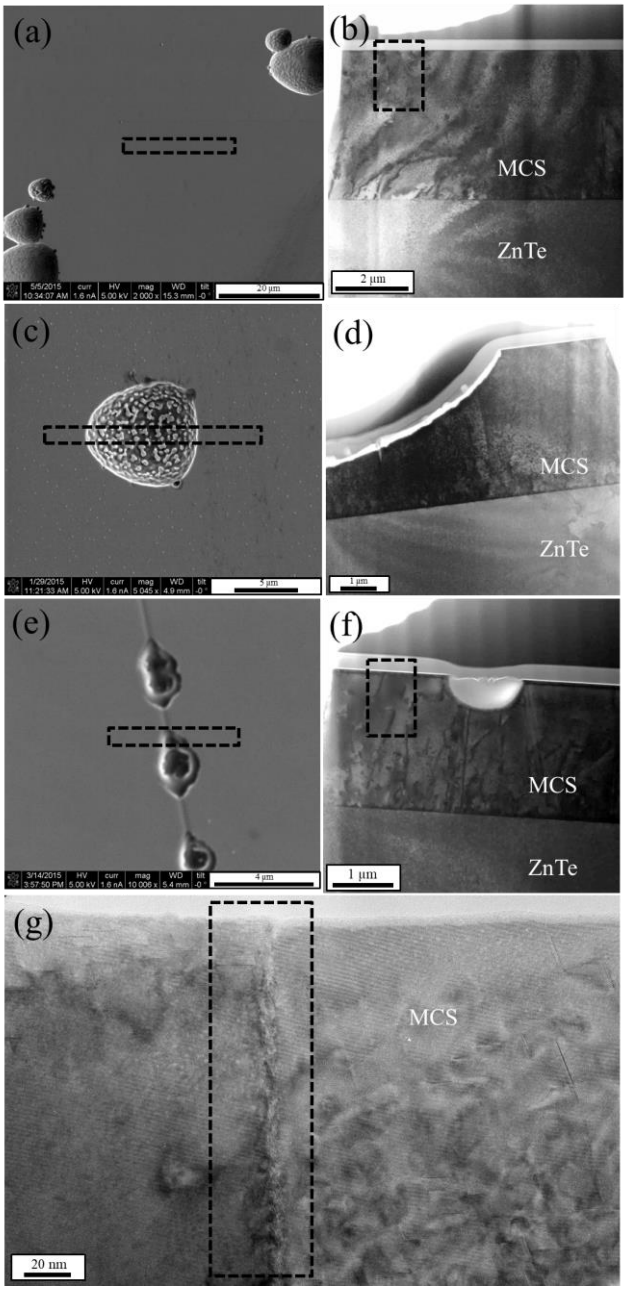

Figure 5. 11 (a) Plan-view SEM images of sample SZ73A. FIB-cut area from regions without pits is marked with a box, (b) XTEM image of the lift-out sample from area without pit. Short defects missed by etching are visible within the box, (c) Sample across the pit, (e) Plan-view SEM image of sample SZ73B, FIB-cut area across a pit is marked by the box, (f) XTEM image of the lift-out sample across the pit; and (g) HRTEM image of the area on left side of the pit. Defect marked with the box.

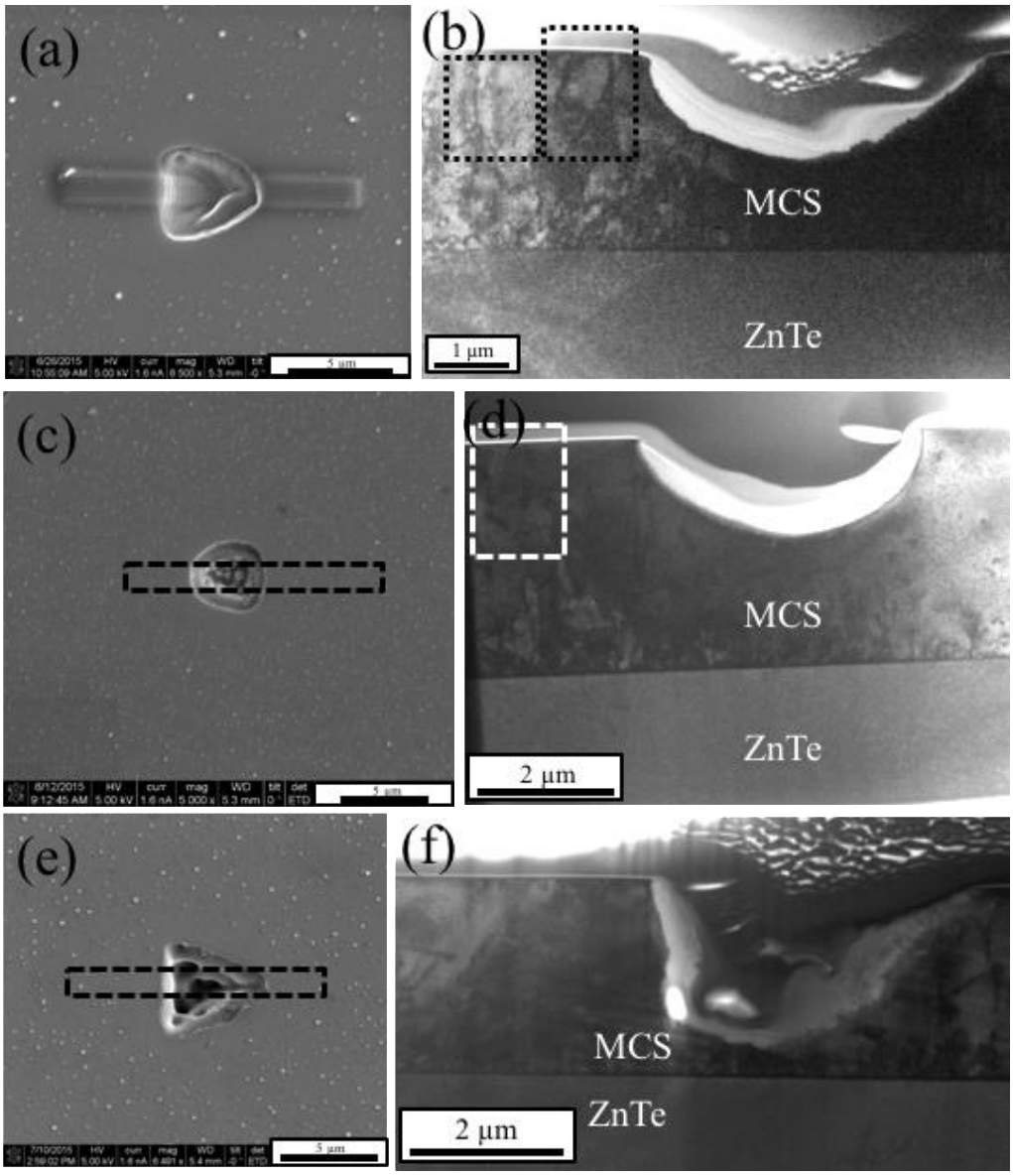

Figure 5. 12 (a) Plan-view SEM images of sample SZ74-E1, FIB-cut area is coated with Pt, (b) XTEM image of the lift-out sample. Dislocation threads missed by etching at the top of MCS are marked by two boxes, (c) Plan-view SEM image of sample SZ74-E3, FIB-cut area is marked with a box across the pit, (d) XTEM image of the lift-out sample across the pit, (e) Plan-view SEM images of sample SZ54-E6, FIB-cut area is marked with a box across the pit, (f) XTEM image of the lift-out sample across the pit.

5.4 Conclusions

In summary, XTEM analysis showed large dislocation density at ZnTe/Si(211) interfaces in all samples, which dropped off rapidly as ZnTe grows. A 2.5° lattice rotation between ZnTe and Si was recorded in SAED patterns.

A detailed microstructural analysis showed that in both HgCdSe/ZnTe and ZnTe/Si interfaces, stacking faults appeared at 19.5 and 90 degrees with respect to the interface. These stacking faults were attributed to Shockley and Frank partials, respectively. Atomic-resolution STEM images showed that the large lattice mismatch at the ZnTe/Si interface was accommodated through {111}-type stacking faults that had dislocations with Burgers vectors of either $\frac{a}{3}\langle\bar{1}11\rangle$ and $\frac{a}{3}\langle 111\rangle/Cos(45)$. Initial attempts to delineate individual dislocations using several different etching solutions revealed that the etchants had successfully etched away defective areas, but many nearby defects were unaffected by the etchant in close proximity to the pits.

References

[1]P. Wijewarnasuriya, Y. Chen, G. Brill, N. Dhar, D. Benson, L. Bubulac, and D. Edwall, J. Electron. Mater. **39**. 1110 (2010).

[2]M. Vaghayenegar, R. N. Jacobs, J. D. Benson, A. J. Stoltz, L. A. Almeida, D. J. Smith, J. Electron. Mater. **46**. 5007 (2017).

[3]J. Chu, and A. Sher, Physics and Properties of Narrow Gap Semiconductors, Springer, Chapter 1. p. 7 (2008).

[4]P. Capper, Narrow-gap II-VI Compounds for Optoelectronic and Electromagnetic Applications, Chapter 6. p. 204 (1999).

[5]C. R. Whitsett, J. G. Broerman and C. J. Summers, Semiconductors and Semimetals, vol.18, Chapter 2. p. 54. (1988).

[6]R. N. Andrews, F. R. Szofran, and S. L. Lehoczky, J. Cryst. Growth. **92**. 445 (1988).

[7]https://www.tf.uni-kiel.de/matwis/amat/semitech_en/kap_2/illustr/i2_1_2.html.

[8]G. Brill, Y. Chen, and P. Wijewarnasuriya, J. Electron. Mater. **8**. 1679 (2011).

[9]J. W. Garland and S. Sivananthan, in Springer Handbook of Crystal Growth, Ed. by G. Dhanaraj, K. Byrappa, V. Prasad, and M. Dudley (Springer Heidelberg Dordrecht London New York, (2010).

[10]K. Doyle, C. H. Swartz, J. H. Dinan, T. H. Myers, G. Brill, Y. Chen, B. L. Vanmil, P. Wijewarnasuriya, J. Vac. Sci. Technol., B. 31. 03C124 (2013).

[11]W. F. Zhao, G. Brill, Y. Chen, and D. J. Smith, J. Electron. Mater. 41. 2852 (2012).

[12]K. Doyle. Development of $Hg_{1-x}Cd_xSe$ for 3rd Generation Focal Plane Arrays. West Virginia University, UMI Number: 3576281 (2013).

[13]S. Farrell, M. V. Rao, G. Brill, Y. Chen, P. Wijewarnasuriya, N. Dhar, J. D. Benson, and K. Harris, J. Electron. Mater. **42**. 3097 (2013).

[14]Y. Chen, S. Simingalam, G. Brill, P. Wijewarnasuriya, N. Dhar, J.J. Kim, and D. J. Smith, J. Electron. Mater. **41**. 2917 (2012).

[15]K. Doyle, and S. Trivedi. Dislocation Etching Solutions for Mercury Cadmium Selenide ARL-CR-0744 (2014).

[16]P. Walker, and W. H. Tarn, Handbook of Metal Etchants, CRC Press LLC, pp. 221 and 809 (1991).

[17]S. Y. Woo, G. A. Devenyi, S. Ghanad-Tavakoli, R. N. Kleiman, J. S. Preston, and G. A. Botton, Appl. Phys. Lett. **102**. 132103 (2013).

[18]X. J. Wang, Y. Chang, C. R. Becker, C. H. Grein, S. Sivananthan, and R. Kodama, J. Electron. Mater. **40**. 1860 (2011).

[19]D. J. Smith, S. C. Y. Tsen, D. Chandrasekhar, P. A. Crozier, S. Rujirawat, G. Brill, Y. P. Chen, R. Sporken, and S. Sivananthan, Mater. Sci. Eng. B **77**, 93 (2000).

[20]Y. A. R. Dasilva, R. Kozac, R. Erni, M. D. Rossel, Ultramicroscopy. **176**, 11 (2017).

CHAPTER 6

SUMMARY AND POSSIBLE FUTURE WORK

6.1. Summary

Mercury cadmium telluride ($Hg_{1-x}Cd_xTe$ or MCT) has been the primary material used for infrared (IR) detectors and sensors due to its superior physical and electronic properties.[1] Due to its close lattice-matching with MCT, cadmium-zinc-telluride (CZT) has been the preferred substrate for MCT growth.[1] Recently, alternative substrates such as Si, GaAs, and GaSb, have been explored for MCT growth. Due to its maturity and many useful properties, Si has been of much interest for this purpose.[2-5] The research of this dissertation has focused on the characterization of Hg-based materials (HgCdTe and HgCdSe) for third-generation IR detectors using different transmission electron microscopy (TEM) techniques.

A systematic study of short-wavelength and long-wavelength (SWIR and LWIR) HgCdTe grown on CdTe/Si (211) by MBE showed large dislocation density at CdTe/Si(211) interfaces, which dropped rapidly as the CdTe thickness increased. A thin ZnTe layer mediated the large lattice mismatch of 19.5% between Si and CdTe. A lattice rotation of 3.7° between CdTe and Si was visible in SAED patterns. Growth of a thin HgTe buffer layer between HgCdTe and CdTe blocked some defects and seemed to improve the overall quality of the HgCdTe layers.

The development of next generation of HgCdTe IR detectors needs an easy and inexpensive method to estimate density of defects in absorbing material. Chemical etching and decoration of HgCdTe surface with etch pits that have 1:1 correspondence with dislocations is an effective approach for estimation of defect density. A detailed

microstructural study was done to investigate the morphology, distribution, and correlation of etch pits and dislocations in as-grown and thermal-cycle-annealed (TCA) HgCdTe (211) films that had been etched by Benson etchant. For as-grown samples, triangular and fish-eye pits were associated with Frank partial and perfect dislocations with $\frac{1}{2}[0\bar{1}1]$ Burgers vector, respectively.[6] Skew pits were determined to have a more complex nature. TCA successfully reduced the etch pit density by 72%. Although TCA processing eliminated the fish-eye pits, $\frac{1}{2}[0\bar{1}1]$ dislocations reappeared in shorter segments in TCA sample.[6] Large pits were observed in both as-grown and TCA samples, but the nature of the defects associated with these pits remains unknown.[6]

Mercury cadmium selenide ($Hg_{1-x}Cd_xSe$ or MCS), has many properties that suggest suitability for IR device but this material has not been well explored for this purpose.[7] Microstructural studies of several HgCdSe/ZnTe/Si (211) heterostructures showed large dislocation density at ZnTe/Si(211) interfaces, which dropped off rapidly as the ZnTe thickness increased. SAED patterns showed 2.5° rotation between the ZnTe and Si crystal lattices. Both HgCdSe/ZnTe and ZnTe/Si interfaces had stacking faults appearing at 19.5 and 90 degrees with respect to plane of the interface. These stacking faults were attributed to Shockley and Frank partials, respectively, and similar faults were also visible in upper regions of HgCdSe. Atomic-resolution STEM images showed that the large lattice mismatch at the ZnTe/Si interface was accommodated through {111}-type stacking faults. Initial attempts to delineate individual dislocations in HgCdSe revealed that while the etchants successfully attacked defective areas, many defects close to the pits were unaffected.

6.2. Future work

6.2.1. Improving MBE-Grown Hg-Based Material on Alternative Substrates

Although HgCdTe has been the preferred material for IR detectors since its discovery, and applications are still expanding, it suffers from high defect density, especially for as-grown materials on alternative substrates.[7] Hence, future studies for improving detector performance via optimizing growth conditions with alternative substrates and reducing defect density by applying post-processing techniques should be a major focus of future research. Meanwhile, research should continue on improving traditional HgCdTe/CdZnTe heterostructures and also investing in alternative designs such as HgTe/CdTe type-III superlattice structures.

6.2.2. HgTe/CdTe type-III superlattices

The type-III superlattice (SL) can be described as a periodic heterostructure with components A and B where the conduction band of A lies close to the valence band of B.[8] The HgTe/CdTe type-III superlattice was one of the first alternatives for LWIR detectors.[9] One underlying reason for its potential is due to significant suppressed Auger recombination in these quantum structures compared to the bulk HgCdTe alloy.[9] However, despite considerable efforts in this area, attempts to grow HgTe/CdTe SLs with properties comparable to HgCdTe alloys have so far been unsuccessful due to superlattice instabilities. These include weak Hg chemical bonding, internal electric fields due to strain mismatch between superlattice layers, change of band gap due to inter-diffusion in HgTe/CdTe SLs, and undesirable misfit dislocations.[9,10]

Figure 6.1 (a-e) show two different samples of type-III HgTe/CdTe superlattices grown on CdTe/Si (211) heterostructures by MBE. It is evident that SLs in all samples are very defective, and they are wavy in shape rather than flat in some cases. Moreover, the CdTe thickness was more than twice its designed value. Based on these preliminary TEM observations, significant in growth improvements will be needed before SL structures suitable for detector applications will be produced.

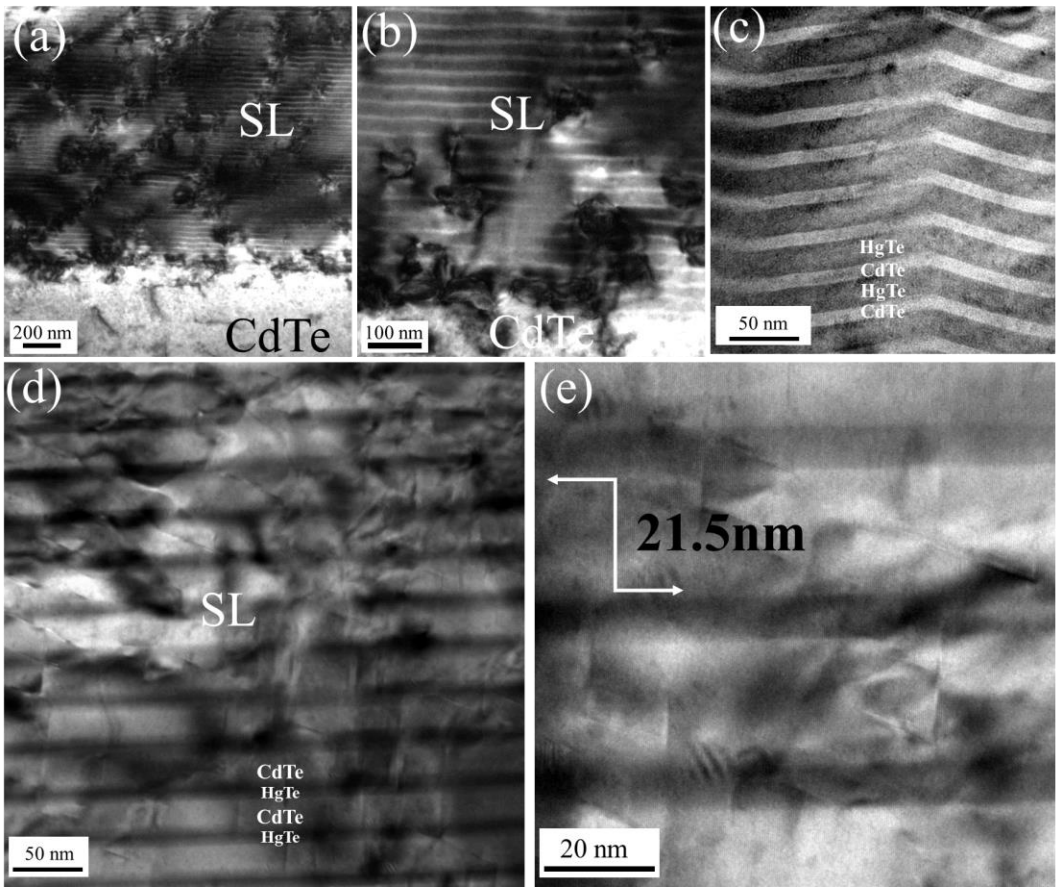

Figure 6. 1 Sample #hct15052: (a, b) Low-magnification images of SL/CdTe, and (c) Medium-magnification image of regions of SL with wavy structure. Sample#hct16003: (d) Medium-magnification image showing defective SL, and (e) High-magnification image revealing serious discrepancy between measured CdTe thickness of 21.5 nm and designed value of 8.8 nm.

6.2.3. HgCdTe grown by MBE on traditional CdZnTe substrates

Although perfectly lattice-matched with HgCdTe, growth on CdZnTe still faces challenges due to substrate irregularities such as presence of pits and Cd inclusions, as well as non-optimal growth parameters.[11-13] Figures 6.2 and 6.3 demonstrate different quality of MCT even when grown on the same CdZnTe wafer. While region A, Fig. 6.2(a-d), shows adequate quality with a few stacking faults in the upper regions of MCT, region B, Fig. 6.3(a-f), is very defective with micro-twins appearing in the bulk MCT, and an uneven saw-tooth top surface. The presence of a thin HgTe layer, ~ 10nm, is clear in HAADF images such as Fig. 6.4 (a). The growth conditions still obviously need to be optimized for uniform growth across the entire CZT wafer.

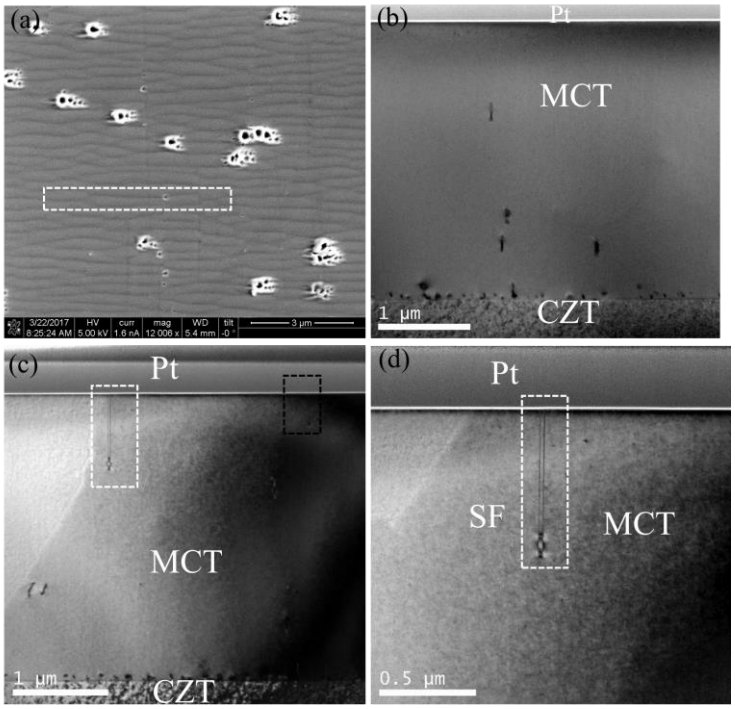

Figure 6. 2 (a) SEM micrograph of region A with better quality. FIB lift-out area is marked with a box, (b-d) XTEM images of MCT/CZT. Regions with stacking faults (SF) are marked with a box.

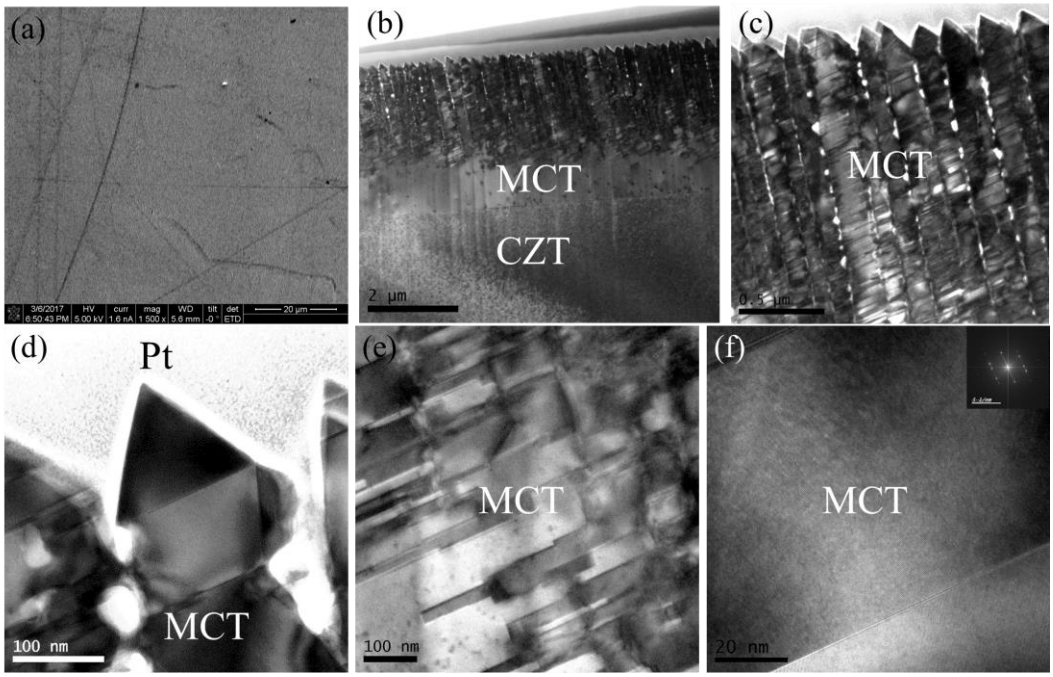

Figure 6. 3 (a) SEM micrograph of region B with low quality, (b-f) XTEM images of MCT/CZT.

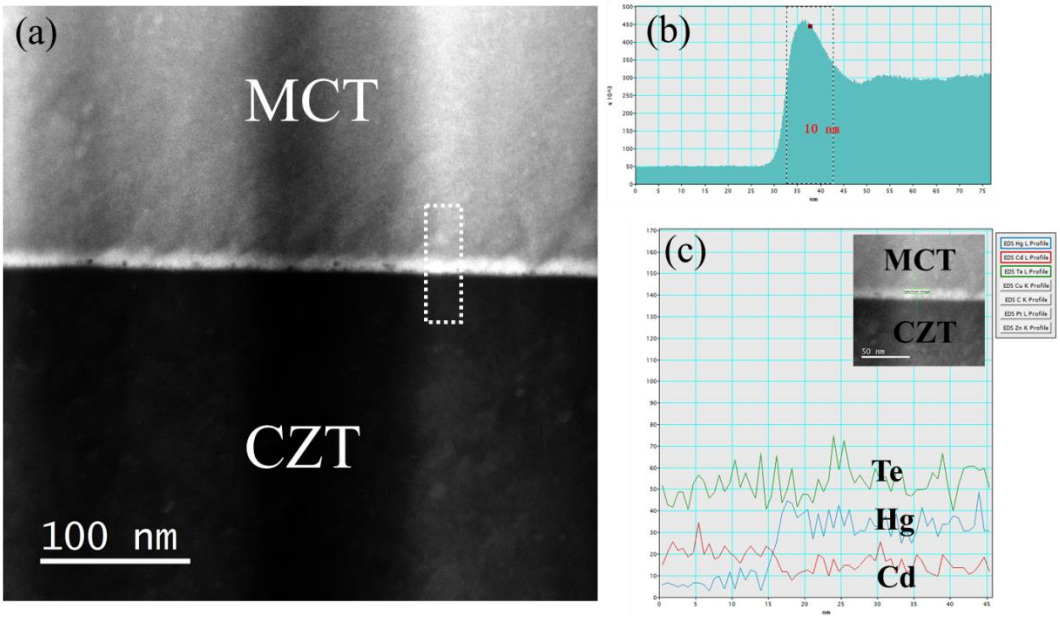

Figure 6. 4 (a) HAADF image of MCT/CZT interface, (b) Intensity profile along boxed region in Fig. 6.4(a), and (c) EDS line profile along MCT/HgTe/CZT.

References

[1]A. Rogalski, J. Antoszewski, and L. Faraone, J. Appl. Phys. **105**. 091101 (2009).

[2]J. W. Garland, S. Sivananthan, Springer Handbook of Crystal Growth. Chapter 32, 1070-1121 (2010).

[3]J. D. Benson, L. O. Bubulac, P. J. Smith, R. N. Jacobs, J. K. Markunas1 M. Jaime-Vasquez, L. A. Almeida, A. Stoltz, J. M. Arias, G. Brill, Y. Chen, P. S. Wijewarnasuriya, S. Farrell, and U. Lee, J. Electron. Mater. **41**. 2971 (2012).

[4]J. J. Kim, R. N. Jacobs, L. A. Almeida, M. Jaime-Vasquez, C. Nozaki, and David J. Smith, J. Electron. Mater. **42**. 3142 (2013).

[5]W. Lei, R. J. Gu, J. Antoszewski, J. Dell, and L. Faraone, J. Electron. Mater. **43**. 2788 (2014).

[6]M. Vaghayenegar, R. N. Jacobs, J. D. Benson, A. J. Stoltz, L. A. Almeida, D. J. Smith, J. Electron. Mater. **46**. 5007 (2017).

[7]P. Wijewarnasuriya, Y. Chen, G. Brill, N. Dhar, D. Benson, L. Bubulac, and D. Edwall, J. Electron. Mater. **39**. 1110 (2010).

[8]R. Tsu, Superlattice to Nanoelectronics 2nd edition, Elsevier, (2011).

[9]A. Rogalski, K. Adamiec, and J. Rutkowski, Narrow-Gap Semiconductor Photodiods, SPIE Press, (2000).

[10]M. A. Kinch, Fundamentals of Infrared Detector Materials, SPIE press, (2007).

[11]M. Reddy, D. D. Lofgreen, K. A. Jones, J. M. Peterson, W. A. Radford, J. D. Benson, and S. M. Johnson, J. Electron. Mater. **42**. 3114 (2013).

[12]M. Reddy, W. A. Radford, D. D. Lofgreen, K. R. Olsson, and S. M. Johnson, J. Electron. Mater. **43**. 2991 (2014).

[13]C. Xu, F. Sheng, and J. Yang, J. Electron. Mater. **46**. 5168 (2017).

REFERENCES

A. Garnier, G. Filoni, T. Hrncir, and L. Hladik, Microelectron. Reliab. **55**, 2135-2141 (2015).

A. J. Stoltz, J. D. Benson, M. Carmody, S. Farrell, P.S. Wijewarnasuriya, G. Brill, R. Jacobs, and Y. Chen, J. Electron. Mater. **40**. 1785 (2011).

A. J. Stoltz, J. D. Benson, R. Jacobs, P. Smith, L. A. Almeida, M. Carmody, S. Farrell, P. Wijewarnasuriya, G. Brill, and Y. Chen, J. Electron. Mater. **41**. 2949 (2012).

A. Rogalski, Infrared Phys. Technol. **50**, 240-252 (2007).

A. Rogalski, J. Antoszewski, and L. Faraone, Appl. Phys. Rev. **2**. 041303 (2015).

A. Rogalski, J. Antoszewski, and L. Faraone, J. Appl. Phys. **105**, 091101 (2009).

A. Rogalski, K. Adamiec, and J. Rutkowski, Narrow-Gap Semiconductor Photodiods, SPIE Press, (2000).

A. Rogalski, Opto-Electron. Rev. **20(3)**, 279-308 (2012).

A. Rogalski, Prog. Quantum Electron. **36**, 342-473 (2012).

A. Rogalski, Rep. Prog. Phys. **68**, 2267-2336 (2005).

B. Fultz, and J. M. Howe, Transmission Electron Microscopy and Diffractometry of Materials 3rd edition, Springer, (2008).

C. B. Carter, and D. B. Williams, Transmission Electron Microscopy Diffraction, Imaging, and Spectrometry, Springer, (2016).

C. R. Whitsett, J. G. Broerman and C. J. Summers, in Semiconductors and Semimetals, vol.18, Chapter 2. p. 54. (1988).

C. Wang, D. J. Smith, S. Tobin, T. Parados, J. Zhao, Y. Chang, and S. Sivananthan, J. Vac. Sci. Technol. A 24, **995** (2006).

C. Xu, F. Sheng, and J. Yang, J. Electron. Mater. **46**. 5168 (2017).

D. B. Williams, and C. B. Carter, Transmission Electron Microscopy A textbook for Materials Science 2nd edition, Springer, (2009).

D. J. Smith, S. C. Y. Tsen, D. Chandrasekhar, P. A. Crozier, S. Rujirawat, G. Brill, Y. P. Chen, R. Sporken, and S. Sivananthan, Mater. Sci. Eng. B **77**, 93 (2000).

E. P. G. Smith, R. E. Bornfreund, I. Kasai, L. T. Pham, E.A. Patten, J. M. Peterson, J. A. Rotha, B. Z. Noshoa, T. J. De Lyon, J. E. Jensena, J. W. Bangs, S. M. Johnson and W. A. Radford, Proc. of SPIE **Vol. 6127 61271F-1**, 8 (2006).

G. Brill, Y. Chen, and P. Wijewarnasuriya, J. Electron. Mater. **8**. 1679 (2011).

G. L. Hansen, J. L. Schmit, and T. L. Casselman, J. Appl. Phys. **53**, 7099 (1989).

G. Thomas, and M. J. Goringe, Transmission Electron Microscopy of Materials, Wiley–Interscience, New York, (1979).

https://www.tf.uni-kiel.de/matwis/amat/semitech_en/kap_2/illustr/i2_1_2.html.

J. Chu, and A. Sher, Physics and Properties of Narrow Gap Semiconductors, Springer, Chapter 1. p. 7 (2008).

J. D. Benson, L. O. Bubulac, P. J. Smith, R. N. Jacobs, J. K. Markunas, M. Jaime-Vasquez, L. A. Almeida, A. Stoltz, J. M. Arias, G. Brill, Y. Chen, P. S. Wijewarnasuriya, S. Farrell, and U. Lee, J. Electron. Mater. **41**. 2971 (2012).

J. D. Benson, L. O. Bubulac, P. J. Smith, R. N. Jacobs, J. K. Markunas, M. Jaime-Vasquez, L. A. Almeida, A. Stoltz, P. S. Wijewarnasuriya, G. Brill, Y. Chen, U. Lee, M. F. Villa, J. Peterson, S. M. Johnson, D. D. Lofgren, D. Rhiger, E.A. Patten, and P. M. Goetz, J. Electron. Mater. **39**. 1080 (2010).

J. D. Benson, L. O. Bubulac, P. J. Smith, R. N. Jacobs, J. K. Markunas1 M. Jaime-Vasquez, L. A. Almeida, A. Stoltz, J. M. Arias, G. Brill, Y. Chen, P. S. Wijewarnasuriya, S. Farrell, and U. Lee, J. Electron. Mater. **41**. 2971 (2012).

J. D. Benson, P. J. Smith, R. N. Jacobs, J. K. Markunas, M. Jaime-Vasquez, L. A. Almeida, A. Stoltz, L. O. Bubulac, M. Groenert, P. S. Wijewarnasuriya, G. Brill, Y.Chen, and U. Lee, J. Electron. Mater. **38**. 1771 (2009).

J. D. Benson, S. Farrell, G. Brill, Y. Chen, P. S. Wijewarnasuriya, L. O. Bubulac, P. J. Smith, R. N. Jacobs, J. K. Markunas, M. Jaime-Vasquez, L. A. Almeida, A. Stoltz, U. Lee, M. F. Vileal, J. Peterson, S. M. Johnson, D. D. Lofgreen, D. Rhiger, E. A. Patten, and P. M. Goetz, J. Electron. Mater. **40**. 1847 (2011).

J. E. Ayers, Hetero-Epitaxy of Semiconductors: Theory, Growth, and Characterization, New York, NY: CRC Press, pp. 332–338, (2007).

J. Hutchison, and A. Kirkland, Nanocharacterization, RSC Publishing, (2007).

J. J. Kim, R. N. Jacobs, L. A. Almeida, M. Jaime-Vasquez, C. Nozaki, and David J. Smith, J. Electron. Mater. **42**. 3142 (2013).

J. J. Kim, R. N. Jacobs, L. A. Almeida, M. Jaime-Vasquez, C. Nozaki, and David J. Smith, J. Electron. Mater. **42**. 3142 (2013).

J. W. Garland, and S. Sivananthan, Springer Handbook of Crystal Growth, ed. By G. Dhanaraj, K. Byrappa, V. Prasad, and M. Dudley, Springer Heidelberg Dordrecht London New York, Chapter 32. p. 1076 (2010).

J. R. Arthur, Surf. Sci. **500**, 189-217 (2002).

K. Doyle and S. Trivedi. Dislocation Etching Solutions for Mercury Cadmium Selenide ARL-CR-0744 (2014).

K. Doyle, C. H. Swartz, J. H. Dinan, T. H. Myers, G. Brill, Y. Chen, B. L. Vanmil, P. Wijewarnasuriya, J. Vac. Sci. Technol., B. 31. 03C124 (2013).

K. Doyle, Development of $Hg_{1-x}Cd_xSe$ for 3rd Generation Focal Plane Arrays. West Virginia University, UMI Number: 3576281 (2013).

K. Jówikowski, and A. Rogalski, J. Electron. Mater. **29**, 736 (2000).

L. A. Giannuzzi, Introduction to Focused Ion Beam, Springer, New York (2005).

M. A. Kinch, Fundamentals of Infrared Detector Materials, SPIE press, (2007).

M. Nastasi, D. M. Parkin, and H. Gleiter, Mechanical properties and deformation behavior of materials having ultra-fine microstructures, Springer-Science+Business Media, B.V, (1992).

M. Reddy, D. D. Lofgreen, K. A. Jones, J. M. Peterson, W. A. Radford, J. D. Benson, and S. M. Johnson, J. Electron. Mater. **42**. 3114 (2013).

M. Reddy, W. A. Radford, D. D. Lofgreen, K. R. Olsson, and S. M. Johnson, J. Electron. Mater. **43**. 2991 (2014).

M. Vaghayenegar, R. N. Jacobs, J. D. Benson, A. J. Stoltz, L. A. Almeida, D. J. Smith, J. Electron. Mater. **46**. 5007 (2017).

M. A. Kinch, Fundamentals of Infrared Detector Materials. 67 (2007).

M. A. Kinch, J. Electron. Matter. **39**, 1043 (2010).

N. Yao, Focused Ion Beam Systems Basics and Applications, Cambridge University Press, Cambridge (2007).

P. Capper, and J. Garland, Mercury Cadmium Telluride Growth, Properties and Application. 159-161 (2011).

P. Capper, Narrow-gap II-VI Compounds for Optoelectronic and Electromagnetic Applications, Chapter 6. p. 204 (1999).

P. Norton, Opto-Electron. Rev. **10(3)**, 159-174 (2009).

P. Walker, W. H. Tarn, Handbook of Metal Etchants, CRC Press LLC, pp. 221 and 809 (1991).

P. Wijewarnasuriya, Y. Chen, G. Brill, N. Dhar, D. Benson, L. Bubulac, and D. Edwall, J. Electron. Mater. **39**. 1110 (2010).

R. Brydson, Aberration-Corrected Analytical Transmission Electron Microscopy, RMS-Wiley Imprint, (2011).

R. E. Smallman, and R. J. Bishop, Modern physical metallurgy and materials engineering science, process, and application 6th edition, Butterworth-Heinemann, (1999).

R. N. Jacobs, A. J. Stoltz, J. D. Benson, P. Smith, C. M. Lennon, L. A. Almeida, S. Farrell, P. S. Wijewarnasuriya, G. Brill, Y. Chen, M. Salmon, and J. Zu, J. Electron. Mater. **42**. 3148 (2013).

R. N. Jacobs, J. Markunas, J. Pellegrino, L. A. Almeida, M. Groenert, M. Jaime-Vasquez, N. Mahadik, C. Andrews, and S.B. Qadri, J. Cryst. Growth. **310**. 2960 (2008).

R. N. Jacobs, P. J. Smith, J. K. Markunas, J. D. Benson, and J. Pellegrino, J. Electron. Mater. **39**. 1036 (2010).

R. Tsu, Superlattice to Nanoelectronics 2nd edition, Elsevier, (2011).

R. N. Andrews, F.R. Szofran, and S.L. Lehoczky, J. Cryst. Growth. **92**. 445 (1988).

S. Farrell, G. Brill, Y. Chen, P. S. Wijewarnasuriya, M. V. Rao, N. Dhar, and K. Harris, J. Electron. Mater. **39**. 43 (2010).

S. Farrell, M. V. Rao, G. Brill, Y. Chen, P. Wijewarnasuriya, N. Dhar, D. Benson, and K. Harris, J. Electron. Mater. **40**. 1727 (2011).

S. Farrell, M. V. Rao, G. Brill, Y. Chen, P. Wijewarnasuriya, N. Dhar, J.D. Benson, and K. Harris, J. Electron. Mater. **42**. 3097 (2013).

S. Simingalam, J. Pattison, Y. Chen, P. Wijewarnasuriya, and M. V. Rao, J. Electron. Mater. **45**. 4668 (2016).

S. Y. Woo, G. A. Devenyi, S. Ghanad-Tavakoli, R. N. Kleiman, J. S. Preston, and G. A. Botton, Appl. Phys. Lett. **102**. 132103 (2013).

T. Yao, and Soon-Ku Hong, Oxide and Nitride Semiconductors Processing, Properties, and Application, Springer, (2009).

W. D. Lawson, S. Neilson, E. H. Putely, and A. S. Young, J. Phys. Chem. Solids. **9**, 325 (1959).

W. F. Zhao, R. N. Jacobs, M. Jaime-Vasques, L. O. Bubulac, and D. J. Smith, J. Electron. Mater. **40**. 1733 (2011).

W. J. Everson, C. K. Ard, J. L. Sepich, B. E. Dean, G. T. Neugebauer, and H. F. Schaake, J. Electron. Mater. **24**, 505 (1995).

W. Lei, J. Antoszewski, and L. Faraone, Appl. Phys. Rev. **2**, 041303 (2015).

W. Lei, R. J. Gu, J. Antoszewski, J. Dell, and L. Faraone, J. Electron. Mater. **43**. 2788 (2014).

W. F. Zhao, G. Brill, Y. Chen, and D. J. Smith, J. Electron. Mater. 41. 2852 (2012).

X. J. Wang, Y. Chang, C. R. Becker, C. H. Grein, S. Sivananthan, and R. Kodama, J. Electron. Mater. **40**. 1860 (2011).

Y. Chen, S. Simingalam, G. Brill, P. Wijewarnasuriya, N. Dhar, J.J. Kim, and D.J. Smith, J. Electron. Mater. **41**. 2917 (2012).

Y. A. R. Dasilva, R. Kozac, R. Erni, M. D. Rossel, Ultramicroscopy. **176**, 11 (2017).

Z. L. Wang, and Z. C. Kang, Functional and Smart Materials Structural Evolution and Structure Analysis, PLENUM PRESS. New York and London, (1998).